Aus dem
Helmholtz-Zentrum München
Comprehensive-Pneumology-Center (CPC)
Institute of Lung Health and Immunity (LHI)

Behavior and effect of nanoparticles in the pulmonary microcirculation

Dissertation

zum Erwerb des Doctor of Philosophy (PhD)
an der Medizinischen Fakultät der
Ludwig-Maximilians-Universität zu München

vorgelegt von:
Chenxi Li

aus:
Dongying, China

Jahr:
2024

Mit Genehmigung der Medizinischen Fakultät der

Ludwig-Maximilians-Universität zu München

Erstes Gutachten:	Prof. Dr. rer. nat. Markus Rehberg
Zweites Gutachten:	Prof. Dr. med. Markus Sperandio
Drittes Gutachten:	Prof. Dr. Fritz Frombach
Viertes Gutachten:	Prof. Dr. Susanna Zierler

Dekan:	Prof. Dr. med. Thomas Gudermann
Tag der mündlichen Prüfung:	23.01.2024

Table of content

Abstract

The lung, with its large surface area and thin air-blood barrier, presents an ideal site for drug delivery and serves as the main entry portal for inhaled particles. Additionally, the abundant pulmonary capillary bed provides an important surface for interactions with particles suspended in the bloodstream. Therefore, engineered nanoparticles (NPs) offer promising prospects for precision drug delivery to the lung. However, despite the potential benefits of NPs, their interactions and possible adverse effects in the pulmonary microcirculation under both healthy and pathophysiological conditions remain largely unknown. Understanding these interactions is crucial for harnessing the full potential of NPs in lung-specific drug delivery and ensuring their safety and efficacy for clinical applications.

To visualize and quantify the real-time dynamics of intravenously delivered or injected NPs and their interactions with the pulmonary vascular innate immune system, we utilized intra-vital microscopy of the alveolar region in mice. The NPs used in the study were divided into two distinct subsets: one usually considered of a low potential for interacting with biomolecules and cells (PEG-amine-QDs, referred to as aQDs), and the other with a high potential for such interactions (carboxyl-QDs, referred to as cQDs).

In vitro experiments demonstrated that cQDs were taken up more efficiently by Human Umbilical Vein Endothelial Cells compared to aQDs. In vivo experiments revealed that intravenously applied cQDs interacted with endothelial cells and might be taken up by them. In contrast, aQDs tended to form clusters in pulmonary vessels over time and induced stronger inflammation compared to cQDs, indicating that the PEG modification of QDs did not fully protect against their potential effects in the pulmonary microcirculation.

Under healthy conditions, i.v. injection of aQDs induced neutrophil recruitment, but did not significantly alter the immune responses under pathological conditions, such as LPS-induced acute inflammation and Bleomycin-induced fibrosis. The initiation of neutrophil recruitment induced by aQDs was found to require cellular degranulation and release of TNF-α. Furthermore, neutrophil response to aQDs appeared to involve the release of damage-associated molecular patterns (DAMPs), particularly extracellular ATP (eATP). This process also involved the

upregulation of relevant selectins (such as E-selectin) and the involvement of integrins (such as LFA-1 and MAC-1) on endothelial cells and neutrophils. These, in turn, resulted in a slowdown of the crawling velocity of neutrophils on the vascular surface. The blockage of selectins and integrins or the use of an eATP antagonist prevented recruitment of neutrophils and partially restored their reduced crawling velocity. Furthermore, the accumulation and retention of neutrophils in the pulmonary microcirculation led to a decrease in local blood flow velocity. Accordingly, when factors involved in neutrophil recruitment, such as cellular degranulation, DAMPs, and TNF-α release, as well as the upregulation of selectins and integrins, were diminished, blood perfusion could be restored to baseline levels.

Overall, this study unveils a detailed mechanism underlying the neutrophil response to aQDs, involving cellular degranulation, DAMPs and TNF-α release, as well as the upregulation of selectins and integrins. This intricate cascade ultimately leads to a reduced velocity of crawling neutrophils and a slowdown in blood perfusion. These insights pave the way for further exploration and optimization of NP-based drug delivery strategies, aiming to enhance efficacy and safety in medical applications.

1. Introduction

1.1 Nanoparticles exposure to the lung

With the increasing demand for nanotechnology, it is inevitable that nanomaterials and nanoproducts will encounter the human body (International Organization for Standardization, 2008). Nanomaterials consisting of solid particles are categorized as “nano” if the size of the respective materials ranges between 1 nm and 100 nm in at least one dimension (European Commission 2022). Exposure to nanomaterials and nanoparticles (NPs) through ingestion or inhalation, followed by internalization in cells has been strongly linked to a range of health issues, including neurological diseases, lung inflammation, cardiovascular diseases, auto-immune diseases, and cancer (Buzea, Pacheco, and Robbie 2007). Due to the large surface area and thin air-blood barrier, the lung is an ideal site for drug delivery and the main entry portal for inhaled particles. In addition, particles smaller than 10 μm (especially those smaller than 2.5 μm in diameter) that are inhaled can reach the peripheral region of the lungs (Mansour, Rhee, and Wu 2009; Yacobi et al. 2011; Nicolaou et al. 2021). A well-established method for evaluating the hazards of NPs in pathological lungs is through animal studies that involve inhalation, intratracheal instillation, and pharyngeal aspiration. These studies assessed a range of NPs, including carbon-based NPs, silica, manufactured NPs and so on. They focused on the immune system, primarily the neutrophils and macrophages in the alveolar and interstitial space, and on potential genetic aberrations (Morimoto et al. 2013, Murugadoss et al. 2017, Donaldson and Poland 2012). The clearance of NPs that have been deposited in the lower airways is associated with size-dependent phagocytosis of these NPs by alveolar macrophages. Alveolar macrophages perform surveillance in the air spaces of the deep lung and are capable of effectively removing inhaled particles in the size range of 1-5 μm (Murgia, Carvalho, and Lehr 2014). When it comes to NPs smaller than 100 nm, they are often able to evade the surveillance of alveolar macrophages, which enables them to penetrate the air-blood barrier of the lungs more easily and translocate into the bloodstream, lymphatic systems, and secondary organs (Oberdörster 2001; Geiser et al. 2005; Buzea, Pacheco, and Robbie 2007; Kreyling 2010; Baranov et al. 2021) (Fig.1). NPs in the blood stream

are cleared by the hepatic and renal pathways. In the hepatic pathway, NPs are taken up and extensively broken down by the mononuclear phagocyte system (MPS) and tissue phagocytes followed by biliary elimination and excretion via the stools (Yang et al. 2019). In the renal pathway, NPs, which are smaller than the kidney filtration threshold of ~6nm, can undergo the primarily renal clearance and thereby avoid to be captured by the MPS (Zhu, Gray, and Patra 2022).

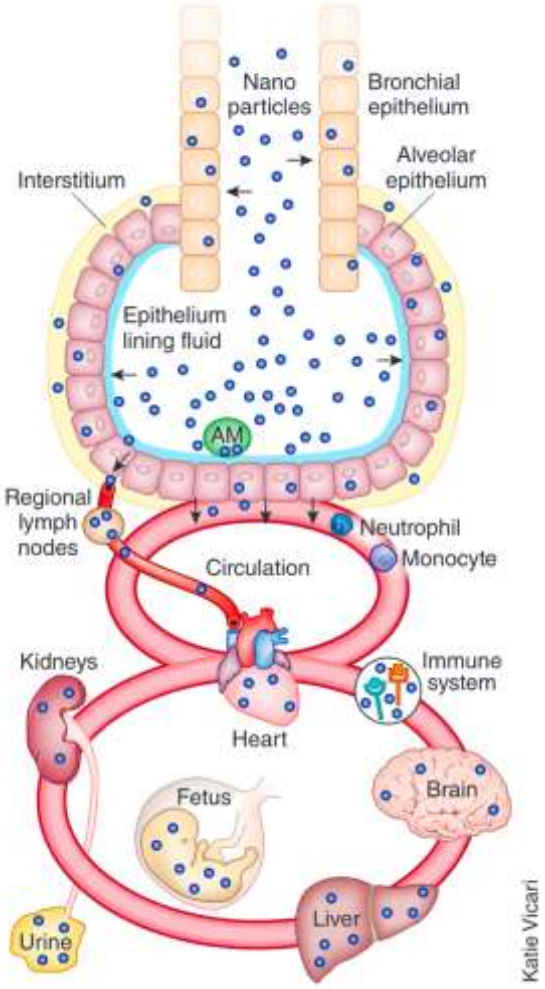

Figure 1. Deposited NPs cross the bio-barrier and translocate into circulatory and lymphatic system, and are thereby distributed to secondary organs (Kreyling 2010).

1.2 Fluorescent NPs/Quantum dots for biomedical application

The increased demand for nanotechnology in medicine and research has led to the development of various types of fluorescent nanoparticles such as carbon

dots, quantum dots (QDs), nanodiamonds, etc., whose safety, biocompatibility, and toxicity in imaging and biological application have been of concern in recent decades. Among these, QDs are the earliest and most common used fluorescent inorganic probes and semiconductors with a size of less than 10 nm (Li et al. 2022). QDs have a distinctive metal core-shell nanostructure that confers them with exceptional fluorescent properties, including high fluorophore brightness, photostability, a broad excitation spectrum, a high emission intensity, and narrow emission spectra. These properties make them suitable for various imaging techniques and drug delivery towards theragnostic approaches (Wegner and Hildebrandt 2015). Praetner et al. conducted a study to investigate the potential role of surface modification of fluorescent QDs (carboxyl-, amine-, and polyethylene glycol (PEG) -QDs) in targeting specific organs and found that carboxyl-QDs (cQDs) had a short residence time in the blood and accumulated in various organs, particularly those with high capillary network density, such as the liver and spleen (Praetner et al. 2010). Studies had shown that laser treatment using Bortezomib-QDs synthesized NPs had a photothermal effect that reduced tumor growth, necrosis, and deformation of cancer cells compared to the control treatment in a tumor-bearing nude mice model. This suggests that Bortezomib-QDs could be a promising cancer therapeutic agent with good biocompatibility (Guo et al. 2021). Fromen and colleagues utilized carboxylate-modified micron sized particles as a therapeutic intervention in models of inflamed mesenteric vasculature. The interaction between particles and neutrophils inhibited the recruitment of neutrophils and facilitated the clearance process of particles in the bloodstream due to a particle-induced neutrophil diversion to the liver (Fromen et al. 2017).

Due to the heavy metal content of QDs, such as cadmium, application of QDs as biological platforms or imaging agents has been associated with toxic effects in cell and animal experiments (Li et al. 2022). It has been demonstrated that different surface modifications of QDs can have different influence on cells in vivo and in vitro, and can alter their interaction within the microvasculature, their bio-distribution, and proinflammatory effects (Praetner et al. 2010; Rehberg et al. 2012). For instance, amine/PEG-QDs (aQDs) have weak protein binding, while cQDs have strong protein binding (Fig.2). cQDs have been shown to induce leukocyte recruitment in postcapillary venules in skeletal muscle tissue. Upon application into the bloodstream, they are taken up by perivascular macrophages, which

might serve as the initial step for leukocyte recruitment. This uptake is followed by cellular degranulation, and the adhesion step of leukocytes is mediated by the expression of ICAM-1. Consequently, leukocytes transmigrate outside of the postcapillary venules (Rehberg et al. 2010).

A

Physical characterization of QDs.

Particle	Diameter (nm)	PdI	Zeta potential (mV)
Carboxyl-QDs			
H_2O	22.2 ± 0.8	0.113 ± 0.111	−42.5 ± 0.6
NaCl	21.2 ± 0.9	0.123 ± 0.103	−28.8 ± 5.2
PBS	18.1 ± 0.2	0.025 ± 0.029	−22.5 ± 4.3
PBS + serum	41.9 ± 0.3	0.448 ± 0.039	−14.8 ± 0.3
Amine-QDs			
H_2O	22.7 ± 0.3	0.037 ± 0.026	−29.2 ± 4.2
NaCl	25.8 ± 0.2	0.016 ± 0.013	−8.5 ± 5.0
PBS	25.2 ± 0.6	0.054 ± 0.030	−5.2 ± 1.8
PBS + serum	36.5 ± 0.4	0.405 ± 0.007	−5.9 ± 0.2
PEG-QDs			
H_2O	37.5 ± 1.0	0.053 ± 0.025	−32.2 ± 5.4
NaCl	34.4 ± 0.4	0.094 ± 0.010	−7.2 ± 2.1
PBS	36.1 ± 0.7	0.078 ± 0.042	−1.1 ± 1.4
PBS + serum	46.6 ± 0.8	0.578 ± 0.008	−7.2 ± 0.8

B

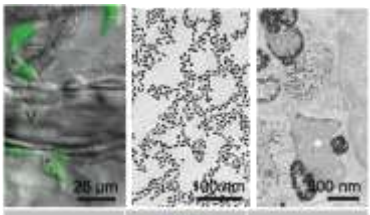

C

Surface coating	Surface charge PBS (mV)	Protein binding
carboxyl-QDs	-22.5 ± 4.3	strong
amine/PEG-QDs	-5.2 ± 1.8	weak
PEG-QDs	-1.1 ± 1.4	weak

Figure 2. (A) Physical characterization of various QDs also used in this thesis (Praetner et al. 2010). (B) Left: cQDs exhibited fluorescence (green) in perivascular cells and venules after intravenous injection; middle: TEM image of cQDs; right: TEM section of mouse cremaster muscle exposed to cQDs in the electron microscope (Zeuschner 2015). (C) Protein binding scheme of different QDs (Rehberg et al. 2010).

1.3 Lung intravital microscopy

Intravital microscopy (IVM) has undergone extensive development since the first attempt to observe rolling leukocytes in 19th century and has become a more practical technique for studying physiological and pathophysiological states of different organs. To elucidate the real-time dynamic process and imaging at cellular levels in various organs (including but not limited to the liver, kidney, brain, skeletal muscle, and skin) in living animals, IVM is equipped with various optical modalities to facilitate different imaging needs (Secklehner, Lo Celso, and Carlin 2017). IVM plays a crucial role in studying innate immune responses during pathological conditions. It enables the investigation of various processes, such as leukocyte recruitment cascade and the scavenger and phagocytic functions, for example, of Kupffer cells. It is also utilized to investigate in vivo delivery of

NPs, including their interactions with immune cells in different organs (Lin, Fathi, and Chen 2020; Neupane and Kubes 2022).

The lung is a vital organ responsible for respiration, and the pulmonary blood system represents the largest microcirculation in the body. Establishing an IVM platform to study the lung is particularly challenging due to the continuous respiratory motion and heart beating, making it one of the most difficult organs to image. Mark R. Looney developed a modified version of stabilized lung imaging that utilizes an imaging window, which is inserted in the chest, with additional reversible vacuum to gently absorb the lung surface to the thoracic window. This technique, called Lung Intravital Microscopy (L-IVM), allows for the study of the immediate dynamic interaction between tumor microparticles, lung tissue, and the immune system (Looney et al. 2011; Headley et al. 2016). In this approach, the continuous application of negative pressure suction carries the potential risk of inducing local inflammation. However, short-term imaging (less than 2h) did not result in significant neutrophil accumulation (Looney et al. 2011). Park et al. utilized L-IVM to visualize the pulmonary endothelial surface layer in both physiological and pathophysiological conditions (Park et al. 2018). Detampel et al. applied this approach to investigate the clearance mechanism of amorphous silica NPs following instillation in the lung and demonstrated that it was dependent on transcytosis process mediated by alveolar epithelial cells (Detampel et al. 2019). Our laboratory is at the forefront of utilizing this technique for studying NPs and their interactions with immune cells in the pulmonary microcirculation.

1.4 Innate immunity in the lung microcirculatory system

The primary functions of lung capillaries are to facilitate essential gas exchange and the lung microvessels serve as a functional immune niche (Granton et al. 2018) (Fig.3). The blood perfusion velocity in the pulmonary capilaries is relatively low (Rossaint and Zarbock 2013). Assuming inertia, a flow rate of 6.40^{-10} m^3/s at the arteriole inlet translates to a total blood flow of 2.42–2.46 l/min through the human lung, which is slightly lower than the reported cardiac outputs of 5 L/min. Haber et al. also demonstrated that in their study, blood flow exhibited a continuous decrease from $1.8x10^{-14}$ m^3/s to $0.5x10^{-14}$ m^3/s across generations 1 to 9 (Haber, Clark, and Tawhai 2013). In contrast to other organs, the lung does not

have resident vascular macrophages in the pulmonary microcirculation, and in the steady state, substantial neutrophils patrol the pulmonary capillaries, which is known as the marginated pool (Granton et al. 2018). Neutrophils are the front-line cells responsible for defending the host against invading pathogens, and they also play an essential role in physiological process (Kolaczkowska and Kubes 2013; Liew and Kubes 2019). Neutrophils have multiple key functions, including inducing the generation of reactive oxygen species (ROS), the release of pro-inflammatory mediators, and the release of neutrophil extracellular traps (NETs). Additionally, neutrophils also play a crucial role in phagocytosis, i.e., the process of engulfing and removing cell debris or pathogens (Gazendam et al. 2016; Segal, 2005). Yipp et al. investigated the immune responses to *Escherichia coli* bloodstream infection in mice by observing the pulmonary microcirculation using L-IVM. Their study demonstrated that neutrophils, not monocytes, played an essential role in sequestering bacteria from the bloodstream. This involved patrolling neutrophils of the marginated pool, allowing them to immediately react and capture pathogens after the pulmonary endothelium immobilized the flowing E.coli pathogens in capillaries through toll-like receptor 4 (TLR-4), Myd88, and CD11b dependent signaling (Yipp et al. 2017). This process is on par with the host vascular defense of the macrophage-dominated liver and spleen (Kolaczkowska and Kubes 2013; Liew and Kubes 2019).

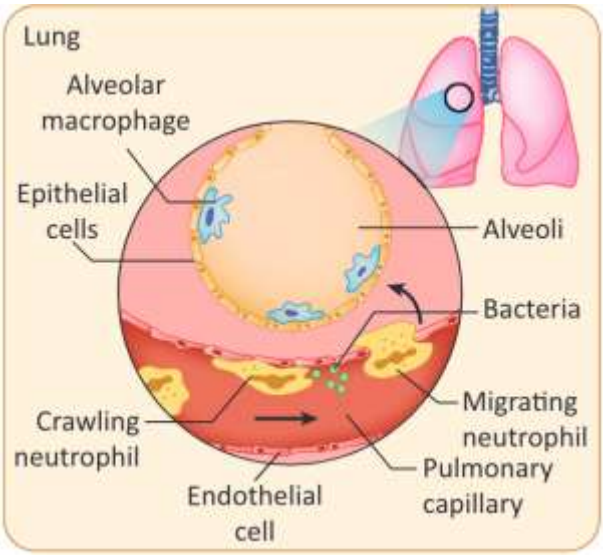

Figure 3. Innate cellular host defense steps of the lung (Granton et al. 2018).

In general, leukocyte recruitment involves several steps in most organs. First, endothelial cells are stimulated by inflammatory mediators (including histamine, cytokines, and pattern recognition receptor (PRR)-mediated detection of pathogens) causing neutrophils to slowly roll on the top of them. This is followed by the strengthening of adhesion and crawling, and finally paracellular and transcellular migration across the blood-vessel walls into the interstitial tissue (Ley et al. 2007; Kolaczkowska and Kubes 2013).

The activation of selectin and integrin ligands is a critical part of this process. E-selectin and P-selectin are typically upregulated on the surface of endothelial cells, while these two selectins work synergistically to optimize neutrophil recruitment with partially overlapping in their functions. In addition to mediating neutrophil-endothelial cell interactions, P-selectin is also expressed on activated platelet and the platelet-neutrophil aggregates also prompt neutrophils recruiting to the endothelium (Begandt et al. 2017; Maas, Soehnlein, and Viola 2018). In this process, L-selectin is expressed on circulating neutrophils to facilitate neutrophil recruitment. The glycoprotein ligands (for example, P-selectin glycoprotein ligand 1, PSGL1) for these selectins are expressed on both leukocytes and endothelial cells. Selectins initially serve to capture neutrophils from the bloodstream and facilitate their tethering and rolling along the endothelium in classical cascade (Kolaczkowska and Kubes 2013). Integrins, including lymphocyte function–associated antigen-1 (LFA-1) and macrophage-1 antigen (Mac-1), are also involved in leukocyte rolling, as well as mediating arrest, firm adhesion, and crawling (Ley et al. 2007). Henderson et al firstly emphasize the role of LFA-1 in the stabilization of the transient or tethering phase of neutrophil rolling, thereby contributing to the process of neutrophil rolling on the mesenteric vascular bed detected by IVM. On the other hand, the presence of MAC-1 is not essential for either rolling or firm adhesion, but rather exhibits distinctive properties in facilitating emigration from the vessel (Henderson et al. 2001).

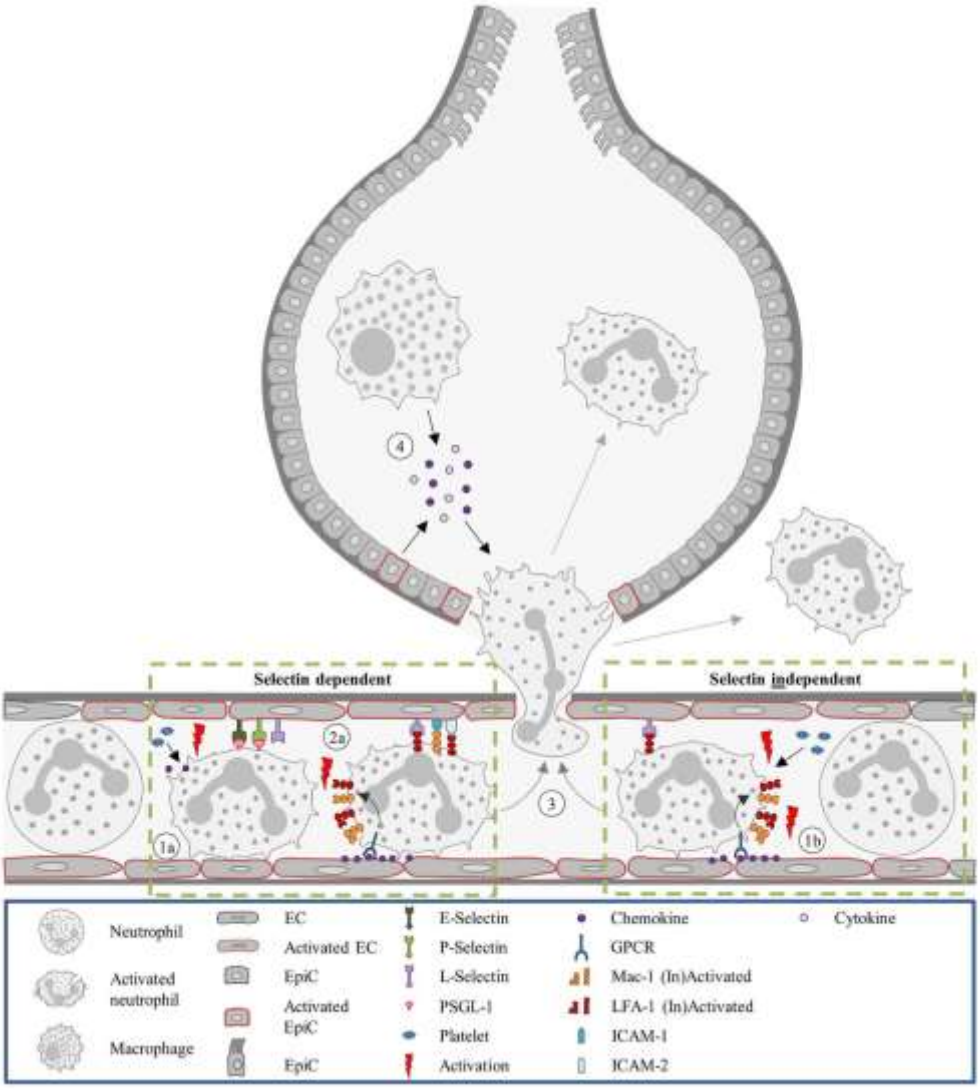

Figure 4. Scheme of neutrophil recruitment in the lung (Maas, Soehnlein, and Viola 2018).

The mechanism of neutrophil recruitment is well-defined and varies depending on the specific organs, different stimuli, and tissue states. However, unlike other organs, neutrophil recruitment in the pulmonary microcirculation differs (Maas, Soehnlein, and Viola 2018) (Fig.4). Endothelial cells, in conjunction with alveolar macrophage and epithelial cells, secrete chemokines, cytokines, and other inflammatory mediators that foster local inflammation and neutrophil accumulation. Due to the diameter of lung capillaries, ranging from 2 to 14 μm, which is smaller than that of neutrophils at approximately 13.7 μm, neutrophils are typically deformed, and the previous view was that they were sequestered in the lung capillaries by means of mechanical trapping, without undergoing the rolling step, as observed in post-capillary venules (Doerschuk et al. 1993; Maas, Soehnlein, and

Viola 2018). Recent advancements in this field have challenged the previous understanding that neutrophil accumulation in the pulmonary microcirculation solely results from mechanical trapping, it is now recognized that neutrophil accumulation generally does not cause complete occlusion of pulmonary vascular blood flow. Neutrophils in the microcirculation engage in tethering and crawling processes, enabling them to interact with endothelial cells and survey potential pathogens. This dynamic behavior of marginated neutrophils contributes to an effective immune response and facilitates the clearance of potential pathogens (Neupane and Kubes 2022). The necessity of selectins and integrins for neutrophil recruitment in the lung varies depending on various stimuli (Rossaint and Zarbock 2013; Maas, Soehnlein, and Viola 2018). For instance, the intratracheal administration of LPS from *Streptococcal pneumonia* induces neutrophil recruitment without dependency on E- or P-selectin, whereas LPS from *Escherichia coli* causes E- and L-selectin-dependent neutrophil recruitment (Mizgerd et al. 1996; Kornerup et al. 2010). Neutrophil recruitment in acute lung inflammation occurs through selectin-dependent or independent pathways, depending on the specific stimuli involved, such as *E. coli*, IL-1, *S. pneumonia*, and C5a (Hellewell et al. 1991; Mizgerd et al. 1997; Ganter et al. 2008; Xu et al. 2008).

1.5 Pulmonary diseases

1.5.1 Acute lung Injury

Rodent's acute lung injury (ALI) can be induced by depositing immunoglobulin (Ig) G immune complexes intrapulmonary, in turn triggering an inflammatory reaction. IgG complexes and C5a, which is a product of complement activation, activate the lung macrophages and lead to the release of cytokines, for example interleukin (IL) -1 and -6, TNF-α, as well as chemokines such as CXC, KC, and CC chemokines (Guo and Ward 2002). In LPS-induced ALI, the mechanism is not primarily associated with C5a (Rittirsch et al. 2008), but rather with the TLR-4 and MyD88 signaling cascade. This signaling cascade triggers various intracellular pathways, such as P38, to regulate the production of pro-inflammatory cytokines like IL-1β, IL-6, and TNF-α, by activating the NFkB pathway (Domscheit et

al. 2020; Ali et al. 2020). The feature of ALI involves the influx of polymorphonuclear neutrophils, interstitial and alveolar edema, as well as intra-alveolar hemorrhage. IL-1 and TNF-α induce the expression of adhesion molecules, including E-selectin and ICAM-1, on the pulmonary vascular endothelium, thereby increasing neutrophil adhesion and facilitating neutrophil transmigration into the lung interstitial tissue and distal airways (Ward 2003). Chemokine-receptor interactions exhibit functional redundancy, with multiple chemokines binding to the same receptor and a single chemokine binding to multiple receptors (Wissinger et al. 2008). The generation of CXC chemokines in the lungs results in neutrophil recruitment to the interstitial and alveolar space. Meanwhile, CC chemokines serve as autocrine factors that effectively augment the function of macrophages, thereby enhancing the production of CXC chemokines (Ward 2003). Using L-IVM in conjunction with two-photon confocal microscopy, Ueki et al. established a fluorescent influenza viruses infected mice model and observed that the inflammation induced by viral infections influenced alterations in neutrophil motility and reduced the blood perfusion speed in pulmonary capillaries (Ueki et al. 2018). Park et al. investigated the alteration of the functional capillary ratio, as a parameter used to assess the fraction of functional microvasculature in the pulmonary microcirculation and dead space, in acute lung injury induced by sepsis and found it decreased in the early stage. Their findings suggest that prolonged neutrophil entrapment within the capillaries can develop the generation of dead space (Park et al. 2019).

1.5.2 Chronic pulmonary fibrosis

Idiopathic pulmonary fibrosis (IPF) is a chronic and progressive lung disease marked by an excessive deposition of extracellular matrix proteins within the interstitial lung and a progressive decline in lung function (Martinez et al. 2017). Bleomycin, an antibiotic drug that damages DNA of cancer cells as a chemotherapy, is the most widely used agent to induce pulmonary fibrosis in mice (Hay, Shahzeidi, and Laurent 1991). In the early stages of injury induced by Bleomycin, the damage is mainly localized to bronchioles, where there is an increase in inflammatory cells and early hyperplastic changes in type II pneumocytes, accompanied by microvascular leakage. On day 7 following Bleomycin treatment, the

damage becomes more diffuse and affects the distal lung parenchyma, with multiple inflammatory foci and edema observed within the alveolar septum. By day 14, the lungs display a well-established interstitial fibrosis in a regional distribution, accompanied by alveolar septal thickening, elevated macrophage numbers, and focal lymphocytosis with lymphoid expansion (Tashiro et al. 2017; Miles et al. 2020). Although neutrophils are well-known as effector cells in defense against acute inflammation, they also contribute to chronic pulmonary fibrosis. Studies have found a positive correlation between the ratio of neutrophils to total cells in lung tissue and the degree of lung fibrosis (Pardo et al. 2000). NETs secreted by neutrophils induce differentiation of lung fibroblasts into myofibroblast phenotype by expressing IL-17, which is a major initiator of inflammation/fibrosis. This promotes the fibrotic activity of differentiated lung fibroblasts (Chrysanthopoulou et al. 2014). Besides, activated platelets have the ability to release pro-fibrotic mediators, which may play a role in the development of lung fibrosis (Crooks et al. 2014). Zhou et al. elucidated that fibroblast proliferation and trans-differentiation into myofibroblasts in the process of Bleomycin-induced pulmonary fibrosis are closely associated with thrombopoietin activated megakaryocytes through releasing transforming growth factor-β mostly (Zhou et al. 2019).

1.5.3 Exposure of the pathologically altered lung to NPs

Exposure to NPs has been reported to induce various patterns of lung inflammation such as multifocal granulomas, pulmonary fibrosis, and pulmonary emphysema (Warheit et al. 2004; 2007; Chen, Su, et al. 2006). In addition, NP exposure aggravates pre-existing pulmonary pathological conditions. Inoue et al demonstrated that the intratracheal administration of smaller NPs exacerbated lung inflammation and pulmonary edema induced by LPS, accompanied by increased expression of IL-1β and CC chemokines in the lungs (Inoue et al. 2006). Studies have demonstrated that mice exposed to ovalbumin along with NPs exhibit a significant increase in goblet-cell hyperplasia and an influx of eosinophils, neutrophils, and mononuclear cells. Moreover, exposure to NPs may modify the lung inflammatory response, lung hyperresponsiveness, and airway remodeling induced by ovalbumin alone (Last et al. 2004; Inoue et al. 2005; 2007). This process is characterized by the promotion of Th immunity, enhanced oxidative

stress, and inappropriate activation of antigen-presenting cells such as dendritic cells (Inoue et al. 2009; 2010).

1.6 Advantages and disadvantages of nanomedicines targeting the lung and the pulmonary microcirculation

Nanotechnology has significant potential for medical applications due to the similarity in scale between nanomaterials and biological molecules/systems, as well as the ability to engineer nanomaterials with specific functions. Unique properties and physical characteristics of nanomaterials are utilized as nanomedicine for the treatment, diagnosis, monitoring, and control of biological systems. A handful of NPs, such as metallic-, semiconductor-, and organic-nanomaterials, have received attention towards drug carrier and diagnostic imaging in nanomedicine (Kim, Rutka, and Chan 2010).

Pulmonary drug delivery is an emerging field of technology that encompasses two main approaches: i) administering medication through inhalation into the lungs, enabling its absorption into the bloodstream via the alveolar epithelium (Liang et al. 2020), and ii) delivering drugs via intravenous (i.v.) injection into the pulmonary microcirculation (Fu et al. 2002). The lung has been identified as a promising “super target” for the delivery of nanomedicines for several reasons. Firstly, the lung has a vast surface area and high vascularization, which make it an ideal site for drug delivery. Moreover, there are less drug metabolizing enzymes in the lungs compared to other organs, which reduces the effects of first-pass metabolism. Additionally, non-invasive means of drug delivery to the lungs allow for localized effects and a more rapid onset of therapeutic action in lung diseases such as COPD, asthma, and lung cancer. After being delivered into the lung, NPs can passively distribute due to the pathological environment or actively cross the thin air-blood barriers and enter the systemic circulation (Smola, Vandamme, and Sokolowski 2008; Mansour, Rhee, and Wu 2009; Murgia, Carvalho, and Lehr 2014; Qiao et al. 2021). Inhaled as well as injected (i.v.) NPs can be modified in terms of their size, shape, surface charge, hydrophilicity, and surface modifications. These modifications enable active, passive, or physico-chemical targeting to specific sites such as the pulmonary endothelium, neutro-

phils, or areas of inflammation in conditions like acute respiratory distress syndrome (ARDS), pulmonary arterial hypertension, and lung cancer. By utilizing these strategies, NPs can be designed to effectively deliver therapeutic agents to the desired target within the lungs (Deng et al. 2021; Qiao et al. 2021).

Despite the potential benefits of nanomedicines targeting the lungs, there are also some risks of unintended side effects. For example, NPs after inhalation can induce the formation of neutrophil plugs (Oberdörster 2001; Buzea, Pacheco, and Robbie 2007) and potentially reduce blood flow, which could result in impaired gas exchange and respiratory distress (Hellewell et al. 1991; Park et al. 2019). Inhaled NPs may trigger an inflammatory response, causing damage to lung tissue (André et al. 2006; Ganguly et al. 2017) and potentially exacerbating pre-existing lung conditions (Inoue et al. 2005; 2006; Alessandrini et al. 2006; Geiser et al. 2014; Sattler et al. 2017). In addition, exposure to NPs induces thrombogenic effects in the microcirculation of healthy mice, irrespective of the route of administration (i.e., inhalation or infusion). These thrombogenic effects caused by NPs are not linked to a local or systemic inflammatory response and appear to be independent of pulmonary inflammation (Khandoga et al. 2010). The regulatory approval process for nanomedicine particles is complex and time-consuming, which may limit their availability and clinical use (Resnik and Tinkle 2007).

In summary, nanomedical particles targeting the lung/pulmonary microcirculation offer promising benefits for drug delivery and treatment efficiency. However, the interactions between NPs and the pulmonary microcirculation are not yet fully understood, which may limit their effectiveness and safety. Therefore, careful evaluation of the potential risks and benefits of nanomedicine delivery to the pulmonary microcirculation should be carried out. Hence, we utilize QDs as model NPs to investigate their behavior and impact on the pulmonary microcirculation under both physiological and pathophysiological conditions.

2. Material and Methods

2.1 Materials

2.1.1 Equipment and instruments

Table 2.1: List of laboratory instruments

Instruments	Type	Company
Automatic benchtop tissue processor	Leica TP1020	Leica Mikrosysteme Vertrieb GmbH Mikroskopie und Histologie, Wetzlar, Deutschland
Cell culture bench	Thermo Scientific™ Herasafe™ KS	Fisher Scientific GmbH Schwerte, Germany
Centrifuge	3K15	Sigma Laborzentrifugen Osterode am Harz, Germany
Centrifuge	MICRO centrifuge Model SD 220VAC	Carl Roth GmbH + Co. KG Karlsruhe, Germany
Centrifuge Cytospin™	Cytospin 2	Thermo Shandon Ltd, UK
CO_2 incubator	CB 150 #01-28940	Binder GmbH Tuttlingen, Germany
FACS cytometer	BD FACSCanto II flow cytometer	BD Biosciences, State of New Jersey, United States
Freezer	Liebherr Mediline	Liebherr GmbH Ochsenhausen, Germany
Fridge	Liebherr Comfort	Liebherr GmbH Ochsehausen, Germany
Fridge	Liebherr Profiline	Liebherr GmbH Ochsenhausen, Germany
Fridge	Siemens KU18R04	SEG Hausgeräte GmbH München, Germany
Hematology analyzer	IDEXX ProCyte	IDEXX Laboratories, USA
Histostar	Thermo Fisher Scientific	Thermo Fisher Scientific, Carlsbad, USA
Hyrax C50	Cryostat	Zeiss, Jena, Germany

Laboratory pH sensor	SevenEasy pH	Mettler-Toledo GmbH, Switzerland
Mouse heating pad	Standard, 12.0 x 20.5 cm	Harvard Apparatus, Massachusetts, USA
Plate reader	TECAN Infinite® M200 PRO	TECAN Group Ltd. Männdorf, Switzerland
Plate reader	TECAN Safire 2	TECAN Group Ltd. Männdorf, Switzerland
Plate reader	Luminex™ 200, LX10009257402	Invitrogen™, Thermo Fisher Scientific, Carlsbad, USA
Rotary microtome	Hyrax M55	Zeiss, Jena, Germany
Vortexer	VF2	IKA® - Labortechnik Staufen, Deutschland
Waterbath	LAUDA AQUAline AL 12	LAUDA DR. R. WOBSER Lauda-Königshofen, Gemany
Zetasizer Nano ZS	MAL1016038	Malvern Panalytical, UK

Table 2.2: List of microsurgical instruments

Instruments	Type	Company
Custom-made vacuum window	Kindly provided by Leon Carlin, Beatson Institute, Cancer Research UK	
Extra fine graefe forceps	No.11151-10	F•S•T, Hans Gawenda, Canada
Extra fine bonn scissors	No.14084-08	F•S•T, Hans Gawenda, Canada
Jeweler forceps	Dumont No.5	Dumont, Switzerland
Shaver	Aesculap Favorita II GT104	Aesculap AG, USA
Vannas Spring Scissors	Straight 3mm Cutting Edge	F•S•T, Hans Gawenda, Canada

Table 2.3: List of microscope equipment

Equipments	Type	Company
Beam splitter	T 580 lpxxr	Chroma Technology, Bellows Falls, VT, United States
Camera	AxioCam MRm	Carl Zeiss, Oberkochen, Germany
Camera	sCMOS	Andor Neo, Abingdon, Oxfordshire
Camera	CCD camera	Megaview, Olympus-SIS, Muenster, Germany
EMCCD cameras	Rolera EM-C2 cameras	Q-imaging, Surrey, Canada
Fluorescence excitation source	CoolLED pE-4000	CoolLED Ltd, Andover, Great Britain
Heating system	Universal fit for every inverted microscope	ibidi GmbH, Gräfelfing, Germany
Imaging software	VisiScope A1 imaging system	Visitron Systems, Puchheim, Germany
In vivo imaging system	Lumina II	Caliper/Perkin Elmer, Hopkinton, Massachusetts, United States
Gas incubation system for CO_2 and O_2	Ibidi Gas Mixer	ibidi GmbH, Gräfelfing, Germany
LED light source	pE-100	CooLED, Andover, United Kingdom
LSFM	Ultramicroscope II	LaVision BioTec GmbH, Bielefeld, Germany
Manometer Magnehelic	Serie 2000/2300	Dwyer, Electro-Mation GmbH, Deutschland
Microscope	TCS SP5 SMD	Leica, Wetzlar, Germany
Microscope	Observer.Z1 Inverted Phase Contrast Fluorescence Microscope	Carl Zeiss, Oberkochen, Germany
Microscope	Axiovert 135	Carl Zeiss, Oberkochen, Germany

Microscope	Laser Scanning Confocal Microscope (LSM710)	Carl Zeiss, Oberkochen, Germany
Objective lens	MVPLAPO 2×/0.5 NA	Olympus, Tokyo, Japan
Water dipping objective lens	20×, NA 1.0	Carl Zeiss, Oberkochen, Germany
Water immersion objective	63×, NA 1.0	Carl Zeiss, Oberkochen, Germany
Zoom body	MVX-10	Olympus, Tokyo, Japan

Table 2.4: List of consumables

Subject	Type	Company
Cell counting chamber	BLAUBRAND® Neubauer Improved, bright line	Brand GmbH + Co. KG, Werthein, Germany
Cell culture dish	TC Dish 100 mm, standard	SARSTEDT AG & Co. Nümbrecht, Germany
Cell culture flask	cellstar® T25, T75	Greiner Bio-One GmbH Frickenhausen, Germany
Cellulos swabs	Askina® Brauncel	B.Braun Melsungen AG, Melsungen, Germany
Combitips	Advanced®, 5ml	Eppendorf AG Hamburg, Germany
Cryo tubes	CryoPure Tubes	SARSTEDT AG & Co. Nümbrecht, Germany
EDTA-coated disposable plastic capillary pipettes	50 µl	Kabe Labortechnik GmbH, Germany
Eye ointment	5 g, mit 5 % Dexpanthenol	Bepanthen, Bayer Vital GmbH, Deutschland
Falcon tube	15 ml, 50 ml	Corning Incorporated New York, USA
Glass coverslips	25 x 25 mm/8 mm diiameter	VWR, Radnor, USA
Insulin syringes	MicroFine $^{TM+}$	BD Biosciences, State of New Jersey, United States

Indwelling cannula	Introcan® 20 G	B.Braun Melsungen AG Melsungen, Germany
Injection cannula	Sterican® Gr. 18, G 26	B.Braun Melsungen AG Melsungen, Germany
Lab gloves	Nitril® NextGen®	Meditrade GmbH Kiefersfelden, Germany
Microslide	VWR Superfrost Micro Slide	VWR, Radnor, USA
Microcapillary pipette	5 µl, 50 µl Minicaps	Hirschmann Laborgeräte GmbH & Co. KG, Germany
Multi-channel pipet	Research plus® 300 µl	Eppendorf AG Hamburg, Germany
Parafilm	PARAFILM® M	Bemis Company, Inc. Neenah, USA
Pasteur pipette	Disposable Glass Pasteur Pipettes 230 mm	Poulten & Graf GmbH Wertheim, Germany
Pipettes	10 µl, 20 µl, 100 µl, 200 µl, 1000 µl	STARLAB International GmbH Hamburg, Germany
Pipette tips	10 µl, 20 µl, 200 µl, 1000 µl	Starlab International GmbH Hamburg, Germany
Pipetting aid	pipetus®-akku	Hirschmann Laborgeräte Eberstadt, Germany
Precision wipes	Kimtech Science	Kimberly-Clark GmbH Koblenz, Germany
Reaction tubes	0.5 ml, 1.5 ml, 2.0 ml	Eppendorf, Hamburg, Germany
Serological pipettes	5 ml, 10 ml, 25 ml, 50 ml	Greiner Bio-One GmbH Frickenhausen, Germany
Syringe	1ml, 2 ml, 5ml, 10ml and 50 ml	B.Braun Melsungen AG Melsungen, Germany
Steril filtration filters	Filtropur S, 0.45 µm, 100 µm	SARSTEDT AG & Co. Nümbrecht, Germany
µ-Slide 8-well	ibiTreat	ibidi GmbH, Gräfelfing, Germany

6-, 12-, 24-, 96-well Cell culture Plate	Greiner CELLSTAR® Cell culture plate	Greiner Bio-One GmbH, Frickenhausen, Germany

Table 2.5: List of chemicals

Chemicals	Type	Company
Bucain	2.5 mg/ml	Puren Pharma GmbH & Co. KG, Germany
Cromolyn sodium salt	assay ≥ 95%	SigmaAldrich, Taufkirchen, Germany
A438079 hydrochloride (Competitive $P2X_7$ antagonist)	≥ 98 % (HPLC)	Bio-Techne GmbH, Germany
Bleomycinsulfat aus Streptomyces verticillus	B5507-15UN	SigmaAldrich, Taufkirchen, Germany
Dichloromethane (DCM)	assay ≥ 99.8 %	Sigma Aldrich, Taufkirchen, Germany
Dibenzyl ether (DBE)	assay ≥ 98.0 %	Sigma Aldrich, Taufkirchen, Germany
DPBS (1X) Dulbecco's Phosphate Buffered Saline	500 ml	Gibco™ life technologies Thermo Fisher Scientific Carlsbad, USA
eBioscience™ 1x RBC Lysepuffer	200ml	Invitrogen, Themo Fisher Scientific, USA
Eosin solution	1 l	Carl Roth GmbH & Co. KG, Germany
Entellan® mounting medium	100 ml	Merck Millipore, Germany
Ethanol absolute	32205-1l	Sigma Aldrich, Taufkirchen, Germany
Fluorescence mounting medium	15 ml	Dako Omnis, Agilent, Santa Clara, USA
Fentanylcitrat	Fentanyl-Piramal® 0.05 mg/ml	Piramal Critical Care GmbH, Hallbergmoos, Germany

Giemsa Stain	1 l	Merck SA, Darmstadt, Germany
Hydrochloric acid	acide chlorhydriique 32 %	Merck Millipore, Germany
Ketamine	100 mg/ml	PharmaWiki, Disentis, Switzerland
Lipopolysaccharid aus Escherichia coli O55:B5	L2880-10MG	Sigma Aldrich, Taufkirchen, Germany
Mayer's hemalum solution	2.5 l	Sigma Aldrich, Taufkirchen, Germany
May Grünwald solution	2.5 l	Sigma Aldrich, Taufkirchen, Germany
Methanol	assay ≥ 99.9 %	Sigma Aldrich, Taufkirchen, Germany
Medetomidinhydrochlorid	Dormilan® 1 mg/ml	Alfavet Tierarzneimittel GmbH, Germany
Midazolam	Dormicum® 5 mg/ml	Cheplapharm Arzneimittel GmbH, Greifswald, Germany
O.C.T. Compound	Tissue-PlusTM	Fisher Scientific GmbH Schwerte, Germany
Paraformaldehyde (PFA)	4 % in PBS	Thermo Fisher Scientific, Carlsbad, USA
Sodium Chloride	ACS reagent, assay ≥ 99.0 %	Merck Millipore, Germany
Sucrose	S0389-500G, assay ≥ 99.5 %	Sigma Aldrich, Taufkirchen, Germany
Tetrahydrofuran (THF)	assay ≥ 99.9 %	Sigma Aldrich, Taufkirchen, Germany
Toluidine blue O	C.I.52040	Merck Millipore, Germany
Trypan blue	0.4 %, sterile filtered	Sigma Aldrich, Taufkirchen, Germany
Trypsin-EDTA (1X)	0.25 %	Life Technologies Limited, Paisley, UK
Triton-X 100	TritonTM -X	SIGMA-ALDRICH GmbH
Tween®20	Viscous liquid	SIGMA-ALDRICH GmbH Steinheim, Deutschland

UltraPure™ distilled water	500 ml	gibco™ life technologies Thermo Fisher Scientific Carlsbad, USA
Xylazine	20 mg/ml	WDT, Garbsen, Germany
Xylol (Isomere)	assay ≥ 98.5 %	Carl Roth GmbH & Co. KG, Germany

Table 2.6: List of NPs

Name	Company
Melamine resin particles, 940 nm, Ex/Em 636 nm/686 nm	microParticles GmbH, Berlin, Germany
Qdot™ 655 ITK™ carboxyl quantum dots	Invitrogen by Thermo Fisher Scientific, Carlsbad, USA
Qdot™ 655 ITK™ amino (PEG) quantum dots	Invitrogen by Thermo Fisher Scientific, Carlsbad, USA

Table 2.7: List of antibodies and reagents

Antibodies	Clone	Company
Alexa Fluor® 488 anti-mouse Ly-6G Antibody	1A8	BioLegend, Fell, Germany
Antibodies for In Vivo Mouse Platelet Labeling (X649)	anti – GPIb beta derivative	Emfret Analytics GmbH & Co. KG, Würzburg, Germany
InVivoMAb anti-mouse LFA-1α (CD11a)	M17/4	Bio X Cell, Lebanon, USA
InVivoMAb anti-mouse/ human CD11b	M1/70	Bio X Cell, Lebanon, USA
InVivoMAb anti-mouse E-selectin (CD62E)	9A9	Bio X Cell, Lebanon, USA
InVivoMAbs rat IgG1 isotype control	HRPN	Bio X Cell, Lebanon, USA

InVivoMAbs rat IgG2a isotype control	2A3	Bio X Cell, Lebanon, USA
Purified anti-mouse TNF-α Antibody	MP6-XT22	BioLegend, Fell, Germany
Purified anti-mouse CD54 (ICAM-1) Antibody	YN1/1.7.4	American Type Culture Collection, Manasses, USA
Purified rat anti-mouse CD62P Antibody	RB40.34	BD Pharmingen, Germany
Rat Anti-CD62E antibody	UZ6 (ab2497)	Abcam, Cambridge, UK
Rabbit Anti-Prx antibody	HPA001868	Sigma-Aldrich, Merck KGaA, Germany
Ultra-LEAF™ Purified anti-mouse CD62L Antibody	MEL-14	BioLegend, Fell, Germany
Ultra-LEAFTM Purified Rat IgG2b, κ Isotype Ctrl Antibody	RTK4530	BioLegend, Fell, Germany

Table 2.8: List of mouse strain / cell line

Cell line / Strain	**Company**
C57BL/6(WT) mice	Charles River, Sulzfeld, Germany
HUVEC	PromoCell, Heidelberg, Germany

Table 2.9: List of kits

Name	**Company**
ATP assay kit	Sigma-Aldrich, Merck KGaA, Germany
BCA protein assay kit	ThermoFisher scientific, USA
Bio-Plex Pro Mouse Chemokine Panel 31-Plex	Bio-Rad Laboratories, California, USA
Masson's-Goldner Trichrome kit	Carl Roth GmbH & Co. KG, Germany

Quant-iT™ PicoGreen™ dsDNA Assay Kits and dsDNA Reagents	Invitrogen by Thermo Fisher Scientific, Carlsbad, USA

Table 2.10: List of software

Name	Company/Developers
BioPlex Manager 6.2 software	Bio-Rad Laboratories, California, USA
Fiji	Rasband, W.S., ImageJ, U. S. National Institutes of Health, Bethesda, Maryland, USA
GraphPad Prism 8.0	GraphPad Software, San Diego, California, USA
Imaris 9.1.0 software	Bitplane, Belfast, United Kingdom
R software (R-4.2.3)	R Core Team (2023). R Foundation for Statistical Computing, Vienna, Austria
Visiview software	Visitron Systems GmbH, Puchheim, Germany

2.2 Methods

2.2.1 Mice

Female C57BL/6 (WT) mice were purchased from Charles River (Sulzfeld, Germany) and were subsequently housed in the animal facility of the Helmholtz Zentrum München. The mice were kept in Individually Ventilated Cages (IVC) with unlimited free access to food and water and were maintained in a pathogen-free environment with constant temperatures ranging from 20-24 °C, 45-65 % humidity and a 12 h light cycle. Mice were exposed by instillation with a 0.1 ug/mouse dose of LPS (L2880-10MG, SigmaAldrich, Germany) for 24 h to induce acute lung inflammation or with 2 U/kg of Bleomycin sulfate (B5507-15UN, SigmaAldrich, Germany) for 14 days to induce pulmonary fibrosis. All experimental procedures were conducted on mice between 8 and 12 weeks old, in accordance with national guidelines, and approved by the Animal Welfare Ethics Committee of the local government of the Upper Bavarian Administrative Region (Regierung

von Oberbayern), under strict governmental and international guidelines, as per EU Directive 2010/63/EU.

2.2.2 Nanoparticles

2.2.2.1 Quantum dots

Qdot™ 655 ITK™ Carboxyl and Qdot™ 655 ITK™ Amino (PEG) QDs were procured from Invitrogen Corporation (Karlsruhe, Germany). They comprise a CdSe core, a ZnS shell, and additional amine residues on top of a PEG coating (aQDs) or carboxyl residues without any coating (cQDs). The hydrodynamic diameter of aQDs is measured to be 25.2 nm when suspended in Dulbecco's Phosphate Buffered Saline (DPBS, Gibco™ life technologies Thermo Fisher Scientific Carlsbad, USA), while the hydrodynamic diameter of cQDs is 18.1 nm (Praetner et al. 2010). Additionally, the emission wavelength of QDs is 655 nm. The QDs were dissolved in 50 µl of DPBS at a concentration of 1 pmol/g and administered via i.v. injection into the circulation of mice through the angular vein, utilizing a 1 ml insulin syringe (Becton, Dickinson and Company, Franklin Lakes, USA).

2.2.2.2 Melamine resin particles

Melamine resin particles (MF-FluoRed) were purchased from microParticles GmbH (Berlin, Germany). These particles have an excitation wavelength of 636 nm and an emission wavelength of 686 nm. They are synthesized by an acid-catalyzed polycondensation process in the presence of red fluorophores, utilizing melamine resin precursors in an aqueous solution. The discrete size of the MFs is 0.94 ± 0.05 µm. The MFs (2.5 % in stock solution) were diluted with UltraPure™ distilled water (Gibco™ life technologies Thermo Fisher Scientific Carlsbad, USA) at a 1:50 ratio to prepare a 0.05 % working solution. Prior to each experiment, the solution was well mixed, and 50 µl was administered intravenously per mouse.

2.2.3 In vivo application of fluorescent antibodies and blocking reagents

Mice were subjected to deep anesthesia by administering a triple compound of medetomidinhydrochlorid (1 mg/kg (body weight, BW), Dormilan® 1 mg/ml, Alfavet Tierarzneimittel GmbH, Germany), midazolam (10 mg/kg BW, Dormicum® 5 mg/ml, Cheplapharm Arzneimittel GmbH, Greifswald, Germany), and fentanyl (0.1 mg/kg BW, Fentanyl-Piramal® 0.05 mg/ml, Piramal Critical Care GmbH, Hallbergmoos, Germany) (MMF) via intraperitoneal (i.p.) injection. The body temperature of the mice was maintained at 37 °C using a heating pad (Harvard Apparatus, Massachusetts, United States). Additionally, an eye ointment was applied to relieve ocular discomfort during the anesthetized state. The fluorescent antibodies, blocking antibodies, and antagonists were injected intravenously into the mice via the angular vein 30 min prior to L-IVM utilizing a 1ml insulin syringe. All reagents were diluted in DPBS, in the appropriate proportions as specified.

Table 2.11: List of in vivo fluorescent dyes, blocking antibodies, and antagonists

Name	**Clone**	**Company**	**Dose**
A438079 hydrochloride (Competitive $P2X_7$ antagonist)	≥ 98 % (HPLC)	Bio-Techne GmbH, Germany	30 µg/mouse
Alexa Fluor® 488 anti-mouse Ly-6G antibody	1A8	BioLegend, Fell, Germany	3 µg/mouse
Antibodies for in vivo mouse platelet labeling (DyLight 649)	anti - GPIb-beta derivative	Emfret Analytics GmbH & Co. KG, Würzburg, Germany	2 µg/mouse
Cromolyn sodium salt	assay ≥ 95 %	Sigma Aldrich, Taufkirchen, Germany	0.2 µg/g (BW)
InVivoMAb anti-mouse LFA-1α (CD11a)	M17/4	Bio X Cell, Lebanon, USA	30 µg/mouse

InVivoMAb anti-mouse/human CD11b	M1/70	Bio X Cell, Lebanon, USA	30 µg/mouse
InVivoMAb anti-mouse E-selectin (CD62E)	9A9	Bio X Cell, Lebanon, USA	20 µg/mouse
InVivoMAbs rat IgG1 isotype control	HRPN	Bio X Cell, Lebanon, USA	30 µg/mouse
InVivoMAbs rat IgG2a isotype control	2A3	Bio X Cell, Lebanon, USA	30 µg/mouse
Purified anti-mouse TNF-α antibody	MP6-XT22	BioLegend, Fell, Germany	30 µg/mouse
Purified anti-mouse CD54 (ICAM-1) antibody	YN1/1.7.4	American Type Culture Collection, Manasses, USA	30 µg/mouse
Purified rat anti-mouse CD62P antibody	RB40.34	BD Pharmingen, Germany	20 µg/mouse
Ultra-LEAF™ purified anti-mouse CD62L antibody	MEL-14	BioLegend, Fell, Germany	20 µg/mouse
Ultra-LEAFTM purified Rat IgG2b, κ Isotype Ctrl antibody	RTK4530	BioLegend, Fell, Germany	20 µg/mouse

2.2.4 Lung intravital microscopy

2.2.4.1 Microscope

The intravital microscope utilized in this study was comprised of a VisiScope. A1 imaging system (Visitron Systems GmbH, Puchheim, Germany), fitted with a water dipping objective (20x, NA 1.0. Zeiss Micro Imaging GmbH, Jena, Germany), and a 16-color LED light source for fluorescence epi-illumination (pE-4000; CoolLED, UK). During the experiment, a quadband filter set (F66-014, DAPI/FITC/Cy3/Cy5 Quad LED ET Set; AHF Analysentechnik AG, Tuebingen,

Germany) was employed to excite QDs and Alexa488-labeled anti-Ly6G antibody at 40 % output power for 50 ms using the 470 nm LED module, while DyLight649-labeled anti-GPIb-V-IX complex antibody and MFs were excited at 40 % output power for 50 ms using the 655 nm LED module. The emissions from NPs and antibodies were separated by a beam splitter (T 580 lpxxr, Chroma Technology Corp, Bellows Falls, USA), and then captured by two Rolera EM2 cameras and processed using VisiView software (Visitron Systems GmbH, Puchheim, Germany).

2.2.4.2 Experimental protocol

The experimental procedure closely followed that of a previously published article by Headley et al. (Headley et al. 2016) (Fig.5). After being anesthetized deeply with MMF via i.p. injection, mice were kept on a temperature-controlled heating pad (12.0 x 20.5 cm, Harvard Apparatus, Massachusetts, USA) to maintain body temperature at 37 °C. Fluorescent antibodies and inhibitors were applied via i.v. injection 30 min prior to L-IVM. The left thorax hair was removed with a shaver (Aesculap Favorita II GT104, Aesculap AG, USA), and the skin of the left thorax and anterior neck was cleansed with 80 % ethanol before local anesthetization with Bucaine (50 µg/site, Puren Pharma). The anterior neck skin was subsequently cut with scissors to a 5 mm incision, and tweezers were used to bluntly separate the underlying tissue, thereby exposing the trachea. A small 20 G blunt catheter (Braun, Melsungen, Germany) was inserted into the incision in the trachea using Vannas Spring Scissors (Fine Science Tools, Hans Gawenda, Canada). The catheter was then connected to a small rodent ventilator (MiniVent, Harvard Apparatus, Massachusetts, United States) with a stroke volume of 10 µl/g (BW) and a breathing rate of 150 breaths/min under a positive end-expiratory pressure (PEEP) of 2~3 cm H_2O (~0.1 cm/g) with 100 % oxygen, thereby facilitating normal breathing patterns in mice. The mouse was placed in a lateral position on a heating platform, and a circular area of approximately 1 cm diameter comprising skin and muscle was excised from the left thorax. A 5 mm incision was then made between the 3rd and 4th ribs, and an intercostal insertion window with an 8 mm glass coverslip (VWR, Radnor, USA) was inserted into the chest.

To stabilize the surface of the lung against the intercostal insertion window, a custom system consisting of different manometers (Magnehelic. Dwyer Instruments. inc, USA) and a negative pressure pump (Nupro, St Willoughby, USA) provided a suction force of 20-25 mmHg. To maintain deep anesthesia, half of the initial dose of MMF (i.p.) was administered every 30 min. At the end of the L-IVM recording, which typically lasts for 60 min, the mice are sacrificed by abdominal aorta exsanguination.

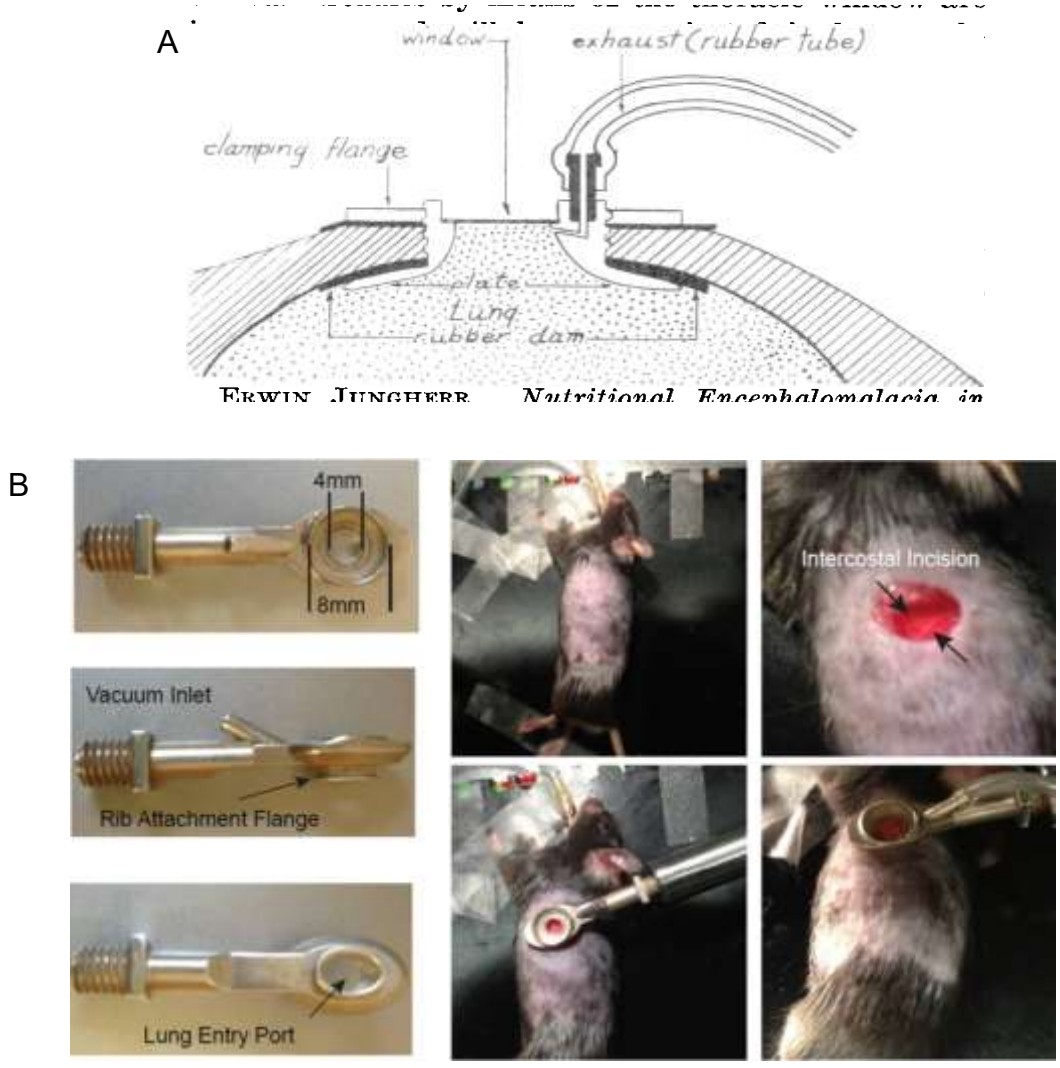

Figure 5. Vacuum stabilized imaging window.

(A) Schematic transverse section of a thoracic wall with a thoracic window adjusted, as first published in 1939 (Terry 1939). (B) Miniaturized negative pressure window for L-IVM in mice, as was used with minor modifications in this work. The thoracic window as well as the surgical procedure are depicted (Headley et al. 2016).

2.2.5 Measurement of L-IVM parameters

2.2.5.1 Quantification of neutrophils and platelets

Following completion of the thoracic surgery, the initiation of L-IVM imaging of the mouse was set as time point 0. To conduct quantitative analysis, 5 randomly selected field of views were recorded within the imaging window at 5-10 min intervals for the QDs, neutrophils, and platelet channels. The image was calibrated to a scale of 2.5 pixel/µm by Fiji software (Rasband, W.S., ImageJ, U. S. National Institutes of Health, Bethesda, Maryland, USA). The neutrophil count was quantified using the “Trackmate” plugin (Ershov et al. 2022) of Fiji, with an (estimated) object diameter of 13.7 µm. To determine the percentage of platelet-covered area, the “Threshold” function was used to select the area occupied by platelets, and the “Measurement” function was used to quantify the percentage of area covered by platelets.

To accurately measure the migration parameters of neutrophils in the lungs of mice, it is essential to obtain high-quality images without any excessive shaking or movement. To ensure high-quality imaging without any disturbance, a region was identified at 0 min to check the imaging quality. Thereafter, starting at 5 min, images of this region were captured every 5 s. The image displacement was rectified using the “Register virtual stack slices” plugin (Arganda-Carreras et al. 2006) of Fiji, utilizing the “Translation” feature extraction and registration models. The velocity and displacement of the neutrophils were subsequently analyzed using the "Trackmate" function of Fiji.

2.2.5.2 Blood perfusion velocity

After 1h of L-IVM, 50 µl of a 0.05 % working solution containing MFs (Ex/Em: 636 nm/686 nm) was administered intravenously to measure the blood perfusion velocity. Images were acquired using a fast acquisition mode at a rate of every 0.185 s. Blood perfusion velocity was determined by tracking the trajectory of MF fluorescence particles using the “Manual Tracking” plugin of Fiji. The sequential images were calibrated to a scale of 2.5 pixel/µm and the time interval was 0.185 s. This function provided a specific coordinate for the position of the beads at each time point.

2.2.6 Preparation of bronchoalveolar lavage (BAL) samples for Cytospin slides and May-Grünwald staining

2.2.6.1 BAL and Cytospins slide preparation

Upon completion of L-IVM imaging, the mice were sacrificed by abdominal aorta exsanguination, with the trachea still cannulated with a 20 G catheter. Subsequently, DPBS from a bottle which was positioned 20 cm above the mouse was instilled into the lung through the cannula and aspirated by pulling on the syringe barrel. The first 2 ml and the subsequent 8 ml of recovered bronchoalveolar lavage fluid (BALF) were collected separately and put into separate falcon tubes (Corning Incorporated New York, USA) on ice. The lavage fluid was then centrifuged (4°C, 20 min, 400 g), and the first 2 ml of supernatant was aliquoted and stored at -80°C for further analysis. The cell pellet obtained from all 10 ml of lavage fluid was resuspended in 0.5 ml of DPBS, and then the resulting cell suspension was diluted 1:10 in 0.2 % Trypan blue (Sigma Aldrich, Taufkirchen, Germany) and counted under a light microscope using a Neubauer counting chamber (BLAUBRAND®, Brand GmbH + Co. KG, Werthein, Germany). Only clear cells represent living cells, as Trypan blue can cross the membrane of dead cells and stain the cytoplasm blue. The cell concentration was calculated using the following formula.

$$\frac{\text{cells}}{\text{ml}} = \frac{\text{counted cells in 4 squares}}{\text{4 (counted squares)}} \times \underset{\text{(dilution factor)}}{10} \times \underset{\text{(Chamber factor)}}{10^4} \times \underset{\text{(total volume)}}{0.5}$$

A suspension of 3 x 10^4 BAL cells in 200 µl DPBS was loaded into each cytofunnel of a Cytospin™ Centrifuge (Cytospin 2, Thermo Shandon Ltd, UK) and centrifuged at 400 rpm for 6 min. The resulting cytospins were removed from the cytospin apparatus to obtain a monolayer of cells within the circular area of the slide and allowed to dry at room temperature for 2 h. The slides were then either frozen at -80 °C or stained directly.

2.2.6.2 May-Grünwald staining

The dried cytospin slides were stained with May-Grünwald according to the following protocol. First, the slides were incubated in May-Grünwald solution (Sigma Aldrich, Taufkirchen, Germany) for 10 min, followed by a 2-min rinse in tap water. The Giemsa stain (Sigma Aldrich, Taufkirchen, Germany) was then diluted 1: 20 with tap water to create a working solution. The slides were immersed in Giemsa working solution for 15 min, followed by one rinse in tap water and a 2-min soak in water. After air-drying overnight at room temperature, the slides were mounted with coverslips using Entellan® (Merck Millipore, Germany). Cell classification was performed using a bright-field microscope.

2.2.7 Lung tissue section

2.2.7.1 Lung tissue frozen section

After completion of L-IVM experiments, anaesthetized mice were humanely sacrificed through immediate abdominal aortic bleeding. The entire lung was isolated, and a 20 G catheter was inserted into the trachea. The lung was inflated with a mixture of 1 ml of cryo-embedded matrix (O.C.T, Cellpath, Newtown, England) and 4 % paraformaldehyde (PFA, Thermo Fisher Scientific, Carlsbad, USA) (1:2) through the catheter, followed by fixation in 4 % PFA at 4 °C overnight. After washing the lung three times with DPBS, it was immersed in a 30 % sucrose solution (S0389-500G, Sigma Aldrich, Taufkirchen, Germany) for dehydration until the lung sank to the bottom. Finally, the lung was embedded in O.C.T and stored at -80 °C. Subsequently, 6 µm slices of the lung were made using a Hyrax C50 cryostat (Zeiss, Jena, Germany).

2.2.7.2 Lung tissue paraffin section

In contrast to the frozen section protocol, the lung was inflated with 1 ml of 4 % PFA through the catheter and then fixed in 4 % PFA at 4 °C overnight. The lobes of the lung were sectioned into slices approximately 2 mm in thickness under the airing hood. The slices were then processed using an automatic benchtop tissue processor (Leica TP1020, Leica, Wetzlar, Deutschland) and embedded in paraffin using a Histostar device (Thermo Fisher Scientific, Carlsbad, USA) before being

stored at 4 °C. The embedded lung tissue was sliced into 3 µm sections using a Hyrax M55 rotary microtome (Zeiss, Jena, Germany).

2.2.8 3D lung imaging

Mice were deeply anesthetized with a mixture of xylazine (110 µg, WDT, Garbsen, Germany) and ketamine (10 mg, PharmaWiki, Disentis, Switzerland) (i.p.). The chest cavity was opened to expose the heart and lung, followed by making a small incision in the right ventricle. A 28 G needle attached to a syringe containing 30 ml of DPBS was inserted into the apex of the left ventricle to perfuse the pulmonary circulation system slowly with DPBS until the lung faded to white. The perfused lung was then fixed in 4 % PFA overnight. Optical clearance was performed as previously described (Yang et al., 2019). The fixed tissue underwent a series of incubation steps to prepare it for imaging. This involved incubation in 50 % Tetrahydrofuran/H_2O (THF, Sigma, Burlington, MA, USA) overnight, followed by a stepwise increase in THF concentration (50 %, 80 %, and 100 %) for 1 h each at room temperature, followed by immersion in 100 % THF overnight and for an additional hour on the next day. Subsequently, samples were incubated in Dichloromethane (DCM, Sigma, Burlington, MA, USA) for approximately 20-40 min and finally immersed in dibenzyl ether (DBE, Sigma, Burlington, MA, USA) for at least 4-6 h until imaging. Imaging was performed using a light sheet fluorescence microscope (LSFM, Ultramicroscope II, LaVision Biotec) equipped with an sCMOS camera (Andor Neo, Abingdon, United Kingdom), a 2x objective lens (Olympus MVPLAPO 2×/0.5 NA) and an Olympus MVX-10 zoom body with a zoom range from 0.63x to 6.3x. The samples were submersed in DBE and imaged at varying magnification levels, with imaging steps of 5-10 µm, depending on the size of the sample. QDs were excited at 470 ± 30 nm and emission detected at 640 ± 30 nm, while lung autofluorescence was excited at 520 ± 40 nm and detected at 585 ± 40 nm, with an exposure time of 100 ms, at 95 % laser power. LSFM images was acquired and processed using Imaris 9.1.0 software (Bitplane, Belfast, United Kingdom).

2.2.9 Blood analysis

One hour after i.v. administration of QDs, the mice were anesthetized with 100 µl of a mixture of xylazine and ketamine (i.p.) until they no longer responded to painful stimuli. Blood samples were collected from the angular vein using a microcapillary pipette (Hirschmann Minicaps, Laborgeräte GmbH & Co. KG, Germany) and 50 µl of blood were collected into an EDTA-coated disposable plastic capillary pipette (Kabe Labortechnik GmbH). A complete hematology analysis, including numbers of white blood cells (WBC), platelets, erythrocytes related parameters, and percentages of different WBC, was performed using a Hematology Analyzer (IDEXX ProCyte, USA).

2.2.10 Bio-Plex Pro Mouse Chemokine Panel 31-Plex

After i.v. administration of QDs for 1 h or 24 h, and instillation of LPS for 4 h, blood was collected as described in section 2.2.9. The collected blood was then centrifuged at 1000 g for 15 min at 4 °C to obtain the supernatant, which was plasma. To remove platelets and precipitates, the plasma was centrifuged again at 10000 g for 10 min at 4 °C, and the resulting plasma supernatant was stored at -80 °C for further analysis. The quantification of 31 chemokines was conducted according to the manufacture's protocol for the Bio-Plex Pro Mouse Chemokine Panel 31-Plex (Bio-Rad Laboratories, California, USA). Briefly, the coupled beads were diluted with Bio-Plex assay buffer to 1x. Subsequently, 50 µl of diluted beads were added to the assay plate and washed twice using wash buffer. Next, 50 µl of serum samples (diluted 1:5 in samples diluent) standards, blank, and control were added and incubated at room temperature for 30 min. After three washing steps, 25 µl of detection antibodies were added to each well and incubated at room temperature for 30 min. Following three washing steps with wash buffer, SA-PE (50 µl) was added to each well and incubated in the dark at room temperature for 10 min. Finally, the plate was then washed three times to remove SA-PE and the beads were resuspended in 125 µl assay buffer and shaken for 30 seconds prior to reading on the Luminex™ 200 (Invitrogen™, Thermo Fisher Scientific, Carlsbad, USA) and the BioPlex Manager 6.2 software (Bio-Rad Laboratories, California, USA). A heatmap with hierarchical clustering analysis based on relative abundancies of chemokine concentrations was performed using "z score" and

“pheatmap” packages (Kolde R, 2019, R package version 1.0.12) in R software (R-4.2.3).

2.2.11 dsDNA detection assay

The quantification of dsDNA levels was conducted as per the manufacture’s protocol for the Quant-iT™ PicoGreen™ dsDNA Assay Kits (Invitrogen by ThermoFisher Scientific, Carlsbad, USA). Briefly, 20 µl of BALF samples, 80 µl of 1x Tris EDTA (TE) buffer, and 100 µl of a mixture of PicoGreen reagent and TE buffer (1:200) were added to a black 96-well microplate (Greiner Bio-One GmbH, Frickenhausen, Germany). The plate was agitated for 3 min, protected from light, and subjected to excitation at 475 nm and emission at 510-550 nm using a fluorescence microplate reader (Tecan Safire 2, TECAN Group Ltd. Männdorf, Switzerland).

2.2.12 BCA protein assay

Protein levels were determined using the BCA protein assay kit (ThermoFisher scientific, USA) as per the manufacturer’s instructions. In brief, 20 µl of BALF was added to a 96-well plate, and a mixture of solution A and B (50:1) was added in a volume of 200 µl. The plate was incubated at 37 °C for 30 min, shielded from light, and the absorbance was measured at 562 nm using a spectrophotometer. (TECAN Infinite® M200 PRO, TECAN Group Ltd. Männdorf, Switzerland).

2.2.13 Histology staining

2.2.13.1 Haematoxylin and Eosin staining (H&E)

Step 1. The paraffin slices were placed in a 37 °C incubator for at least 2 h, and then processed to deparaffinization as described below (Table 2.12).

Table 2.12: Deparaffinization step

Chemicals	Time
Xylol	5 min
Xylol	5 min

100 % Ethanol	1 min
100 % Ethanol	1 min
90 % Ethanol	1 min
80 % Ethanol	1 min
70 % Ethanol	1 min

Step 2. The slices were processed with Mayer's Hemalum solution (Sigma Aldrich, Taufkirchen, Germany) and Eosin solution (Carl Roth GmbH & Co. KG, Germany) according to the following protocol (Table 2.13).

Table 2.13: Mayer's Hemalum and Eosin solution staining step

Chemicals	Time
Distilled water	1x dip briefly
Mayer's Hemalum (filtered)	5 min
Tap water	1x dip briefly
0.1 % Hydrochloric acid (HCL)-Ethanol (2 ml 32 % HCL with 200 ml 70 % Ethanol)	1x dip briefly
Tap water	10 min
Distilled water	1x dip briefly
0.5 % Eosin solution (filtered)	8 min

Step 3. The stained slices were dehydrated using a series of ethanol solutions with increasing concentrations (Table 2.14) and were subsequently covered with Entellan® before being mounted with coverslips.

Table 2.14: Dehydration step

Chemicals	Time
70 % Ethanol	1x dip briefly
80 % Ethanol	1x dip briefly
90 % Ethanol	1x dip briefly
96 % Ethanol	1x dip briefly

100 % Ethanol	1~2 min
100 % Ethanol	1~2 min
Xylol	5 min
Xylol	5 min

In general, the nuclei of cells stained with H&E exhibit a blue hue, whereas other elements of the lung tissue show a rose-red color.

2.2.13.2 Masson’s-Goldner Trichrome staining

The paraffin slices were deparaffinized and dehydrated using the same method as described in section 2.2.13.1, step 1 and 3. Step 2 of Masson’s-Goldner Trichrome staining (Carl Roth GmbH & Co. KG, Germany) was performed as outlined in Table 2.15. Finally, the stained slices were covered with Entellan® and mounted with coverslips.

Table 2.15: Masson’s-Goldner Trichrome staining step

Chemicals	Time
Weigerts Ironhematoxylin	10 min
Tap water	1x dip briefly
0.1 % HCL-Ethanol (2 ml 32 % HCL with 200 ml 70 % Ethanol)	1x dip briefly
Running tap water	12 min
Distilled water	1x dip briefly
Goldner Stain I (Ponceau - Acidfuchsin red)	5 min
1 % Acetic acid	30 s
Distilled water	1x dip briefly
Goldner Stain II (Phosphormolybdemic acid)	8 min
1 % Acetic acid	30 s
Goldner Stain III (Lighgreen)	15 min
1 % Acetic acid	30 s

Distilled water	1x dip briefly

Overall, collagen fibers are depicted in green, while the nuclei of cells stained with Weigerts Iron hematoxylin shows a dark brown color, and other elements of the lung tissue such as cytoplasm and muscle fibers appear red.

2.2.13.3 Toluidine blue staining

To prepare the Toluidine Blue solutions, 1 g of Toluidine blue O (C.I.52040, Merck Millipore, Germany) was mixed thoroughly with 100 ml of 70 % alcohol to create the Toluidine Blue stock solution. Additionally, 0.5 g of Sodium Chloride (ACS reagent, ≥ 99.0 %, Merck Millipore, Germany) was mixed with 50 ml of distilled water (UltraPure™ Dnase/RNnase, Invitrogen™, USA), and the pH value was measured using a laboratory pH sensor (SevenEasy pH, Mettler-Toledo GmbH, Switzerland). It was then adjusted to a range of 2.0-2.5 using HCL (32 %, Merck Millipore, Germany), resulting in a 1 % Sodium Chloride solution. To create the Toluidine Blue working solution, 5 ml of the Toluidine Blue stock solution was mixed with 45 ml of freshly prepared 1 % Sodium Chloride solution. It is important to maintain a pH value of 2.0-2.5 in the working solution to achieve a strong contrast.

The lung slices were subjected to the deparaffinization protocol described in section 2.2.13.1, step 1. Following this, the slices were washed in running water for 2 min and then immersed in the Toluidine Blue working solution for 2 min. Afterward, they were washed in distilled water for 2 min. The stained slices were further processed in the dehydration step as described in 2.2.13.1, step 3. Finally, the slices were covered with Entellan® and mounted with coverslips. This staining technique is utilized to identify the metachromasia of mast cells, which display violet/red-purple metachromatic granules against a blue background tissue.

2.2.13.4 Immunofluorescence staining

Frozen slices were rinsed in DPBS solution containing 0.1 % Tween®20 (SIGMA-ALDRICH GmbH Steinheim, Deutschland) for 3 times, each for a duration of 2 min. Subsequently, the slices were blocked using DPBS solution comprising of

5 % normal goat serum and 0.3 % TritonX-100 (SIGMA-ALDRICH GmbH) for 1h, followed by incubation with primary antibodies (Table 2.16), which were suitably diluted in antibody diluent solution comprising of DPBS solution with 1 % BSA and 0.3 % TritonX-100, at 4 °C overnight. Next, the slices were treated with secondary antibodies and DAPI for 1 h, both of which were diluted (1:1000) in antibody diluent solution. Each step was followed by a washing step in DPBS solution containing 0.1 % Tween®20 for 3 times, each for 5 min. Eventually, the stained slices were mounted using DAKO fluorescence mounting medium (Dako Omnis, Agilent, Santa Clara, USA) and covered with coverslips.

Table 2.16: Information of antibodies

Antibody	Detection system	company	Dilution
Anti-CD62E antibody	Rat	Abcam, Cambridge, UK	1:250
Anti-Prx antibody HPA001868	Rabbit	Sigma-Aldrich, Merck KGaA, Germany	1:500

2.2.14 Statistical evaluation

All data were presented as mean ± standard error of the mean (SEM) and plotted using GraphPad Prism 8 (GraphPad Software Inc., La Jolla, USA), with the sample size and number of repeats indicated in the figure legends. For normally distributed data, a two-sided Student's t-test was used for comparison between two groups and if the variances were unequal, a Welch's t-test was used instead, while for nonparametric data, the Mann-Whitney rank-sum test was used. Comparisons among multiple groups were performed using a One-way or Two-way ANOVA with Tukey's comparisons test. Significances levels were defined as follows: $P < 0.05$ (*), $P < 0.01$ (**), $P < 0.001$ (***), and $P < 0.0001$ (****), while p-value ≥ 0.05 were considered not significant (ns).

3. Results

3.1 L-IVM and histology of lung in healthy, LPS-, and Bleomycin-treated mice

To investigate the impact of i.v. administration of NPs on the interaction of neutrophils and platelets with pulmonary microvessels under physiologic and pathophysiologic conditions, we utilized mouse models of LPS (0.1 ug/mouse) induced acute lung inflammation and Bleomycin (2 U/kg) induced pulmonary fibrosis in addition to healthy mice. Prior to the actual NPs application experiments, lung physiology and pathophysiologic condition of these mice has been examined.

3.1.1 Imaging and quantitative analysis of neutrophils

Before L-IVM, mice were injected intravenously with Alexa488-labeled anti-Ly6G antibody which directly labels vascularly localized neutrophils in vivo. Images were recorded immediately after surgical insertion of the thoracic window and were taken every 5 to 10 min for 1h. At each time point, 5 areas were randomly selected for further analysis. Representative L-IVM images of healthy (control), LPS-treated and Bleomycin-treated mice at 0 and 60 min are shown in Fig.6 A. The lung structure in these microscopic images is clearly visible in healthy mice and in mice with acute lung inflammation, whereas in the fibrotic lung, the images of the tissue structure appear impaired due to diffuse interstitial changes. At the beginning of L-IVM (t=0), the neutrophil numbers in the microvascular among the three conditions were similar, only a little lower in LPS-treated mice (Fig.6 B).

The suction-based L-IVM has been proven to induce minimal early inflammation, and any inflammation induced by the method may be attributed to the experimental duration, as it may become obvious over 6 h (Looney and Headley 2018). As shown in Fig 6. A and B, a slight increase in neutrophil numbers over 60 min occurred in the control (healthy) group that was considered as the baseline level. Neutrophil numbers in fibrotic mice did not differ from those in the control group. However, in LPS-treated (24 h) mice, recruited neutrophils increased during L-IVM, probably caused by the microsurgery as a second hit, after a previous presensitization caused by the LPS stimulation. At 60 min, neutrophil numbers were

3.56 ± 0.18 /10^4µm ^{2} which was significantly increased as compared to the control group (2.37 ± 0.16 /10^4µm^2).

Taken together, in healthy mice or Bleomycin-treated mice, neutrophil recruitment in alveolar microvessels was not induced during L-IVM. But after LPS stimulation, the mice undergo an immune response as a result of the L-IVM process, which might be considered as a second hit. Under acute pathophysiologic conditions, the initial insult (LPS stimulation) primes the immune system, making it more responsive to the subsequent L-IVM process. This immune response can potentially impact the behavior and functional responses of immune cells in the pulmonary microcirculation.

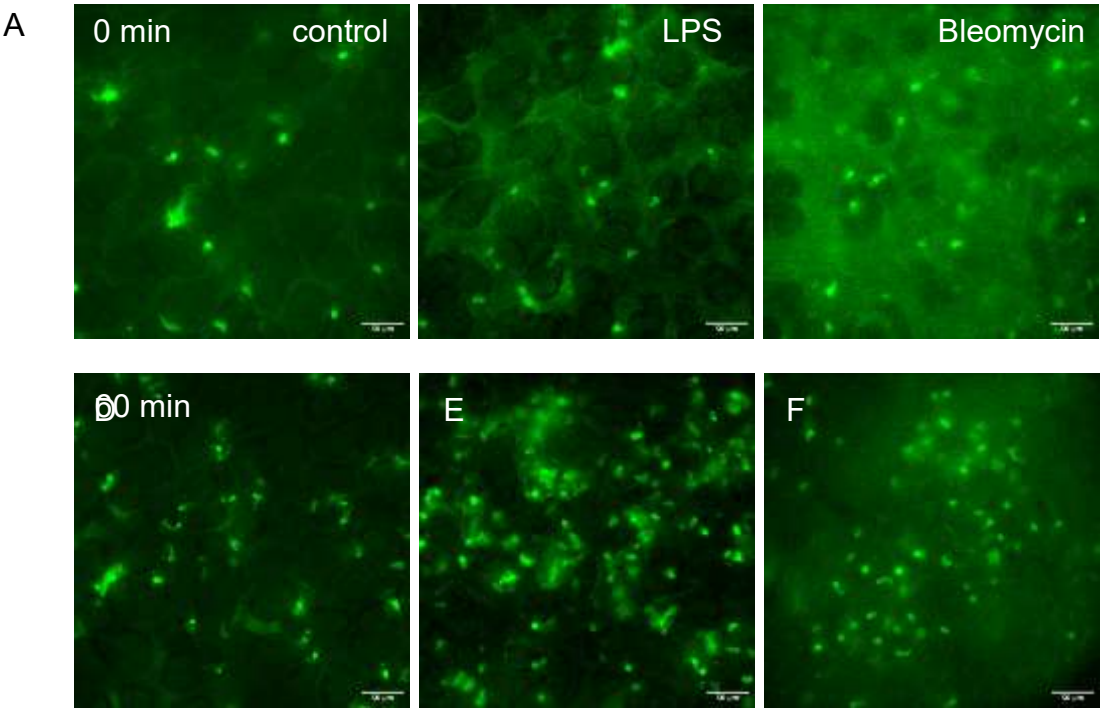

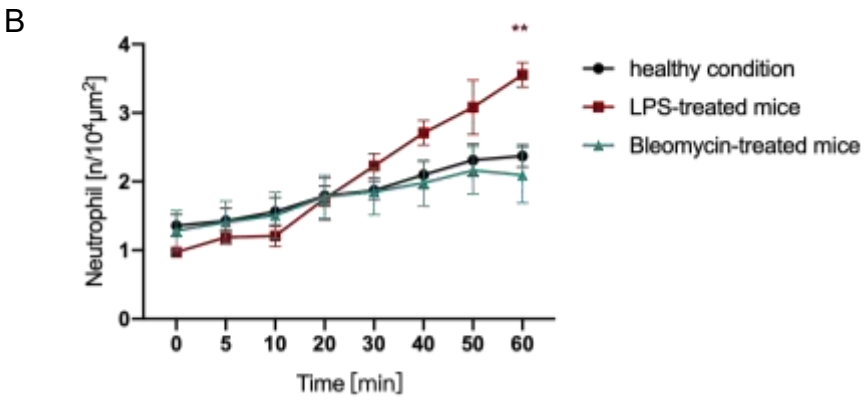

Figure 6. Representative L-IVM images and quantification of time trends of neutrophils in the pulmonary microcirculation of healthy, LPS-treated, and Bleomycin-treated mice.

Representative L-IVM images. (A) The upper images depict neutrophils (green) in the pulmonary microcirculation from healthy, LPS-treated (24 h), and Bleomycin-treated (14 d) mice at the start (0 min) of recording after chest surgery. The lower row shows the timepoint of 60 min. Neutrophils were directly labeled in vivo by i.v. application of Alexa488-labeled anti-Ly6G Abs, depicted in bright green points. The autofluorescence outlining alveolar and vascular structures is dark green (Scale bar: 50 µm). (B) The changes in neutrophil numbers during 60 min of L-IVM were quantified and shown. (mean ± SEM, n = 4 mice/group, red * LPS-treated mice vs control group, Two-way ANOVA test).

3.1.2 Imaging and quantitative analysis of platelets

To image platelet dynamics, DyLight649-labeled anti-GPIb-V-IX complex was injected intravenously before L-IVM to label platelets. Representative images of platelets in the pulmonary microcirculation in the 3 models are shown in Fig.7 A - C. The platelets evenly flow through the microvessels in healthy condition, whereas at the beginning of the L-IVM process in LPS-treated mice, some large clusters of platelets appeared, which subsequently broke up into small pieces flowing into different following vessels, as visible in the time lapse of Fig.7 B1 - B4. In Bleomycin-treated mice (Fig.7 C), the area covered by platelets was increased as compared to the other conditions. Therefore, we measured the percentage of platelet-covered areas per field of view to quantify the platelet covered area over time in the different conditions (Fig.7 D). Except at the first timepoint in LPS-treated mice, the platelet containing areas did not increase during the process of observation. However, in Bleomycin-treated mice, platelet containing areas in the microcirculation were already increased at early timepoints and increased more during the duration of L-IVM.

The circulating fluorescent platelets clearly indicate alveolar borders and the thickness of the surrounding (interstitial) tissue. Diameter of 15 alveoli and 20 alveolar interstitial spaces were randomly measured per mouse in each group of 4 mice. In Fig.7 D, the alveolar size in healthy and LPS-treated mice were similar (47.5 ± 1.60 µm and 47.17 ± 1.18 µm), however it was decreased significantly at a value of 42.33 ± 1.14 µm in Bleomycin-treated mice. As visible in Fig.7 E, after

LPS treatment for 24 h, there was not much change in lung tissue structure, alveolar septal thickness was similar (17.44 ± 0.86 µm) as compared to healthy mice (17.21 ± 0.82 µm). The alveolar septal thickness in fibrotic mice was significantly increased to 39.90 ± 2.27 µm.

In summary, compared with healthy mice, LPS-treated mice exhibit large clusters of platelets present at the beginning of the L-IVM process which then separate into fragments that circulate in the pulmonary microcirculation. In fibrotic lungs, the altered tissue structure can be differentiated from the other conditions by L-IVM i.e., increased platelet positive areas, increased alveolar interstitial space and reduced alveolar diameter.

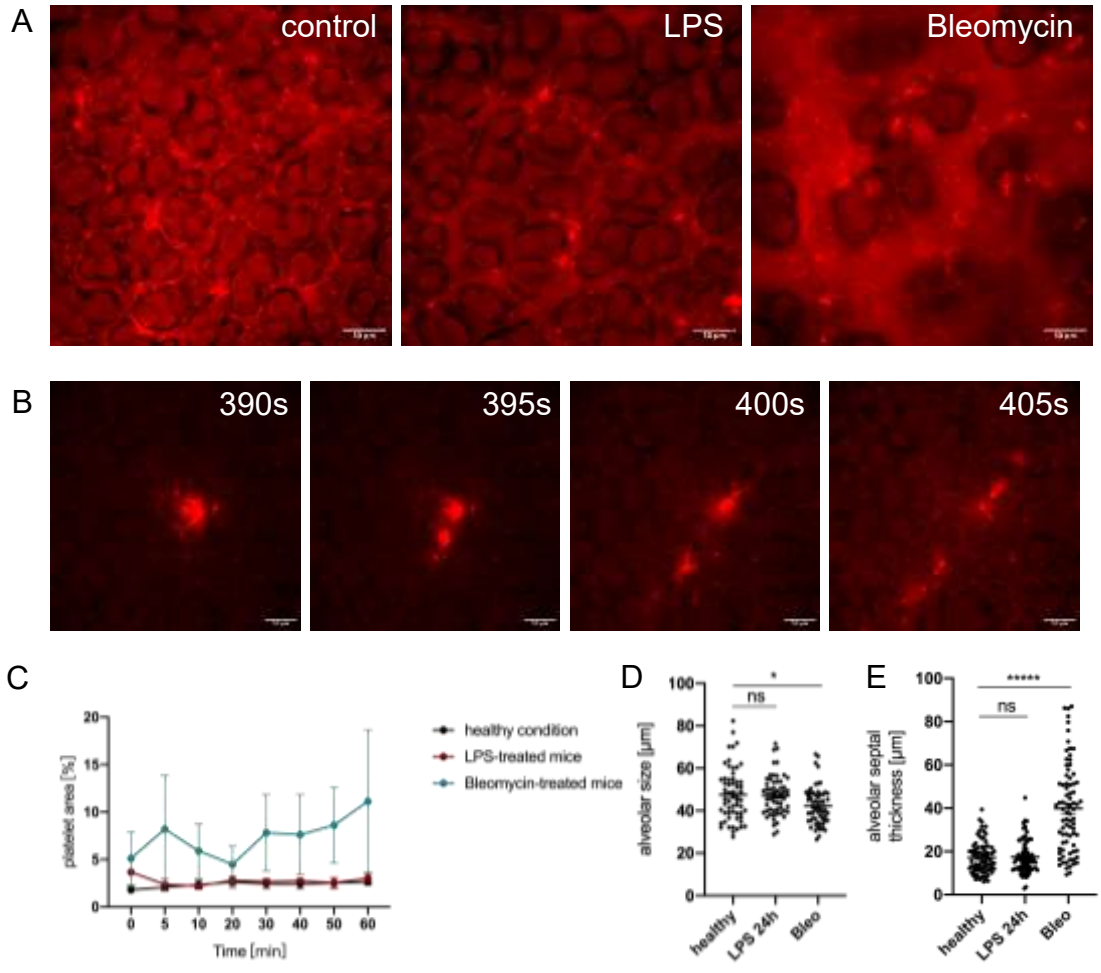

Figure 7. Representative platelet images and quantification of platelet dynamics in the pulmonary microcirculation of healthy, LPS-, and Bleomycin-treated mice.

Representative images of platelets recorded by L-IVM. (A) The images show platelet patterns in the pulmonary microcirculation of healthy, LPS-, and Bleomycin-treated mice. (B) The time lapse of platelet changes in LPS-treated mice is shown. Platelets were directly labeled by

DyLight649-conjugated anti-GPIb-V-IX complex, depicted in bright red points. The autofluorescence of alveolar and vascular structures appears dark red. (Scale bar: 50 µm). (C) The percentages of the platelet covered area in field of views [%] during 60 min of L-IVM were quantified. (D) The alveolar size, (E) and the alveolar septal thickness under the three conditions were quantified. (mean ± SEM, n = 3~4 mice/group, One-way/Two-way ANOVA test).

3.1.3 Analysis of BAL parameters

At the end of the L-IVM observation procedure, mice were lavaged to obtain BAL cells and supernatants, allowing for further exploration of the immune status in the bronchial and alveolar environment. BAL cells were collected by Cytospin preparation and analyzed by May Grunwald-Giemsa staining to determine the cell types. After 24h of LPS instillation for acute lung injury, the total number of BAL cells increased to 1.59 ± 0.13 x 10^6, as compared to 0.27 ± 0.01 x 10^6 cells recovered from healthy mice. Neutrophil numbers increased significantly (118.50 ± 15.59 x 10^4 vs 0.19 ± 0.07 x 10^6), whereas there was little change in macrophages, monocytes, or lymphocytes. In Bleomycin-induced fibrosis (14 d), the amount of BAL cells increased to 2.26 ± 0.27 x 10^6. Neutrophils remained at levels similar to those in healthy mice, whereas the levels of alveolar macrophages, lymphocytes, and monocytes were significantly higher than in healthy mice (Fig.8).

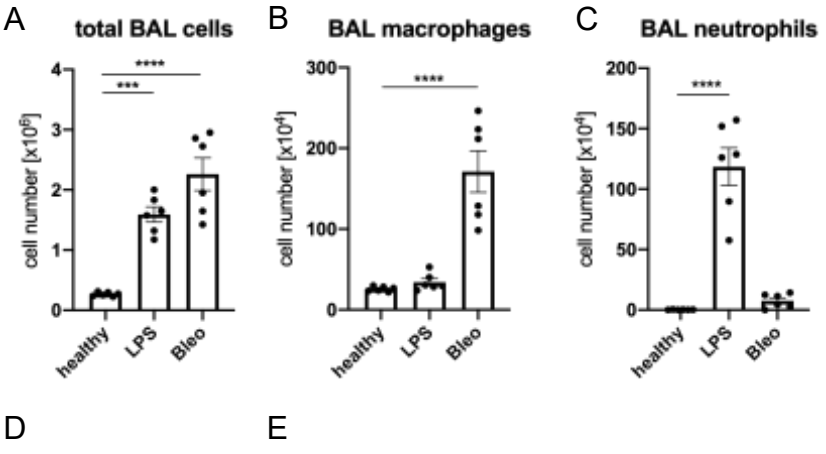

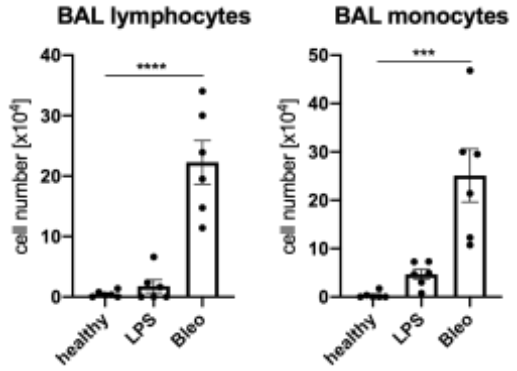

Figure 8. Quantification and classification of BAL cells of healthy, LPS-treated, and Bleomycin-treated mice.

Quantification of total BAL cells (A), macrophages (B), neutrophils (C), lymphocytes (D), and monocytes (E) after L-IVM. May Grunwald-Giemsa stained cytospins of BAL cells were analyzed. (mean ± SEM, n = 6 mice/group, One-way ANOVA test).

In addition, the first 2 ml of BALF supernatant was collected from mice after 1 h L-IVM and levels of protein and free double stranded DNA (dsDNA) have been analyzed. As depicted in Fig.9 A, there were no significant differences in protein levels between the healthy (0.16 ± 0.03 mg/ml) and LPS-treated group (0.29 ± 0.04 mg/ml). After 14 d of Bleomycin treatment, the protein levels in BALF supernatant were significantly increased to 0.98 ± 0.22 mg/ml. dsDNA levels increased to 82.67 ± 18.20 ng/ml after 24 h of LPS treatment compared to the healthy individuals at 4.71 ± 1.10 ng/ml, while dsDNA levels in the Bleomycin-treated group were only slightly increased (11.51 ± 1.42 ng/ml) (Fig.9 B).

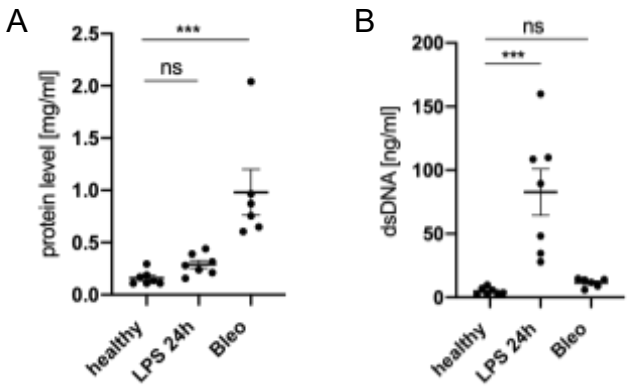

Figure 9. dsDNA and protein levels detected in BALF supernatants.

The first 2 ml of BALF supernatant was collected and assessed by BCA protein assay kit and PicoGreen dsDNA assay kit. The protein (A) and dsDNA (B) levels in the three conditions are shown. (mean ± SEM, n = 6~7 mice/group, One-way ANOVA test).

Overall, our analysis of the BAL samples demonstrated that neutrophils were enriched in the broncho-alveolar space, along with increased dsDNA levels, following LPS stimulation, which aligned with our intended model of acute lung injury (ALI). In the context of Bleomycin-induced fibrosis, we observed alterations in BAL cell numbers, including macrophages, lymphocytes, and monocytes, as well as changes in protein levels and thickening of the alveolar walls.

3.1.4 Histological investigation of lung structure

To identify histologic alterations of the lung structure, H&E staining for healthy and LPS-treated mice and Masson's-Goldner Trichrome staining for Bleomycin-treated mice were applied. After lavage, lungs were isolated and kept as paraffin section for further staining. In Fig.10, H&E staining shows that the general lung structure was not changed in LPS-treated mice (Fig.10 B) as compared to the healthy condition (Fig.10 A). The use of Masson's-Goldner trichrome stain aimed to detect the accumulation of collagen in smooth muscle, since collagen synthesis predicts the progression of fibrosis. Fig.10 D shows that Bleomycin treatment induced pulmonary fibrosis in mice, as evidenced by an increase in collagen-positive areas around the trachea and increased alveolar septal thickness.

A

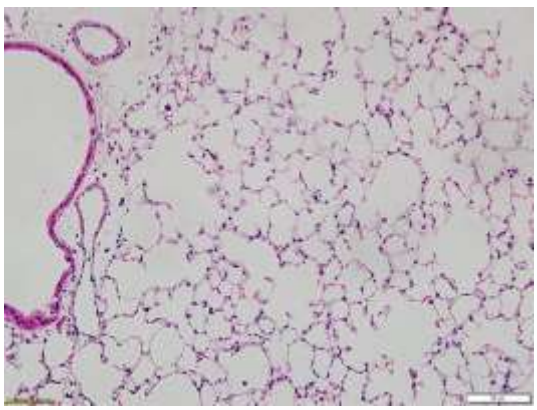

B

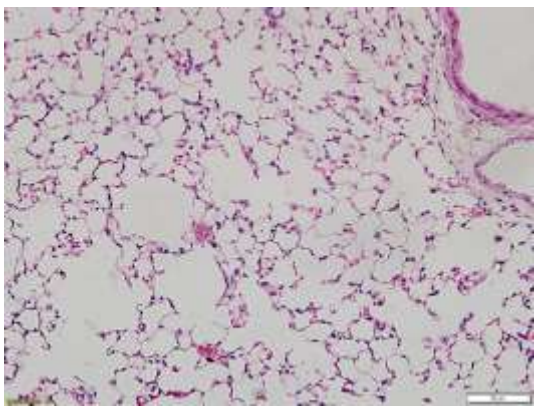

C

D

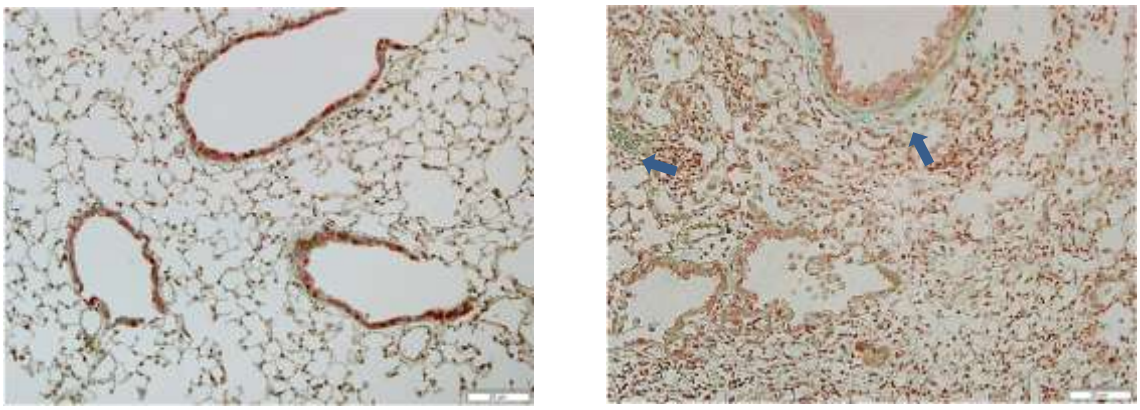

Figure 10. Representative images of H&E stains and Massons-Goldner Trichrome collagen stains on different conditions.

Images of H&E lung tissue staining from healthy (A) and LPS-treated (B) mice are shown. Masson's-Goldner Trichrome stain of lung tissue from the healthy condition (C) and Bleomycin-treated mice (D) demonstrates the establishment of lung fibrosis. This condition is characterized by the accumulation of massive extracellular matrix components, including collagen deposition, and thickened alveolar septa. Collagens (green color) are highlighted by blue arrows; nuclei are shown in dark brown; muscle fibers are in bright red; and erythrocytes and cytoplasm are represented in red/orange color. (Scale bar: 20/50 μm).

3.2 Different patterns of QDs interaction with endothelial cells in vitro

Based on the different characteristics of QDs, in vitro experiments were conducted to investigate the interactions of QDs with endothelial cells. We used different surface modified quantum dots, i.e., cQDs and aQDs which are semiconductors of a size of ca. 20 nm with intrinsic specific fluorescence and are clearly visible in vivo and in vitro. cQDs have been shown to be taken up very efficiently by macrophages as well as endothelial cells in vivo and in vitro, in contrary to aQDs (Praetner et al. 2010; Rehberg et al. 2010; 2012; 2016). Human umbilical vein endothelial cell line (HUVEC) cultures were utilized to observe and analyze the behavior of these different modified QDs at the cellular level. HUVEC were cultured and incubated with different modified QDs for 1 h. Consistent with the previous reports, cQDs, which have a strong protein binding capacity (Fig.2), were observed to be taken up by HUVEC cells after 1 h. However, almost no uptake of aQDs, which show weak interactions with biomolecules (Fig.2), was

observed in the HUVEC cells. These findings are in line with our previous studies (Praetner et al. 2010; Rehberg et al. 2010; 2012; Nekolla et al. 2016) and confirm that the QDs used in this study exhibit similar interactions with endothelial cells as previously reported. This allows for a comparison of their behavior in the pulmonary microcirculation, as investigated in this thesis, with their interactions and effects in the skeletal muscle. Furthermore, the results emphasize the significance of the biomolecule binding ability of QDs in influencing their cellular uptake and underscore the importance of understanding their interactions with biological systems.

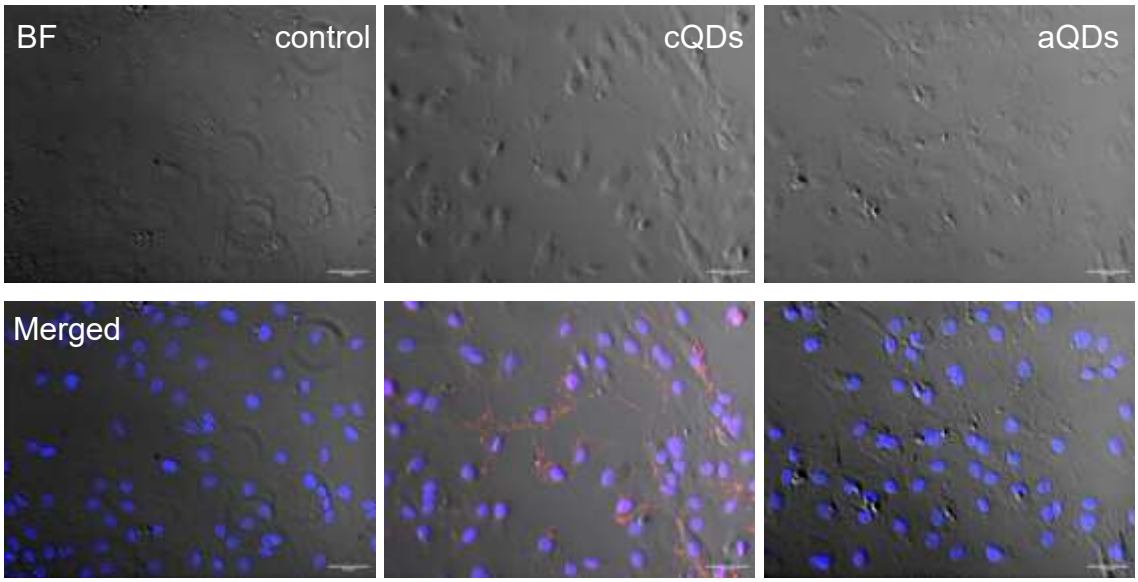

Figure 11. Representative images of QDs uptake by HUVEC.

Endothelial cells (HUVEC) were incubated with cQDs and aQDs for 1 h, followed by fixation with 4 % PFA for IF staining. The uptake of cQDs by HUVEC was confirmed using fluorescent microscopy, with QDs depicted in red, nuclei stained (DAPI) in blue, and the bright filed image shown in grey. (Scale bar: 50 µm).

3.3 Distribution of QDs in healthy murine lungs after i.v. application

3.3.1 Detection of QDs dynamics in healthy mice after i.v. application using intravital microscopy

Next, we investigated dynamics and distribution of QDs in the murine pulmonary microcirculation. Prior to L-IVM, DyLight649-labeled anti-GPIb-V-IX complex Abs and Alexa488-labeled anti-Ly6G Abs were applied via the angular vein. The surgery was typically performed in 15 min and immediately after the microscopy recording started (baseline t=0 min). At 5 min, the QDs (1 pmol/g) were i.v. injected. During the observation time, images of QDs distribution in the lung microcirculation were captured. After i.v. application, QDs fluorescence was homogenously present in the microvessels. In addition, some small cQDs containing fluorescent clusters circulated in the microcirculation and part of them gradually interacted with the endothelium in the early phase that the association was stable for 60 min (Fig.12 A and C). Positive stretches of cQDs along microvessel walls indicate cQDs uptake by endothelial cells. However, as shown in Fig.12 B, some big and immobile clusters, containing aQDs appeared in capillaries and remained immobile for the whole observation time. At each time point, 10 aggregate free areas in the lumen of microvessles were randomly selected for analysis of QDs kinetics in the blood by monitoring fluorescence intensity. As revealed in Fig.12 D, the intensity of both QD types in the circulation was reduced almost to background levels at 60 min.

A

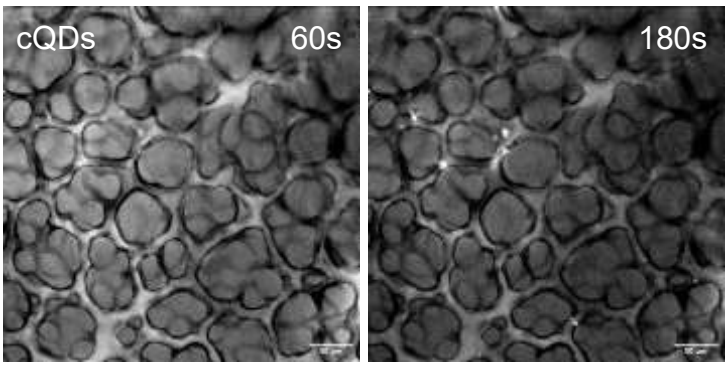

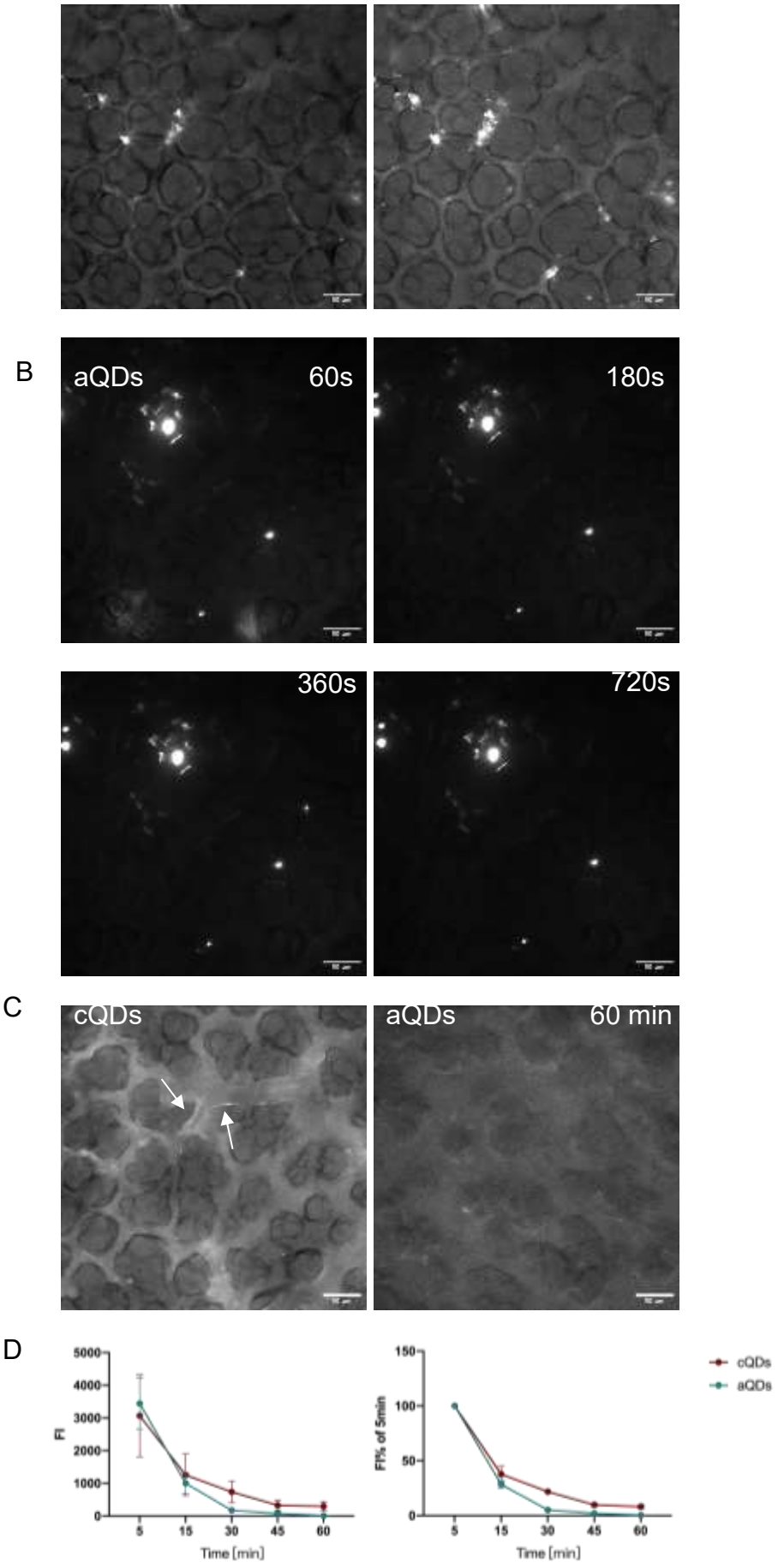

Figure 12. Time lapse of QDs detection in lung microcirculation via L-IVM.

Time lapse of cQDs (A) and aQDs (B) clustering within pulmonary microvessels via L-IVM at an early stage. The QD clusters are depicted with bright white (Scale bar: 50 µm). (C) Representative L-IVM images of cQDs and aQDs at 60min (without clusters) indicate, that cQDs are taken up by endothelial cells in some microvesses (white arrow). (D) Quantification of fluorescence intensity in the lumen of blood vessels. (mean ± SEM, n = 4 mice/group).

3.3.2 Visualization of QDs distribution in murine whole lungs with tissue optical clearing associated with 3D imaging

To study the exact distribution of QDs in the pulmonary microcirculation, 3D light sheet microscopy of the entire lung structure was employed. After the process of L-IVM, the murine lungs were perfused with DPBS to remove as much blood as possible, followed by the tissue optical clearing process. In Fig.13, 3D imaging of a healthy murine lung with autofluorescence is depicted. The whole lung and bronchial contouring were clearly visible in the (magnified) images. In mice treated with cQDs, only a few fluorescent cQDs points were observed in the periphery of the lung. The tissue structure appeared less clearly outlined compared to the control lung. On the other hand, aQDs spots were clearly detected and scattered throughout the lung. Additionally, prominent aggregates of aQDs were localized in the blood vessels surrounding the main bronchi.

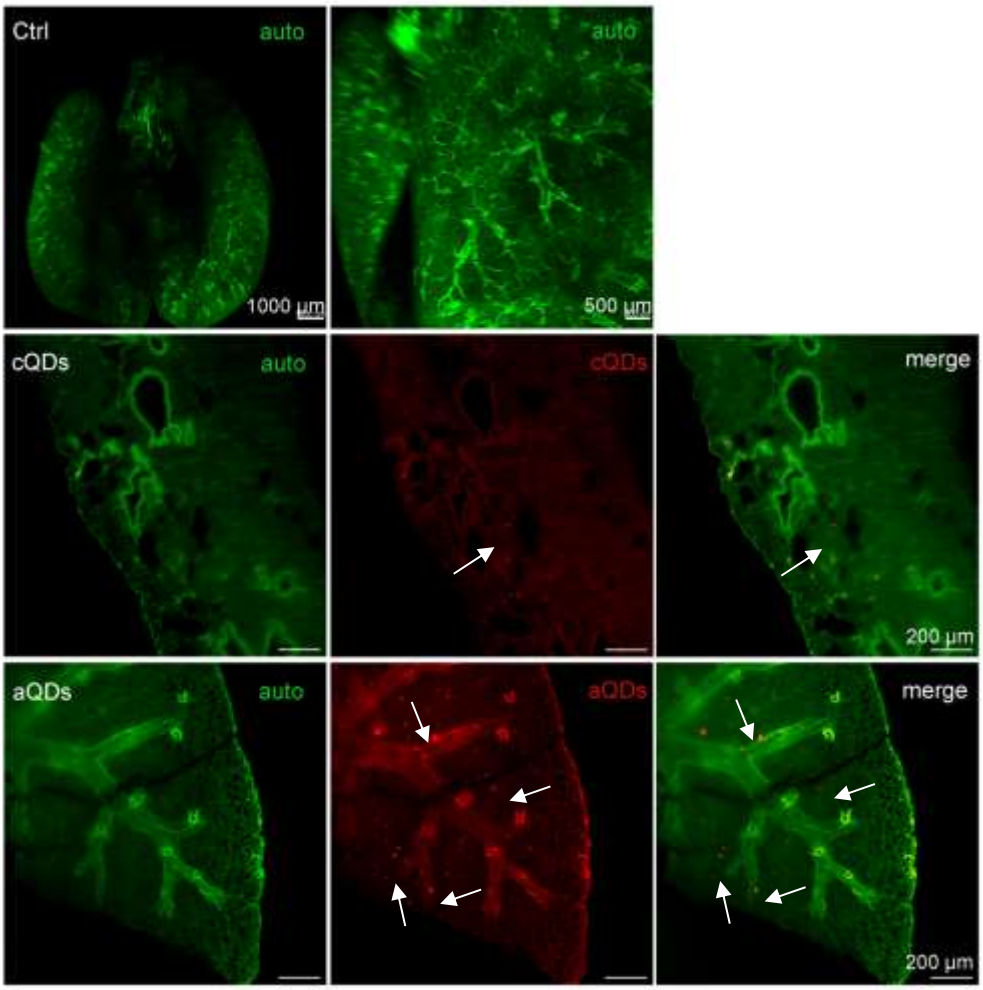

Figure 13. Visualization of QDs distribution in the murine whole lung using 3D imaging.

3D imaging of lungs after tissue optical clearing from a healthy control mouse, cQDs treated, and aQDs treated mouse by i.v. application for 1 h is shown. The images provide an overall presentation of the lung tissue. The lung structure with autofluorescence is depicted in green, while QDs points are highlighted in bright red color (arrow). (Scale bar: 200/500/1000 µm).

In conclusion, the distribution of cQDs and aQDs in whole lungs was different. Both in L-IVM and 3D light sheet microscopy of tissue optical clearing, we observed that cQDs in pulmonary capillaries were more dispersed, leading us to speculate that they were likely taken up by endothelial cells. On the other hand, aQDs were observed to form larger aggregates and remain in the circulation.

3.4 QDs elicited neutrophils immune response in the pulmonary microcirculation

3.4.1 Effects of differently surface modified QDs on neutrophils recruitment

The neutrophils are primary responder cells during the rapid immune reaction (Liew and Kubes 2019). We concentrated on the alterations in neutrophil numbers and migration parameters following the QDs challenge and whether this immune response was different under pathophysiologic conditions, i.e., in LPS and Bleomycin treated mice. For this, neutrophils were immunolabeled with i.v. injected Alexa488-labeled anti-Ly6G antibodies during L-IVM.

As depicted in Fig.14 A, vehicle treatment in healthy mice resulted only in a slight increase in neutrophil numbers, rising from 1.36 ± 0.16/10^4µm^2 at the beginning to 2.37 ± 0.16/10^4µm^2 at 60 min. This small increment in the control group is most likely due to the thoracic surgery. However, neutrophil levels began to increase following i.v. application of aQDs (1 pmol/g) at 20 min and continued to rise until 60 min. During the last 40 min, the neutrophils count increased considerably in the aQDs group compared to the control group, eventually reaching 6.01 ± 0.37/10^4µm^2. Meanwhile, cQDs (1 pmol/g) only elicited a small increase after 60 min (3.46 ± 0.42/10^4µm^2).

Shown in Fig.14 B, as for the LPS-treated mice (24 h) in the absence of QDs, slightly lower neutrophil levels (0.97 ± 0.05/10^4µm^2) than the healthy controls (1.36 ± 0.16/10^4µm^2), have been detected at t=0. Neutrophil numbers increased sharply to 3.55 ± 0.18/10^4µm^2 in the following 60 min, in contrast to healthy control subjects. Furthermore, neutrophil changes in the LPS-treated mice after application of QDs, were approximately the same as in the LPS-treated controls over the course of the experiments. From 30 to 60 min, aQDs injection induced slightly higher neutrophil counts as compared to the LPS and LPS + cQDs groups.

Taken together, 24 h after low dose LPS stimulation, thoracic surgery induced strong neutrophil responses during the course of L-IVM, whereas exposure to QDs had little additional effect.

In fibrotic lungs of Bleomycin-treated mice as well as in Bleomycin-treated mice receiving cQDs (Fig.14 C), the neutrophil numbers at baseline as well as during

the 60 min observation period did not differ from healthy controls. Neutrophil levels increased only after exposure to aQDs, reaching a maximum value of 3.38 ± 0.66/10^4µm^2 after 40 min, before decreasing slightly towards the end.

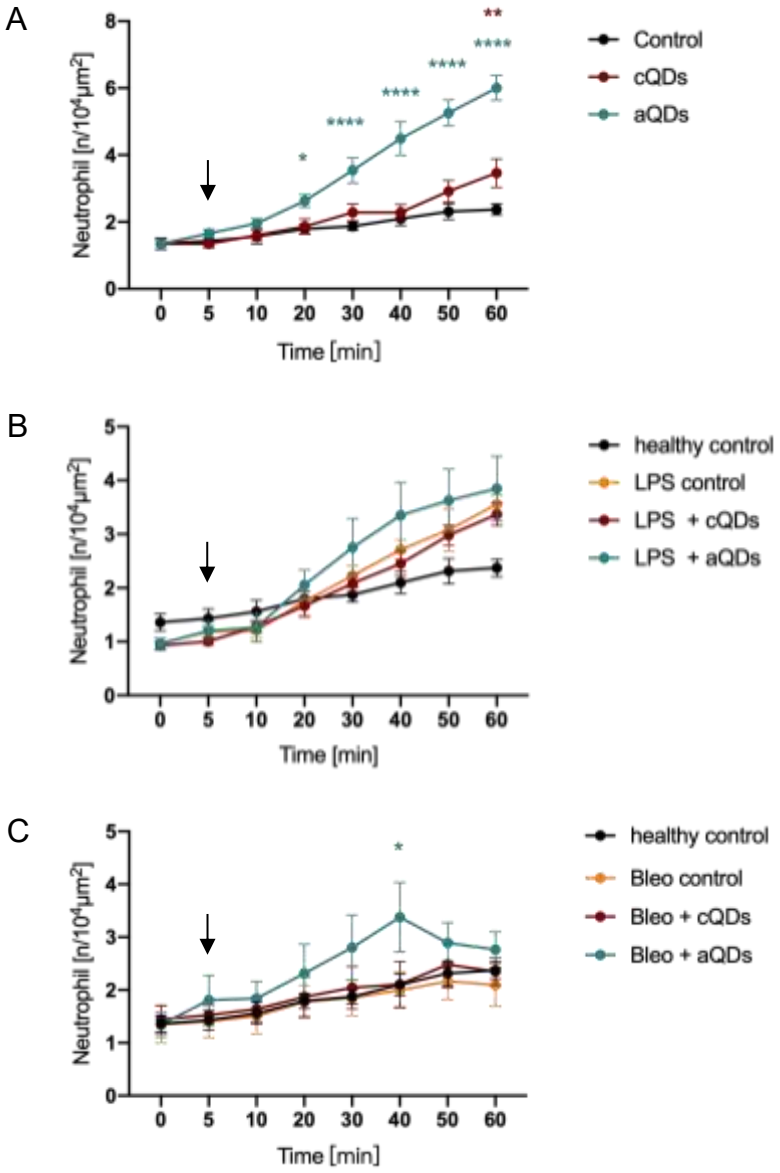

Figure 14. Quantification of the number of recruited neutrophils in the lung microcirculation in 3 different mouse models after application of QDs.

The neutrophil amount was recorded and quantified by L-IVM after QDs (1 pmol/g), or vehicle were applied at 5 min (black arrow). At each time point, five fields of view in the imaging window, on the lung surface were chosen randomly, recorded, and further analyzed. Results of the change in neutrophil count in 3 different mouse models (A: healthy mice, B: LPS-treated mice (24 h), and C: Bleomycin-treated mice (14 d)) during 60 min were quantified

and shown. (mean ± SEM, n = 4 mice/group, green * aQDs vs corresponding control group, red * cQDs vs corresponding control group, Two-way ANOVA test).

3.4.1.1 Distribution of neutrophils in capillaries and alveolar space

Based on the results that aQDs induced neutrophil recruitment in healthy mice, we next studied the primary microvessel types in the pulmonary microcirculation where neutrophils are recruited after aQDs exposure. We utilized merged images of neutrophils labeled with anti-Ly6G (Alexa488) and platelets labeled with anti-GPIb-V-IX complex (DyLight649) by Fiji software, which allowed us to visualize clearly outlined blood vessels. By analyzing these images at two different time points (t=0 and t=60), we aimed to quantify the distribution of neutrophils in the alveolar space and in microvessels of different sizes.

Previous studies have indicated that the diameter of small pulmonary arterioles and venules is approximately 25 μm (Tabuchi et al. 2008), and it has been observed that recruited neutrophils predominantly accumulate in vessels smaller than 10 μm (Yipp et al. 2017). Here we divided the microvessels into three categories: vessels smaller than 10 μm, vessels ranging from 10-20 μm, and vessels larger than 20 μm. In healthy mice, most neutrophils were observed in vessels smaller than 20 μm, as shown in Fig.15 C. After one-hour observation of L-IVM, the level of recruited neutrophils increased significantly compared to the initial time of L-IVM (16.45 ± 1.41 cells/FOV vs. 8.8 ± 0.78 cells/FOV in vessels < 10 μ and 14.70 ± 1.47 cells/FOV vs. 7.60 ± 1.22 cells/FOV in vessels 10-20 μm). The localization pattern of neutrophils in the pulmonary microcirculation following aQDs application was similar to the controls. After 1h aQDs challenge, neutrophils showed a significant increase in vessels smaller than 20 μm, especially in vessels ranging from 10 to 20 μm (35.90 ± 4.08 cells/FOV vs. 11.20 ± 0.84 cells/FOV in vessels < 10 μm and 37.30 ± 4.80 cells/FOV vs. 4.80 ± 0.75 cells/FOV in vessels 10-20 μm). Moreover, neutrophils induced by aQDs for 1 h significantly increased in the alveolar space (Fig.15 B) (10.95 ± 0.88 cells/FOV vs. 3.60 ± 0.32 cells/FOV) and in vessels larger than 20 μm (6.95 ± 2.39 cells/FOV vs. 0.85 ± 0.39 cells/FOV).

The results of our analysis indicate that aQDs induced the recruitment of neutrophils predominately in microvessels smaller than 20 μm in diameter, which are

located directly surrounding the alveoli. These microvessels contributed significantly to this recruitment process. Furthermore, transmigration of neutrophils to the alveolar space had already occurred at this early timepoint.

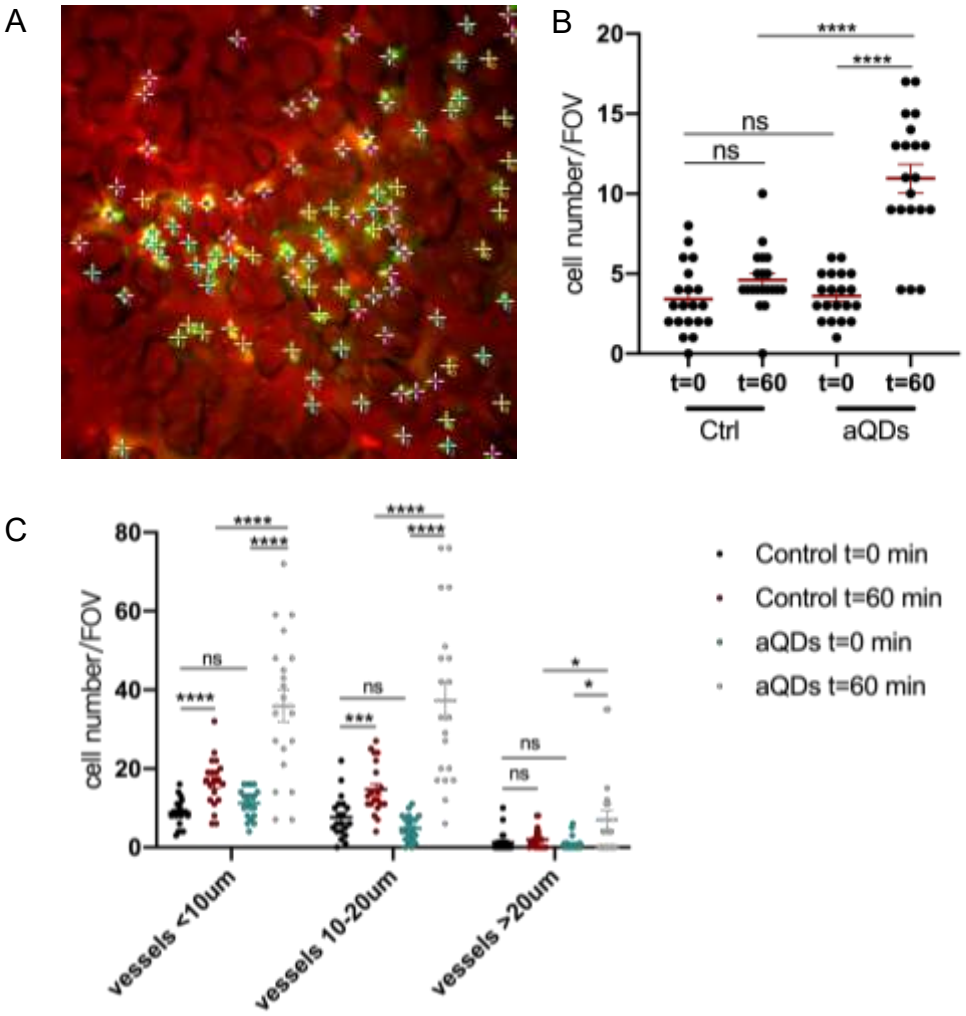

Figure 15. Distribution of neutrophils in the alveolar space and in microvessels of different sizes.

(A) Localization of neutrophils in the alveolar space and in microvessels of different size classes was analyzed using the “Multipoint” function of Fiji. Point 0: neutrophils in the alveolar space, point 1: neutrophils in vessels smaller than 10 µm, point 2: neutrophils in vessels ranging from 10-20 µm, and point 3: neutrophils in vessels larger than 20 µm. Quantitative assessment of neutrophils localized in (B) the pulmonary alveolar space and (C) various-sized microvasculature. (n = 20 areas of observation from 4 mice/group, mean ± SEM, (B) One-way ANOVA test, (C) Student’s t test.)

3.4.1.2 Quantification of neutrophils in lung sections

To further confirm the results obtained by L-IVM, lung samples were collected from mice 1 h after QDs application and subjected to IF staining. Neutrophils were specifically labeled using anti-Ly6G (Alexa488) antibody, and representative images of control, cQDs-treated, and aQDs-treated lungs are shown in Fig. 16 A, B, and C. The images were analyzed using the "Multipoint" function in Fiji software. Following a one-hour exposure to QDs, the number of neutrophils in the aQDs group significantly increased to 395.30 ± 29.18 cells/field of view (FOV) compared to the control group (226.30 ± 7.59 cells/FOV), while the cQDs-treated lungs showed 271.50 ± 33.23 cells/FOV. These findings were consistent with the results obtained from IVM, indicating that aQDs effectively induced the recruitment of neutrophils to the pulmonary microcirculation within 1 h.

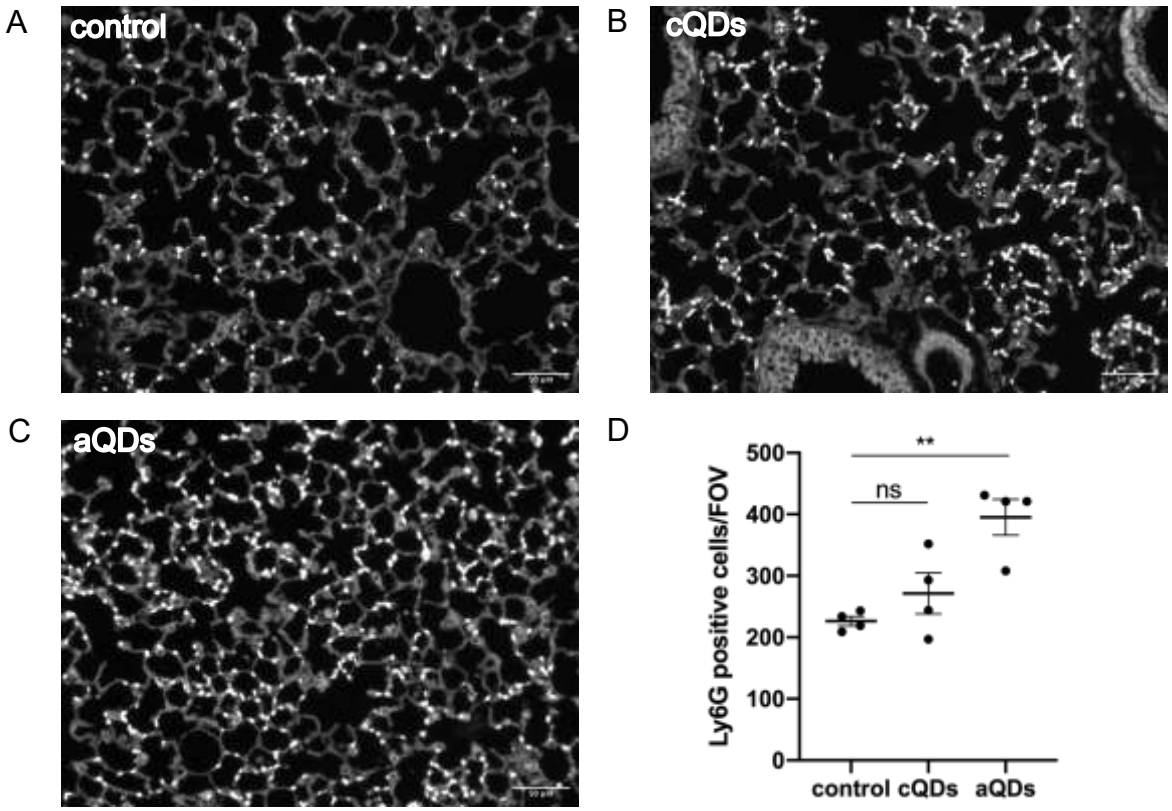

Figure 16. Quantification of neutrophils in lung tissue slices.

Paraffin lung sections (3 µm) obtained from mice after 60 min of QDs application were subjected to staining with Alexa488-labeled anti-Ly6G antibody. Neutrophils in control (A), cQDs-treated (B), and aQDs-treated (C) lungs are depicted white. Quantification of neutrophils is presented in (D). (n = 2 mice/group, mean ± SEM, One-way ANOVA test.)

3.4.2 Effects of QDs on the motility of neutrophils in healthy and LPS-treated mice.

Next, we focused on the motility of neutrophils in healthy mice after aQDs and cQDs i.v. application. Long-term sequences were recorded every 5 seconds at areas of high image quality and stability, which are required for further analysis of neutrophil movement. The lungs of mice after 14 d of Bleomycin treatment were not suitable for long-time L-IVM observation due to diffuse images and strong motion artefacts, which distorted the results of neutrophil motility analysis. Therefor only healthy mice were included in this section. The time-lapse movies were analyzed, and the neutrophil trajectories were automatically generated using “Trackmate” plugin of Fiji, as shown in Fig.17.

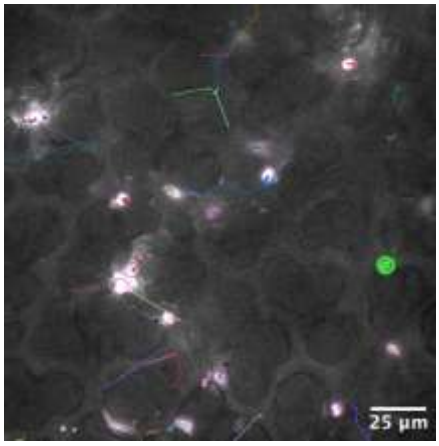

Figure 17. Trajectories of neutrophil movements in healthy mice via L-IVM.

Neutrophil dynamics were recorded every 5 seconds over a period of 10 min by L-IVM. The images were analyzed, and the movement trajectories of neutrophils were automatically generated by plugin “Trackmate” of Fiji software. The figure displays representative neutrophil trajectories during the period of 55-65 min under healthy conditions. Each trajectory is represented by a different color, indicating tracks of individual neutrophils. (Scale bar: 25 µm).

Depending on the state and movement of neutrophils, there are 3 types of neutrophil interactions with vessel walls in the pulmonary microcirculation, involving tethering, adhesion, and crawling. Tethering neutrophils were defined as those interacting with the endothelium for less than 30 s. Adhering neutrophils were defined as those interacting with the endothelial layer for longer than 30 s without

any movement. Crawling neutrophils were defined as those exhibiting movements for longer than 30 s (Yipp et al. 2017). Fig.18 depicts the distribution and dynamic changes of neutrophil-vessel interactions in healthy mice following QDs application. The results demonstrate that, regardless of whether there was an additional challenge or not, the population of tethering and crawling neutrophils had a trend of increasing after 1 h. In contrast, the number of adherent neutrophils remained relatively stable throughout the observation period, with only a slight increase observed in response to aQDs.

These results shed light on the dynamic behavior of neutrophils in response to QDs exposure, with tethering and crawling neutrophils being more actively involved in the recruitment process. The stable levels of adherent neutrophils suggest that their adhesion to the endothelium is maintained and might be unaffected by the presence of QDs. Due to the challenging surgery and analysis, the sample size is limited (only two mice per group). Therefore, the conclusions drawn from this section may not be as robust as desired.

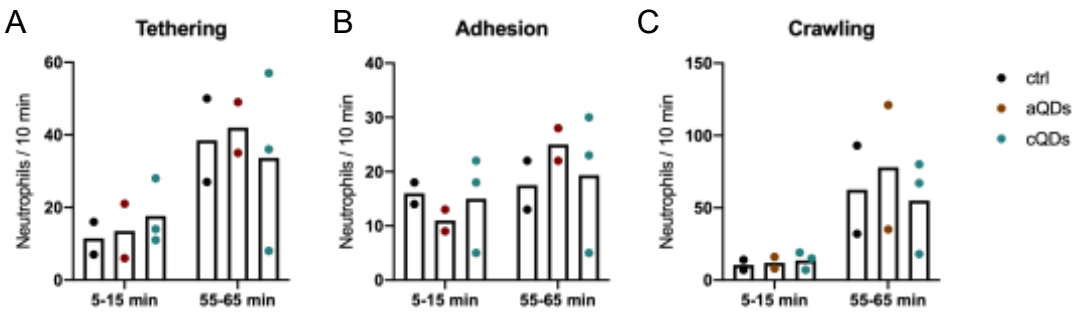

Figure 18. Quantification of neutrophil interaction patterns in the pulmonary microcirculation.

Neutrophil recruitment steps, namely tethering (A), adhesion (B), and crawling (C) were quantified in healthy mice after QDs exposure (in the time periods of 5-15 and 55-65 min) by the “Trackmate” plugin of Fiji. Tethering neutrophils were defined as those interacting with blood vessel walls for less than 30 s. Adherent neutrophils were defined as those interacting for longer than 30 s without displaying any movement. Crawling neutrophils were defined as those exhibiting movements for longer than 30 s (Yipp et al. 2017). (Mean value, n = 2 mice/group).

The crawling velocity of neutrophils in healthy mice was analyzed after categorizing them based on their microvessel interaction types. All crawling neutrophils

within an observation area were included in the analysis, and their crawling velocities were measured in two 10-min intervals (5-15 and 55-65 min). Fig.19 presents the crawling velocity of neutrophils under healthy conditions. Initially, without any treatment, the crawling velocity of neutrophils was measured at 10.55 ± 1.58 μm/min. At 5 min, QDs (both aQDs and cQDs) were intravenously administered. Immediately afterwards, the crawling velocity of neutrophils in the aQDs group was measured to be 8.23 ± 1.05 μm/min, while in the cQDs group, it was 8.63 ± 0.89 μm/min. After 1 h, the crawling velocity of neutrophils in the control group was increased, rising from 10.55 ± 1.58 μm/min to 16.60 ± 1.52 μm/min. Similarly, in the cQDs group, the crawling velocity significantly increased to 15.57 ± 1.55 μm/min after 1 h. However, after 1 h, the crawling velocity of neutrophils in the aQDs group was 8.45 ± 0.37 μm/min, which was significantly lower than that in the control and cQDs groups at the same time point.

These findings suggest that aQDs application can slow down the crawling velocity of recruited neutrophils in response to this challenge. Considering the previous observations that aQDs induced neutrophil recruitment in the pulmonary microcirculation, this decreased crawling velocity indicates a potential regulatory effect of aQDs on the motility of recruited neutrophils in the pulmonary microvasculature, possibly by the induction of specific adhesion molecules (see below).

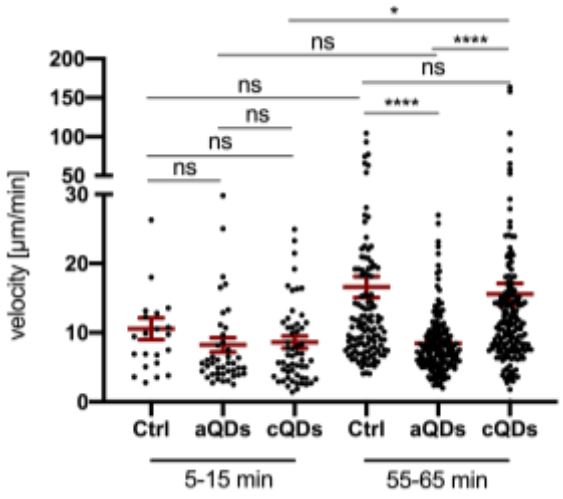

Figure 19. Crawling velocity of neutrophils in healthy mice after QDs treatment.

Crawling neutrophils in time lapse movies of 10 min at the indicated timepoints, were auto tracked by Fiji and the velocities were analyzed. Velocities of different conditions and times are shown. (mean ± SEM, n = 22-174 neutrophils in 10 min form 2-3 mice/group, Student's t-test/One-way ANOVA test).

3.4.3 Effect of QDs application on blood perfusion velocity

At the end of the experiments after 1 h of L-IVM recording, fluorescent melamine resin particles microbeads (diameter: 0.94 ± 0.05 µm) were injected intravenously to measure the blood perfusion velocity. As shown in Fig.20, A, the microbeads can be seen as bright dots, some of which adhere to blood vessels and some of which flow freely with the blood stream. The centerline blood perfusion velocity was obtained by manually tracking free flowing beads using the “Manual tracking” plugin of Fiji.

In the healthy state as shown in Fig.20 B, blood perfusion velocity after 1 h of the L-IVM procedure was 201.6 ± 10 µm/s. After 1 h of exposure to aQDs, blood perfusion velocity was significantly reduced to 149.2 ± 8.24 µm/s. Meanwhile, cQDs injection resulted in a slightly lower perfusion velocity of 177 ± 8.5 µm/s. Compared to healthy controls, the blood perfusion in LPS-treated mice was decreased considerably to 119.8 ± 6.43 µm/s (Fig.20 D). In contrast, as shown in Fig.20 C, administration of cQDs or aQDs did not further alter blood perfusion in LPS-treated mice, with a velocity of 138.5 ± 7.87 µm/s in the cQDs group and 139.8 ± 8.53 µm/s in the aQDs group.

A

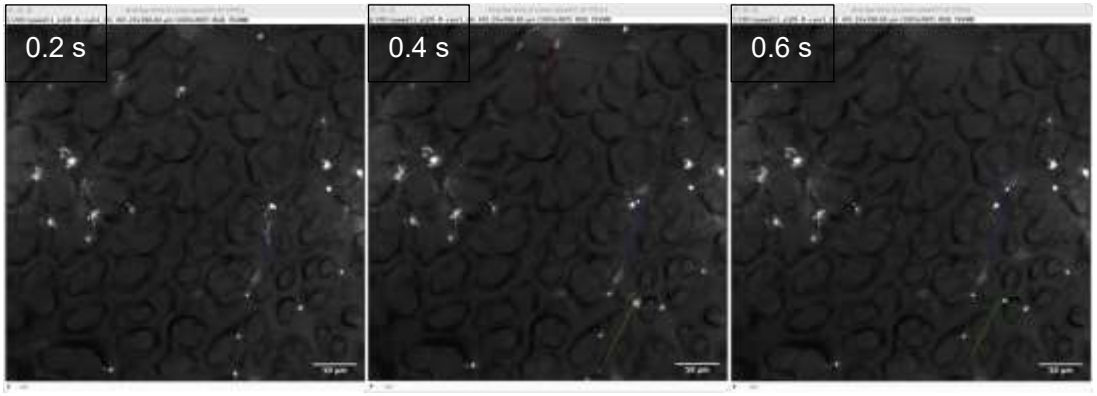

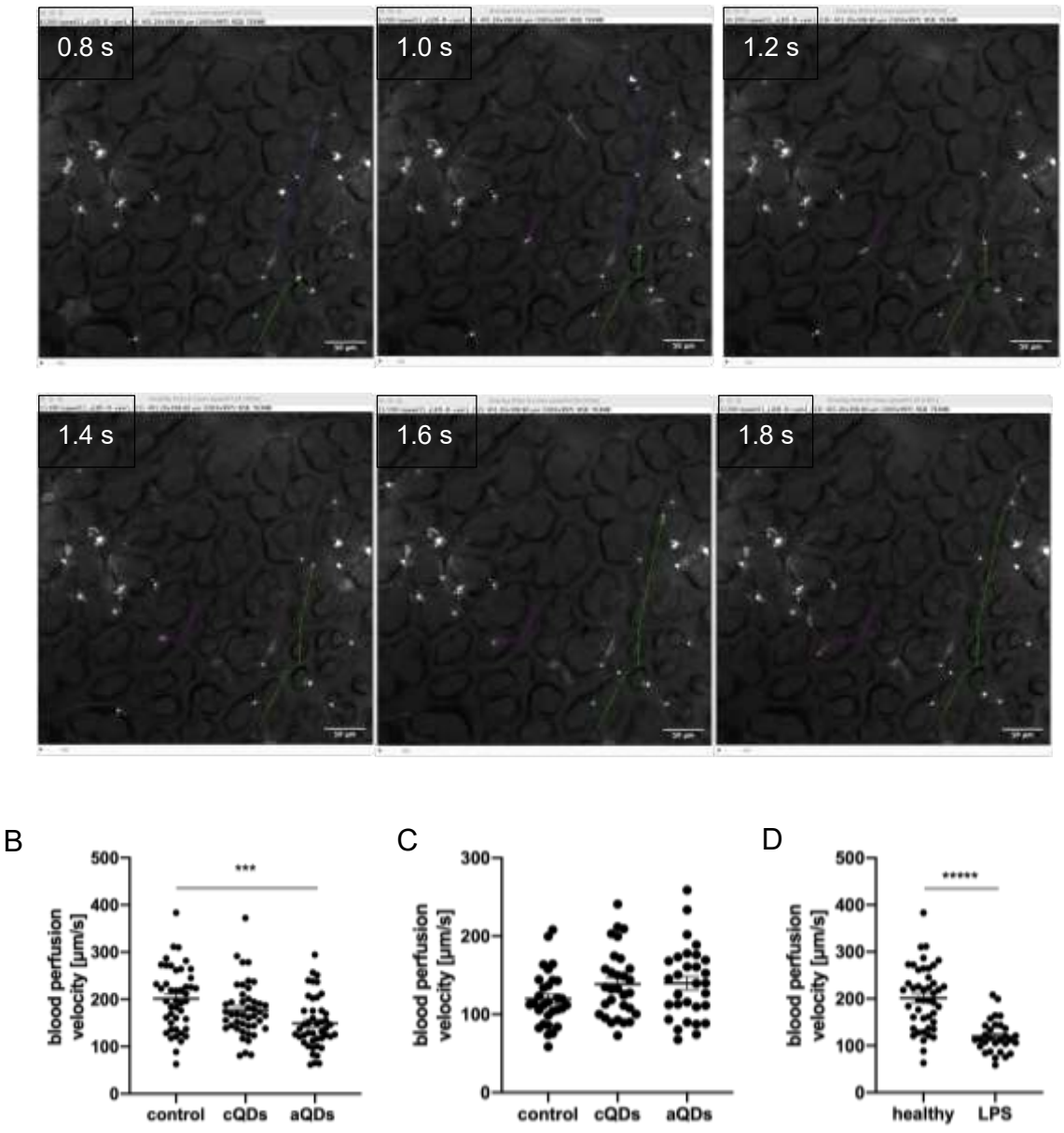

Figure 20. Quantification of blood perfusion velocity.

(A) Time lapse images of blood perfusion depicted by bead trajectories in the lung microcirculation. The sequential images show blood flow direction in blood vessels presented by individual microbead trajectories, depicted as different colored lines. Blood perfusion velocities in healthy (B) and LPS-pretreated mice (C) after 1h of QDs administration are shown. (mean ± SEM, n = 2~3 mice/group, One-way ANOVA test.). (D) Blood perfusion velocity of healthy and LPS-treated conditions after 1 h L-IVM are presented. (mean ± SEM, n = 2~3 mice/group, Student's t-test).

3.5 Neutrophil recruitment induced by aQDs: Involvement of cellular degranulation and cell adhesion molecules

To further understand the mechanisms underlying the immune responses induced by aQDs, we performed experiments to inhibit or block various factors or molecules that could potentially be involved in cytokine release and neutrophil recruitment.

3.5.1 Inhibition of neutrophil recruitment induced by aQDs by cromolyn

As previously demonstrated, QDs-induced leukocyte recruitment in skeletal muscle postcapillary venules could be reduced by prior application of cromolyn, an inhibitor of cellular degranulation (Rehberg et al., 2010). The inhibitor is described to act primarily on mast cells but also on (alveolar) macrophages (Holian, Hamilton, and Scheule 1991), which are both well known to release a range of mediators to induce the inflammatory process. Therefore, we investigated whether cromolyn also inhibited inflammatory response by aQDs in the pulmonary immune system. A dose of 0.2 mg/kg (BW) of cromolyn was administrated intravenously to healthy mice 30 min prior to L-IVM experiments. In the cromolyn pretreated group receiving aQDs, different neutrophil responses were observed compared to the group treated only with aQDs. The starting level of neutrophils was similar like the control baseline values. Thereafter, neutrophil numbers were only slightly higher than the control group. At 60 min, pretreatment with cromolyn largely abolished the neutrophil recruitment induced by aQDs (3.04 ± 0.62/10^4µm^2 in cromolyn + aQDs vs. 6.01 ± 0.37/10^4µm^2 for aQDs only) (Fig.21). Taken together, the inflammation induced by aQDs could be blocked by cromolyn pretreatment.

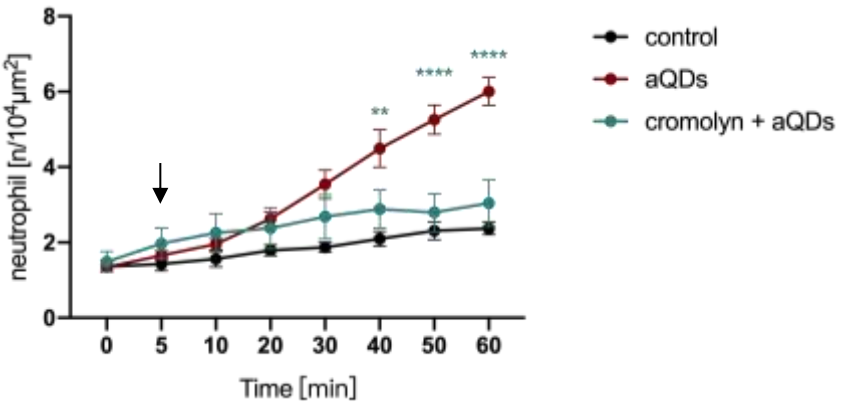

Figure 21. Inhibition of cellular degranulation decreased numbers of recruited neutrophils induced by aQDs application.

Neutrophil recruitment over time in the lung microcirculation was quantified by L-IVM. Cromolyn, an inhibitor of mast cell and macrophage degranulation, was applied intravenously at 0.2 mg/kg (BW) 30 min prior to L-IVM. QDs or vehicle were injected at 5 min (black arrow). (mean ± SEM, n = 4 mice/group, green * cromolyn + aQDs vs aQDs group, Two-way ANOVA test).

3.5.1.1 Staining of mast cells in lung tissue

Since membrane stabilizing cromolyn inhibited the neutrophil recruitment induced by aQDs and mast cell degranulation has been shown to contribute to early neutrophil recruitment (De Filippo et al. 2013), we investigated whether localized mast cells in the alveolar region, i.e. in the region where the IVM analysis has been conducted, could be responsible for this effect. Previous studies have demonstrated that there are a few mast cells present in the lung parenchymal tissues of laboratory wildtype mice (Yeh et al. 2021). However, in some pathological conditions such as allergic pulmonary inflammation, lung ischemia-reperfusion, and influenza infection, there is an increase in the number of mast cells in the lung parenchyma (Greenland et al. 2014; Bankova et al. 2015; Zarnegar et al. 2018). The lungs were collected and stained with Toluidine Blue as shown in Fig.22. In control mice and QDs-treated mice for 1 h, we did not observe any significant staining of mast cells in the alveolar region or around bronchioles. However, after 4 h of LPS treatment and 24 h of QDs treatment, we observed the presence of a few cells located near the bronchioles with violet-colored granules stained with Toluidine Blue, which is indicative of mast cells.

These findings make the contribution of alveolar-localized mast cells to the on-site initiation of neutrophil recruitment immediately after QDs application implausible. However, it is possible that mast cells in other tissues could be involved in the observed effects. Interestingly, QDs (24 h) as well as LPS (4 h) application seems to either increase mast cell numbers or increase mast cell granularity stained by Toluidine Blue in the lung parenchyma.

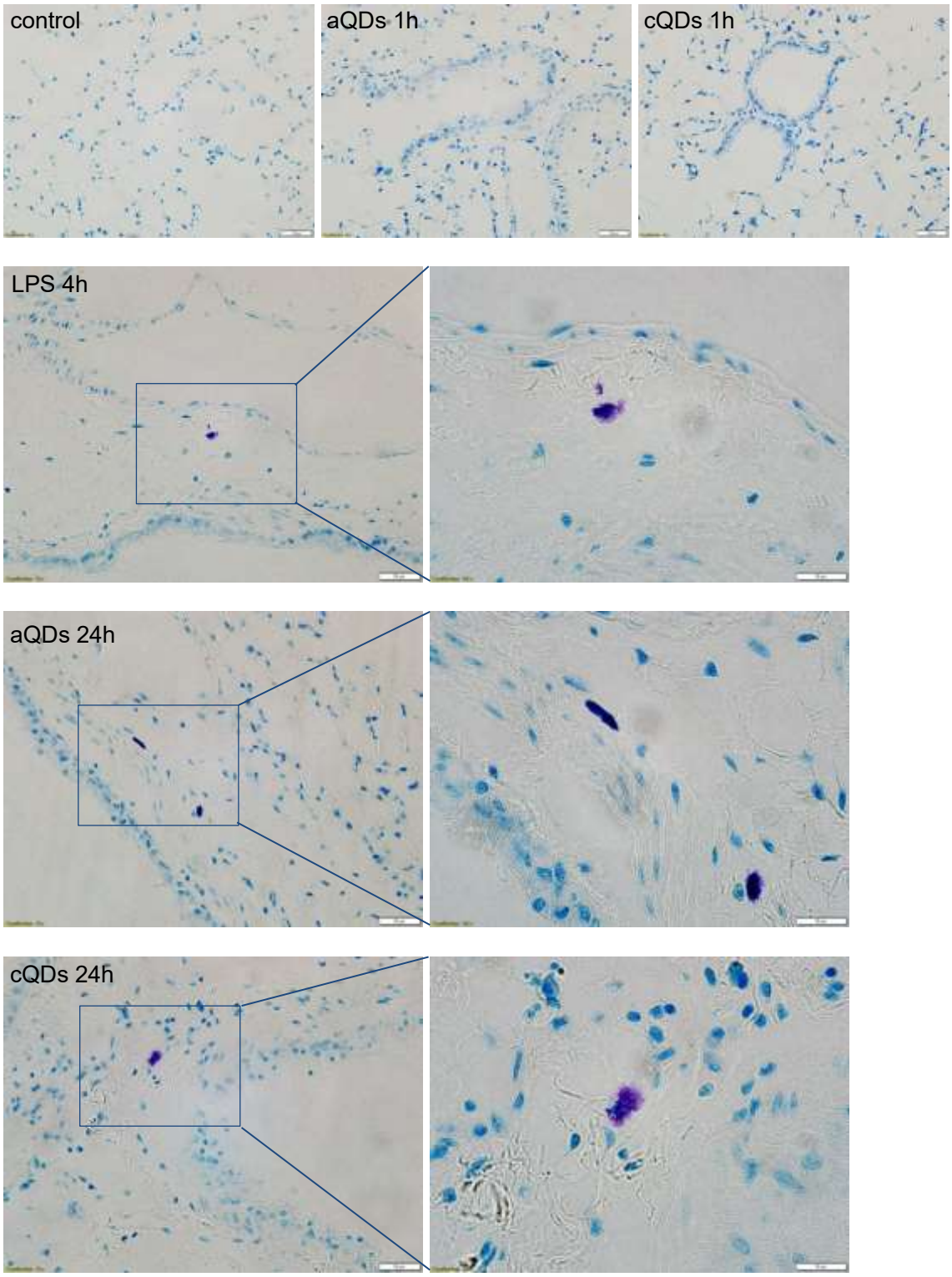

Figure 22. Toluidine blue stained lung sections of mice following different treatments.

Representative images depict the staining of metachromatic granules in mast cells, which exhibit a violet color, against the blue background of the surrounding tissue in histological lung sections obtained after aQDs and cQDs exposure for 1 h and 24 h, LPS treatment for 4 h, and under control conditions. (Scale bar: 10/20 µm).

3.5.2 Suppression of neutrophil recruitment by TNF-α neutralization after aQDs application

Mast cells and macrophages play a role in vivo neutrophil recruitment through the release of stored cytokines, especially TNF-α early in the inflammatory response induced by immune complexes (Zhang, Ramos, and Jakschik 1992; De Filippo et al. 2013; Dudeck et al. 2021). Additional TNF-α promotes the accumulation of neutrophils (Peterson et al. 2006). To elucidate whether the process of neutrophil recruitment triggered by aQDs was influenced by TNF-α, neutralizing anti-TNF-α monoclonal antibodies (mAbs) were intravenously injected into the mice 30 min before L-IVM and aQDs injection. The application of anti-TNF-α mAbs significantly decreased the basal levels (t=0 min) of neutrophils during L-IVM, with a value of 0.85 ± 0.13/10^4μm^2 compared to 1.36 ± 0.16/10^4μm^2 in the control group, as shown in Fig.23 B. After the application of aQDs (Fig.23 A), neutrophils levels did not increase as in the aQDs-only application group but remained consistently below control neutrophil numbers. Taken together, anti-TNF-α mAbs induced a significant reduction, with a neutrophil value of 1.83 ± 0.13/10^4μm^2 after 60 min.

Interestingly, the application of aQDs along with IgG1 isotype control antibodies also showed an inhibitory effect on neutrophil recruitment induced by aQDs, although the effect was not as strong as that of the neutralizing anti-TNF-α mAbs. Previous studies have demonstrated that IgG isotype can decrease the levels of pro-inflammatory cytokines such as IL-1β and IL-6, which are associated with neutrophil recruitment (Nguyen et al. 2012). IgG1 is the most abundant isotype of IgG in the blood of mice and has been shown to possess anti-inflammatory properties by blocking the C5a pathway (Karsten et al. 2012). This could possibly explain why the IgG1 isotype exhibited anti-inflammatory effects in our study.

One hour after L-IVM, blood perfusion rates were quantified by tracking melamine resin microbeads. Pretreatment with anti-TNF-α mAbs in mice exposed to aQDs restored the reduced blood perfusion velocity caused by aQDs to a value of 247.5 ± 11.09 μm/s, which was significantly higher than the blood perfusion rate in the control state (Fig.23 C).

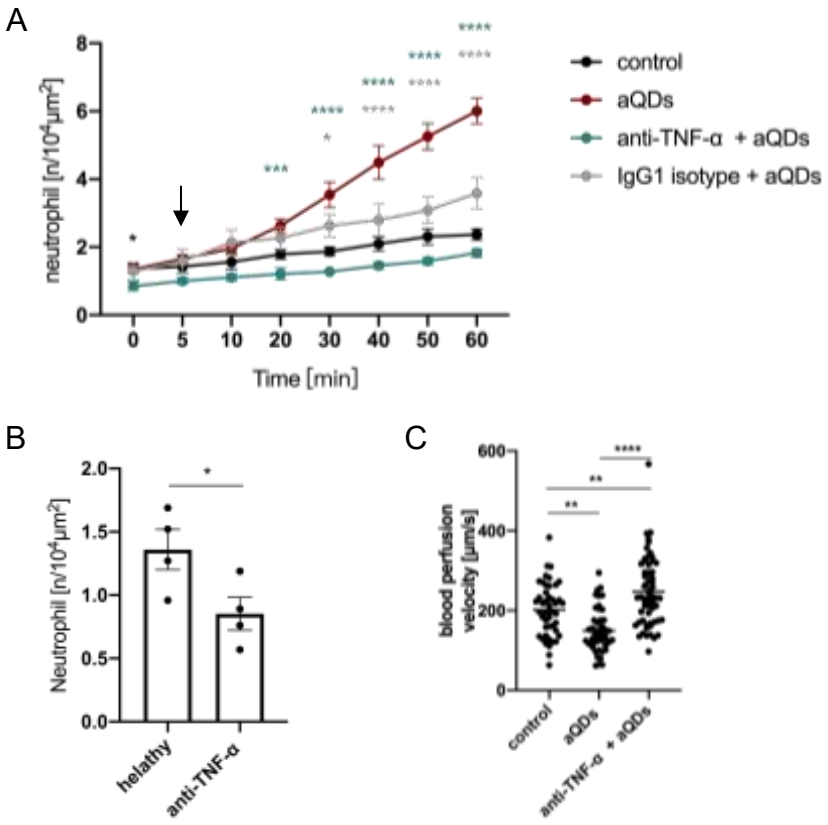

Figure 23. Application of neutralizing anti-TNF-α mAbs suppressed neutrophil recruitment and increased the blood perfusion velocity decline induced by aQDs.

(A) Quantification of recruited neutrophils over time in mice pre-treated intravenously with anti-TNF-α mAbs for 30 min prior to L-IVM. (n = 4 mice/group, mean ± SEM. Grey * anti-IgG1 mAbs + aQDs vs aQDs group, green * anti-TNF-α mAbs + aQDs vs aQDs group, Two-way ANOVA test. Black * anti-TNF-α mAbs + aQDs vs control group, Student's t test). (B) Comparison of baseline neutrophils levels with and without anti-TNF-α mAbs 30 min pre-treatment. (n = 4 mice/group, mean ± SEM, Student's t-test). (C) Quantification of blood perfusion velocity in different experimental groups. (n = 3~4 mice/group, mean ± SEM, One-way ANOVA test).

3.5.3 E-selectin as a mediator of neutrophil recruitment induced by aQDs

Neutrophil recruitment involves a complex cascade of selectin and integrin responses between endothelial cells and neutrophils (Ley et al. 2007; Kim and Luster 2015). Unlike in skin and skeletal muscle, the mechanisms of neutrophil recruitment in the pulmonary microcirculation are not fully understood yet. Because the diameter of pulmonary capillaries ranges from approximately 2 to 14 µm, neutrophils do not roll but undergo mechanical deformation to process in the

capillaries (Doerschuk et al. 1993). The role of selectins and integrins in neutrophil recruitment in the lung can vary depending on various stimuli (Rossaint and Zarbock 2013; Maas, Soehnlein, and Viola 2018). For instance, intratracheal administration of LPS from *Streptococcal pneumonia* induces neutrophil recruitment independently of E- or P-selectin, whereas LPS from *Escherichia coli* causes E- and L-selectin-dependent neutrophil recruitment (Mizgerd et al. 1996; Kornerup et al. 2010). To further understand the role of selectins in neutrophil recruitment induced by aQDs in the pulmonary microcirculation, we administered specific neutralizing Abs targeting E-selectin, L-selectin, and P-selectin intravenously 30 min prior to L-IVM and injection of aQDs.

As depicted in Fig.24 A, the application of anti-E-selectin mAbs along with aQDs resulted in an initial neutrophil value of 0.99 ± 0.15/10^4µm^2, which remained relatively stable over 1h (at 60 min: 1.95 ± 0.40/10^4µm^2), similar to the neutrophil numbers in the control group, indicating that aQDs induced neutrophil recruitment was abrogated by anti- E-selectin mAbs. However, in mice pretreated with anti-P-selectin mAbs before the application of aQDs (Fig.24 B), the recruited neutrophil numbers remained like those in the aQDs-only application group, with only a slight reduction during the last 30 min, that was not significantly different. Regarding L-selectin function, no definitive conclusion could be drawn, as in 3 of 5 mice pretreated with anti-L-selectin mAbs for 30 min, there were already a significant number of neutrophils accumulated in the lung microcirculation at t=0 (Fig.24 C). For the other 2 mice, there were no apparent alterations in neutrophil recruitment induced by aQDs compared to the aQDs-only treated group.

A

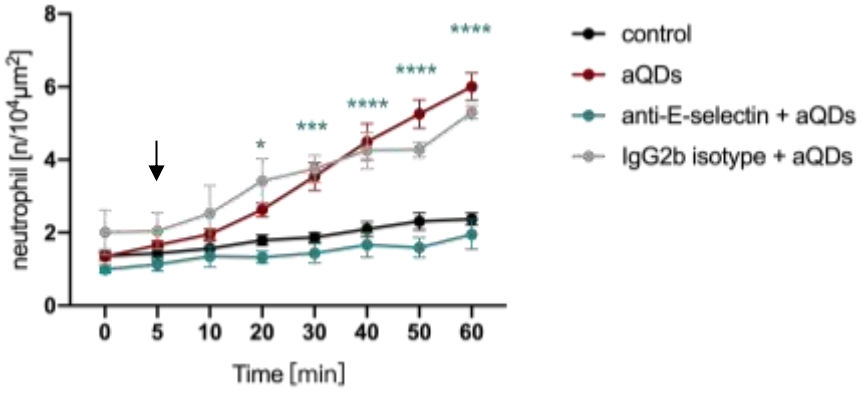

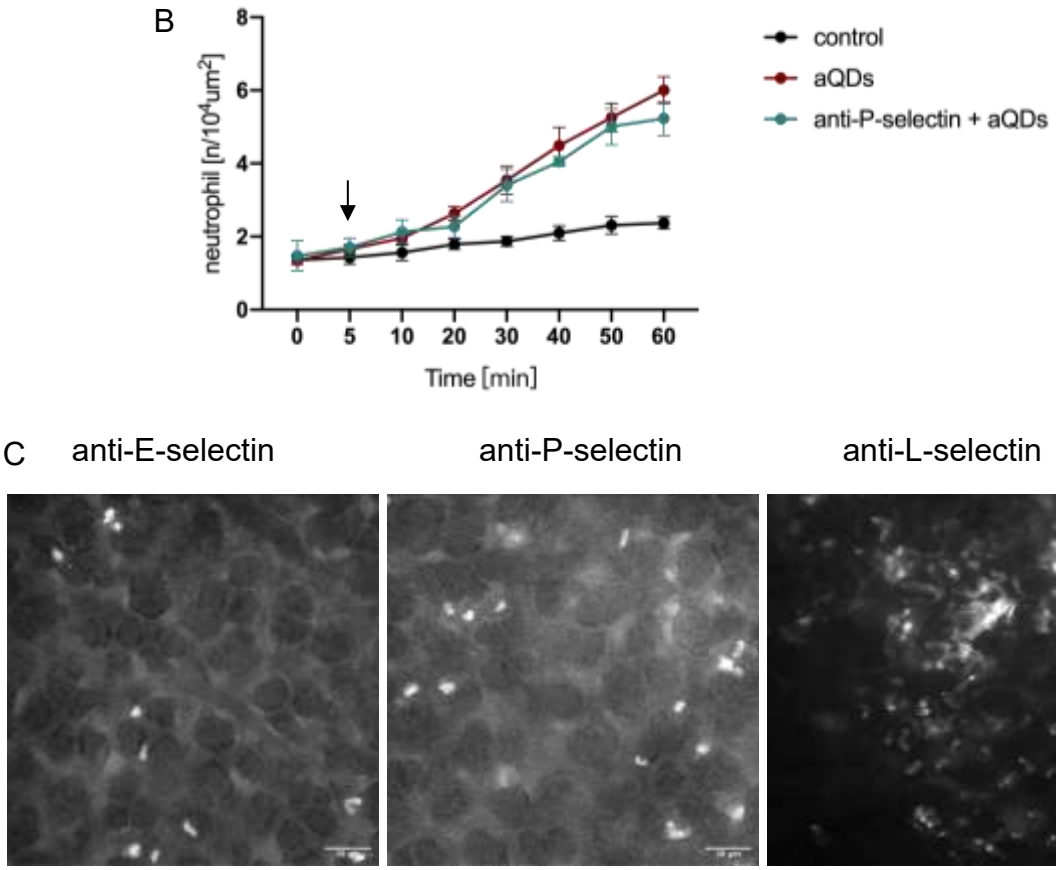

Figure 24. Application of anti-E-selectin but not anti-P-selectin or anti-L-selectin neutralizing mAbs reduced neutrophil recruitment elicited by aQDs.

Quantification of recruited neutrophil numbers over time in mice pretreated intravenously with (A) anti-E-selectin or (B) anti-P-selectin mAbs for 30 min followed by application of aQDs. (Black arrow indicates aQDs injection at t = 5 min; mean ± SEM, n = 4 mice/group, green * anti-E-selectin mAbs + aQDs vs aQDs group, Two-way ANOVA test). (C) Representative L-IVM images obtained at t=0 min of mice pre-treated intravenously with anti-E-selectin, P-selectin, and L-selectin mAbs for 30 min. (Scale bar: 50µm).

3.5.3.1 IF staining of E-selectin on lung paraffin sections

To investigate whether the application of QDs in the pulmonary microcirculation induces the expression of E-selectin on the endothelial cell surface, lung sections were collected and subjected to IF staining using the CD62E antibody (UZ6 (ab2497), Abcam, Cambridge, UK). The pulmonary endothelium was labeled with the Prx antibody (HPA001868, Sigma-Aldrich, Merck KGaA, Germany). The images of the stained sections under different conditions are presented in Fig.25 A-

D. Quantitative analysis revealed a significant increase in CD62E-positive microvessel segments after the application of aQDs compared to the control group (21 ± 1.62/FOV vs. 3.33 ± 0.84/FOV). Additionally, there was also an increase in CD62E-positive microvessel segments in the cQDs group (9.33 ± 0.67/FOV). These findings suggest that aQDs induce the upregulation of CD62E expression on pulmonary endothelial cells, indicating the involvement of E-selectin in neutrophil recruitment in the pulmonary microcirculation.

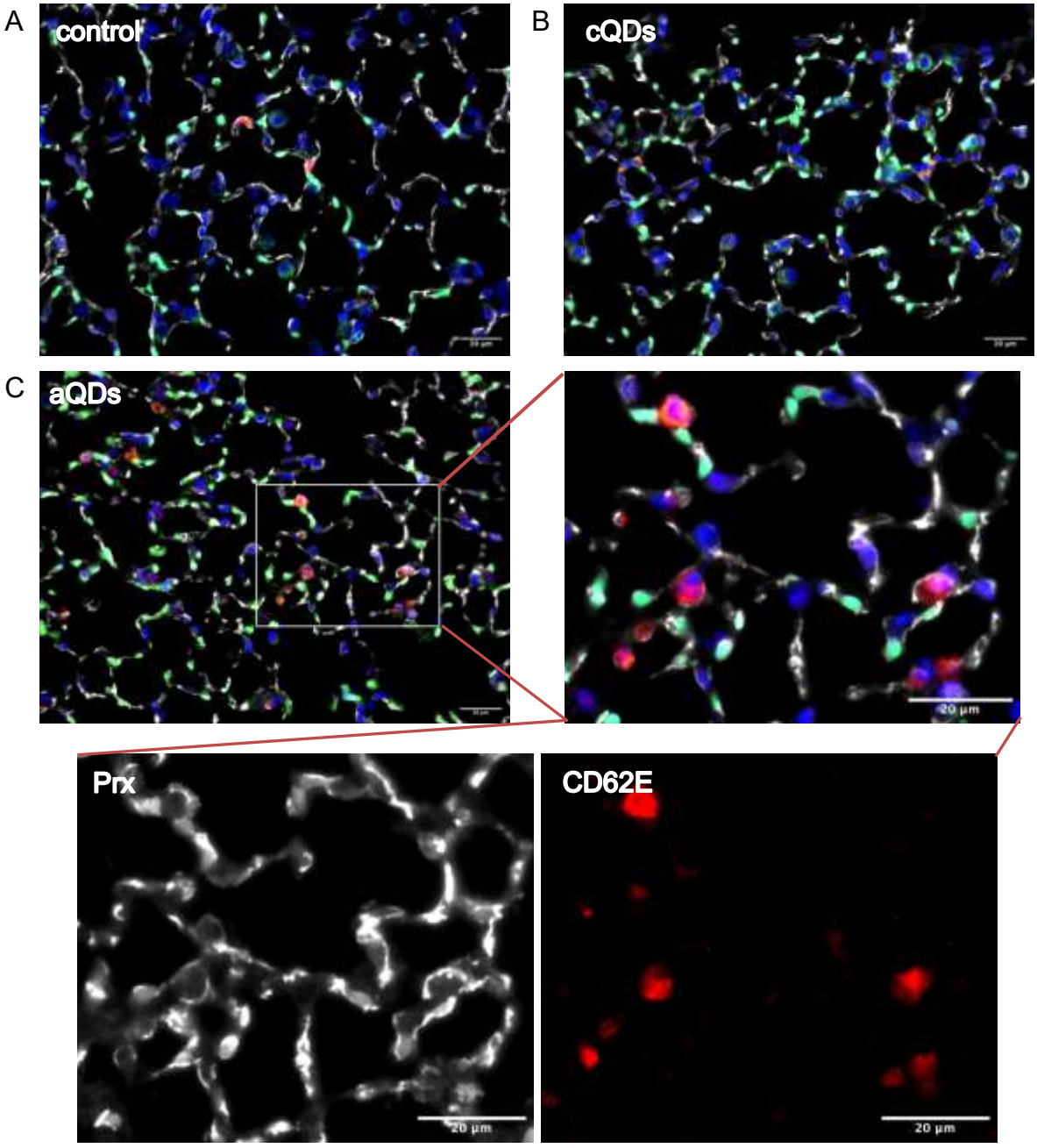

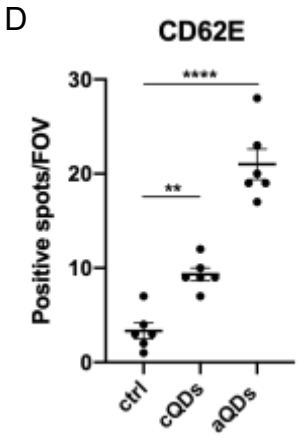

Figure 25. Quantification of CD62E on lung slices by IF staining.

Paraffin lung sections (3 µm) obtained from the control (A), cQDs-treated (B), and aQDs-treated (with the enlarged image) (C) mice after 1h were stained with Rat Anti-CD62E antibody (red), Alexa488-labeled anti-Ly6G antibody (green), Rabbit Anti-Prx antibody (white) and DAPI (blue). (Scale bar: 20 µm). The images were analyzed to quantify the number of CD62E positive spots, as shown in (D). (n = 3 mice/group, mean ± SEM, One-way ANOVA test.)

3.5.4 LFA-1 but not MAC-1, mainly mediated the aQDs induced neutrophil recruitment

LFA-1 and Mac-1, expressed on leukocytes, are key integrins that regulate leukocyte adhesion and migration in the inflammatory response. LFA-1 plays a predominant role in mediating PMN adhesion to ICAM-1 and ICAM-2, whereas Mac-1 is primarily responsible to RAGE, JAM-A, and JAM-C. (Ley et al. 2007; Kolaczkowska and Kubes 2013; Li et al. 2018). The role of LFA-1 and MAC-1 in neutrophil recruitment in the pulmonary microcirculation was addressed. Mice were pre-treated intravenously with anti-LFA-1 or anti-MAC-1 neutralizing mAbs 30 min prior to L-IVM, thereafter QDs were applied intravenously at t=5 min. The application of anti-LFA-1 mAbs along with aQDs resulted in neutrophil counts similar to the control baseline (Fig.26 A), with a value of 1.31 ± 0.10/10^4um^2 (at 0 min) and an increase to 2.21 ± 0.19/10^4um^2 (at 60 min). Notably, neutrophil recruitment induced by aQDs was effectively inhibited by the anti-LFA-1 mAbs. Furthermore, the blood perfusion velocities in the different mAb treatment groups after 1h of L-IVM were analyzed (Fig.26 C). When compared to controls (201.6 ±

10 um/s), anti-LFA-1 mAbs significantly recovered the reduced blood perfusion speed after aQDs injection from 149.2 ± 8.23 um/s to 185.7 ± 9.79 um/s.

These findings suggest that LFA-1 plays a critical role in the process of neutrophil recruitment induced by aQDs. Inhibition of LFA-1 effectively suppressed neutrophil recruitment, and this was accompanied by an improvement in blood perfusion velocity. These results indicate that LFA-1 is possibly involved in the adhesion step of neutrophil recruitment in response to aQDs in the pulmonary microcirculation. The restoration of blood perfusion velocity after anti-LFA-1 mAbs treatment suggests that blocking LFA-1 mitigates the impact of aQDs on the pulmonary microcirculation.

In Fig.26 B, the administration of anti-MAC-1 mAbs appeared to have a dynamic effect on neutrophil recruitment induced by aQDs. Initially, the pretreatment with anti-MAC-1 mAbs decreased the number of recruited neutrophils. However, the neutrophil numbers at 60 min increased again ($5.43 \pm 0.74/10^4 um^2$) in the anti-MAC-1 mAbs + aQDs group and became approximately equal to the neutrophil numbers obtained after only aQDs administration ($6.01 \pm 0.37/10^4 um^2$), indicating that anti-MAC-1 slow down the neutrophil recruitment. This suggests that while MAC-1 may play a role in the initial recruitment of neutrophils in response to aQDs, other factors or compensatory mechanisms might come into play after 1 h, leading to the recovery of neutrophil recruitment even in the presence of anti-MAC-1 mAbs.

Following our investigation of LFA-1 and MAC-1 functions in the neutrophil recruitment cascade, we aimed to study the role of ICAM-1, an important endothelial adhesion molecule and ligand of LFA-1. However, during the experiment, we encountered unexpected challenges. The administration of anti-ICAM-1 mAbs to 5 mice for 30 minutes resulted in adverse effects, including inflammation detected by L-IVM or even death of the mice at the start of L-IVM, for reasons that are currently unknown. As a result, we were unable to proceed with the investigation of ICAM-1 in this study, and this issue requires further investigation to better understand the underlying mechanisms and potential complications associated with anti-ICAM-1 mAbs treatment.

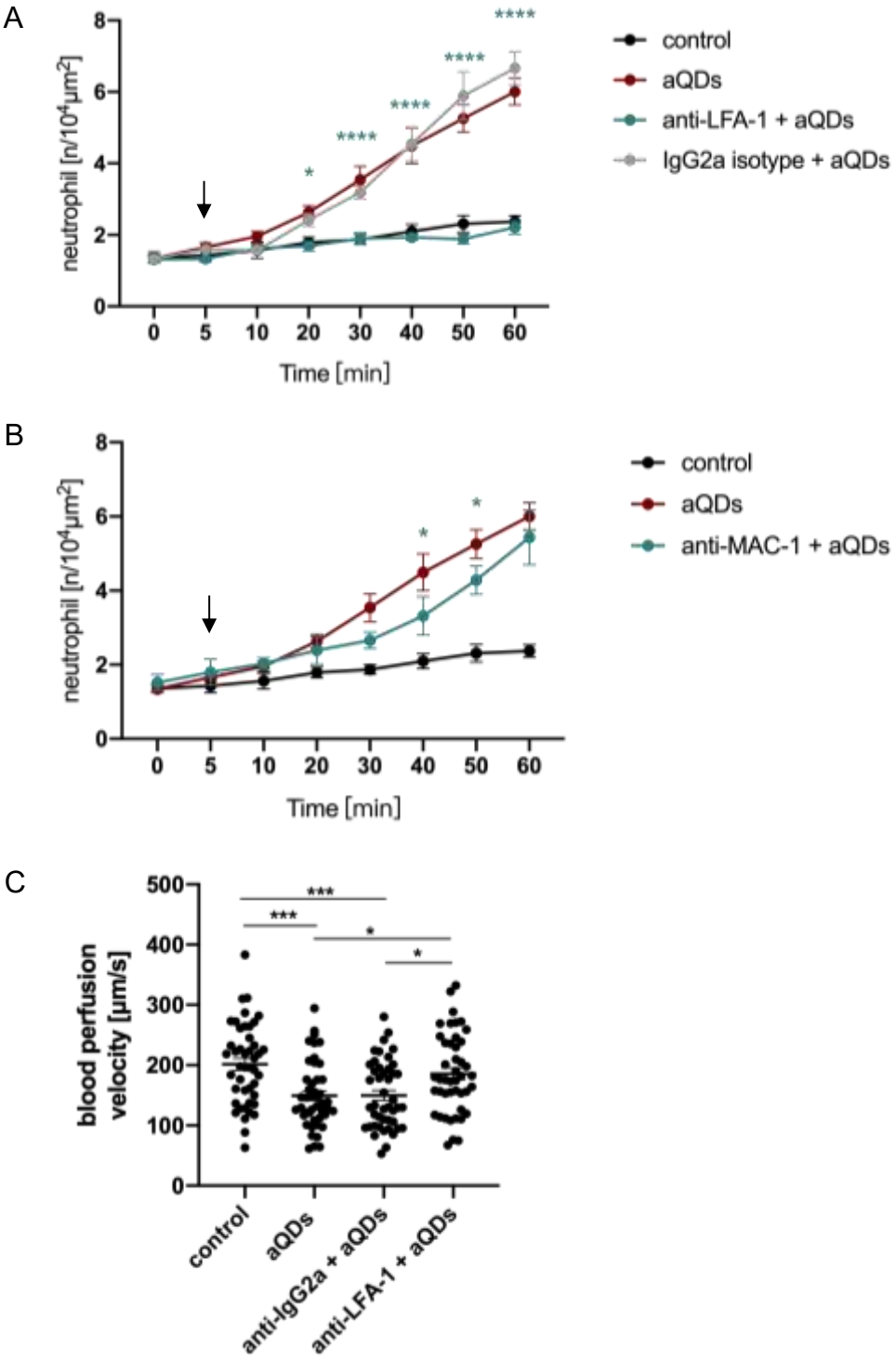

Figure 26. Inhibition of LFA-1 but not MAC-1 reduced neutrophil recruitment elicited by aQDs.

Quantification of recruited neutrophil numbers over time in mice pre-treated intravenously with (A) anti-LFA-1 mAbs or (B) anti-MAC-1 mAbs or isotype control Abs 30 min prior to L-IVM and aQDs exposure at 5 min (black arrow). (mean ± SEM, n = 3~4 mice/group, green * anti-LFA-1/anti-MAC-1 mAbs + aQDs vs aQDs group, Two-way ANOVA test). (C) Quantification of blood perfusion velocities in different experimental groups at t=1 h. (mean ± SEM, n = 3 mice/group, One-way ANOVA test).

3.5.4.1 Effects of LFA-1 and Mac-1 on velocity of crawling neutrophils in inflammation

The effects of LFA-1 and MAC-1 on the velocities of crawling neutrophils induced by aQDs were further investigated. The patterns of recruited neutrophils after the administration of different inhibitors were depicted in Fig.27. There was an obvious trend of increased numbers of tethering, adherent, and crawling neutrophils in the group pretreated with anti-MAC-1 mAbs compared to only aQDs application, both at 5-15 minutes and 55-65 minutes. Regarding the velocity of crawling neutrophils at 5-15 min, there were no significant alterations observed after pretreatment with either anti-LFA-1 or anti-MAC-1 mAbs compared to only aQDs application. However, at 55-65 minutes, both inhibitors were able to reverse the decreased velocities of crawling neutrophils induced by aQDs (8.45 ± 0.37 um/min) to 12.18 ± 1.14 um/min and 11.31 ± 0.30 um/min, respectively, although the velocities did not return to the levels observed in the control group at the same time (16.60 ± 1.52 um/min).

These findings suggest that LFA-1 and MAC-1 play a role in influencing the crawling step of neutrophil recruitment induced by aQDs in the pulmonary microcirculation. It appears that aQDs can slow down the crawling velocities of recruited neutrophils through the involvement of LFA-1 and MAC-1. However, after inhibiting the effects of LFA-1 and MAC-1 with specific antibodies, the crawling velocities of neutrophils may be restored, indicating that these adhesion molecules are responsible for the observed slowdown in neutrophil crawling.

A

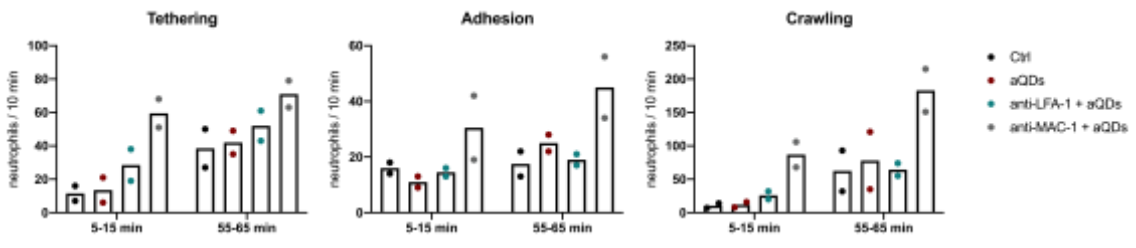

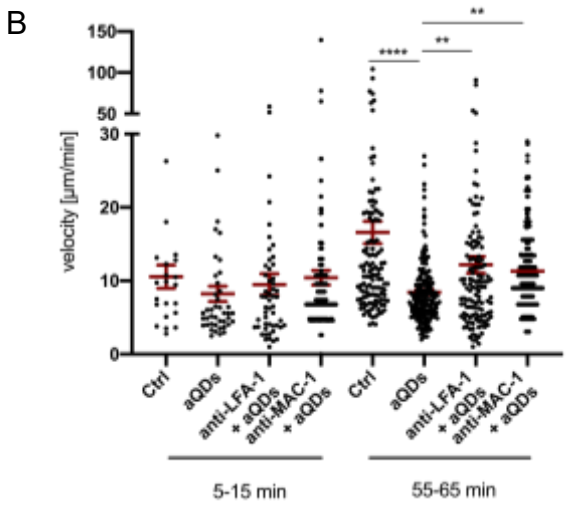

Figure 27. Effects of LFA-1 and MAC-1 on neutrophil interaction patterns in the pulmonary microcirculation.

Quantification of tethering (A), adhesion (B), and crawling (C) neutrophils in healthy mice pretreated with either anti-LFA-1 or anti-MAC-1 mAbs after QDs exposure are shown (in the time periods of 5-15 and 55-65 min) (Mean value, n = 2 mice/group). (D) Velocities of crawling neutrophils in different conditions and times are shown. (mean ± SEM, n = 22-365 neutrophils in 10 min form 2 mice/group, One-way ANOVA test).

3.6 Analysis of chemokine concentrations in blood serum after treatment with QDs and inhibitors/neutralizing antibodies

3.6.1 Dynamics of chemokine concentrations following different applications

The distribution and presence of QDs in blood can influence the overall functionality of the cardiovascular system and affect other organs. Given the previously observed effects of i.v. application of aQDs on leukocyte recruitment in the pulmonary microcirculation by L-IVM, we sought to investigate further the systemic change in the circulatory system following QDs application. To this end, the Bio-Rad mouse chemokine 31-plex assay, as described in section 2.2.10, was employed to detect changes in chemokine concentrations in the circulatory system after various treatments. Data analysis was conducted using the “z score” and “pheatmap” package (Kolde R, 2019, R package version 1.0.12) in R software

(R-4.2.3) to visualize the chemokine concentration changes detected in serum samples (Fig. 28).

The heatmap depicts the dynamic changes in chemokine levels in the systemic circulation following QDs challenge, with LPS serving as the positive control. Both cQDs and aQDs application for 1h or 24h resulted in increased concentrations of certain chemokines, some of which showed similar patterns of change as observed with LPS stimulation. Notably, chemokines such as CCL22, CCL27, IL-4, CXCL12, and CXCL13 exhibited increased levels following cQDs 1h application, while IL-6, CXCL10, CCL24, IL-1b, and IFN-gamma showed increased levels after aQDs 1h application. Furthermore, aQDs were found to enhance the levels of chemokines, including CCL3, IL-10, CCL4, and CXCL11, while decreasing the levels of chemokines such as IL-16, CX3CL1, CCL1, and CCL12 after 1h. After 24h of application, aQDs significantly increased the levels of IL-4, IL-1b, GM-CSF, IFN-gamma, TNF-α, and certain CXC and CC chemokines in the systemic circulation. On the other hand, cQDs mainly increased the level of TNF-α at this time point.

As visualized by the heatmap, there were global alterations in chemokine levels across different treatments, highlighting specific shifts in chemokine patterns in the systemic circulation. In the next chapter, we will further analyze and delve into the specific changes observed in some chemokines.

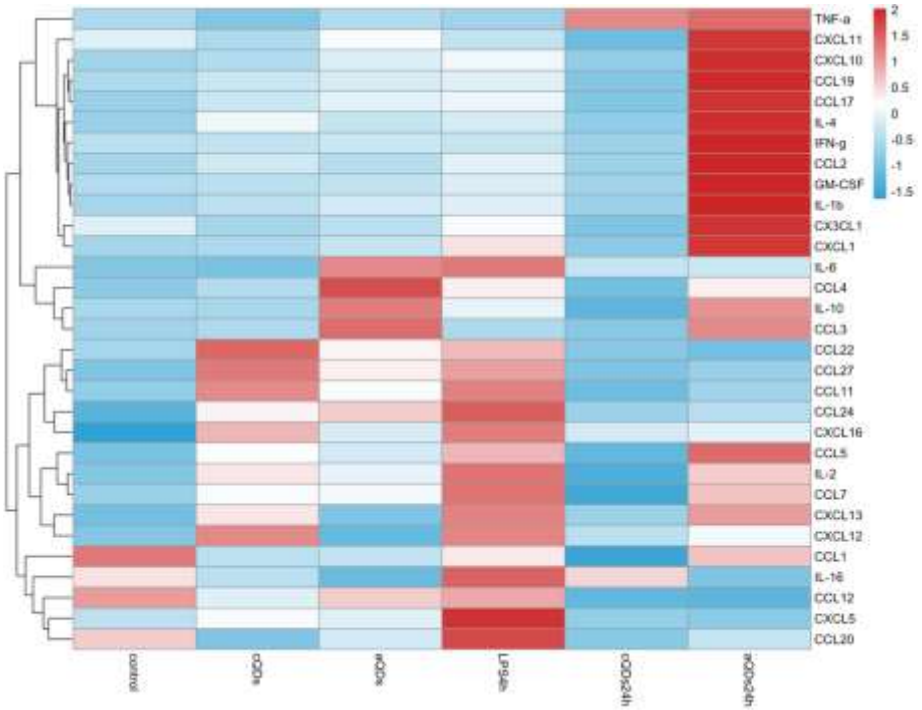

Figure 28. Heatmap of chemokine concentration alterations in the systemic circulation after treatments with QDs and LPS as well as under control conditions.

After treatments of QDs (1 pmol/g) i.v. for 1h or 24h and LPS (0.1 µg/mouse) by instillation for 4 h as positive control, the blood was collected to obtain plasma for Bio-Plex Pro Mouse Chemokine Panel analysis. Data in columns represents an average value from 3 to 4 biological replicates. The color key is presented by row Z-score, indicating the level of expression (low: blue; high: red). The heatmap (Kolde R, 2019, R package version 1.0.12) also includes hierarchical clustering analysis to identify patterns and relationships between the chemokines. Graphic was edited using R software (R-4.2.3).

3.6.2 Differential effects of various treatments on chemokine expression

The global heatmap provided an overview of the relative changes in chemokine concentrations under various conditions, but it did not provide absolute differences of individual chemokines. To focus on this issue, we selected several promising chemokines from the heatmap for further analysis (Fig.29).

IL-6 is a multifunctional chemokine produced by various immune cells that exhibits both pro- and anti-inflammatory properties. It promotes inflammatory events by activating and proliferating lymphocytes, inducing the differentiation of B cells, recruiting leukocytes, and triggering an acute phase protein response to physiologic stimuli. IL-6 exhibits both local and systemic effects in response to physiological stimuli as needed. IL-10 is an anti-inflammatory chemokine, which is mainly produced by monocytes and lymphocytes, usually followed by secretion of proinflammatory factors, such as IL-1, IL-16, and TNF-α. IL-10 exerts its effects through autocrine or paracrine signaling, modulating the localized inflammatory response, and also exhibits endocrine effects, regulating inflammation at the systemic level (Stenvinkel et al. 2005). Significant changes in the concentrations of IL-6 and IL-10 have been detected after the different treatments. Specifically, the level of IL-6 was significantly higher after 4 h of LPS treatment (76.24 ± 14.19 pg/ml) compared to control values (9.14 ± 3.69 pg/ml). An increased IL-6 concentration (72.28 ± 36.50 pg/ml) was observed in the aQDs 1 h group. Similarly, an increased in IL-10 was also observed in the aQDs 1 h group (898.00 ± 159.90 pg/ml) compared to the controls (393.10 ± 108.90 pg/ml), although the difference was not statistically significant.

Additionally, macrophage inflammatory protein (MIP)-1a/CCL3 and MIP-1b/CCL4 are chemotactic and proinflammatory regulators expressed by lymphocytes and monocytes/macrophages (Maurer and von Stebut 2004). CCL3 is known to mediate neutrophil recruitment in murine immune inflammation, depending on the TNF-α pathway, which is also a proinflammation cytokine produced by various cells, including macrophages, lymphocytes, and endothelial cells (Ramos et al. 2005; Reichel et al. 2009). Our results showed a significant increase of CCL3 levels in the aQDs 1 h group to 17.35 ± 3.10 pg/ml, compared to controls (4.76 ± 1.53 pg/ml), while a trend towards an increase in CCL4 concentration was observed in the aQDs 1 h group (139.50 ± 33.92 pg/ml vs 60.19 ± 14.77 pg/ml). However, there was no significant difference in TNF-α concentrations observed in the different treatments.

In addition to the previously mentioned chemokines, macrophage-derived chemokine (MDC)/CCL22 was also found to be altered in response to the various applications. MDC/CCL22 is a proinflammatory chemoattractant for CCR4-expressing Th2 lymphocytes, monocyte-derived dendritic cells, and natural killer cells, and is known to regulate pulmonary levels of MIP-2 and MIP-1 (Richter et al. 2014). Our results showed that aQDs 1 h and LPS 4 h treatments induced higher CCL22 levels (92.26 ± 7.71 pg/ml; 110.40 ± 16.82 pg/ml) compared to controls (57.58 ± 5.00 pg/ml).

Eotaxin/CCL11 and Eotaxin2/CCL24, on the other hand, are known to attract CCR3-expressing eosinophils, Th2 lymphocytes, basophils, mast cells, neutrophils, and macrophages in response to allergen challenge. Notably, a significant increase in Eotaxin2/CCL24 levels (2243.00 ± 164.40 pg/ml vs 1688.00 ± 106.80 pg/ml) and a trend of enrichment in Eotaxin/CCL11 (335.70 ± 79.18 pg/ml vs 171.70 ± 24.76 pg/ml) were observed in the cQDs 1 h treated group compared to the corresponding controls. Moreover, LPS treatment for 4 h also significantly induced Eotaxin2/CCL24 levels to 2694.00 ± 108.10 pg/ml.

Different modified QDs induce changes in some chemokines. Overall, these individual alterations of chemokines in the systemic circulation provide further insights into the effects of the different treatments on the immune response.

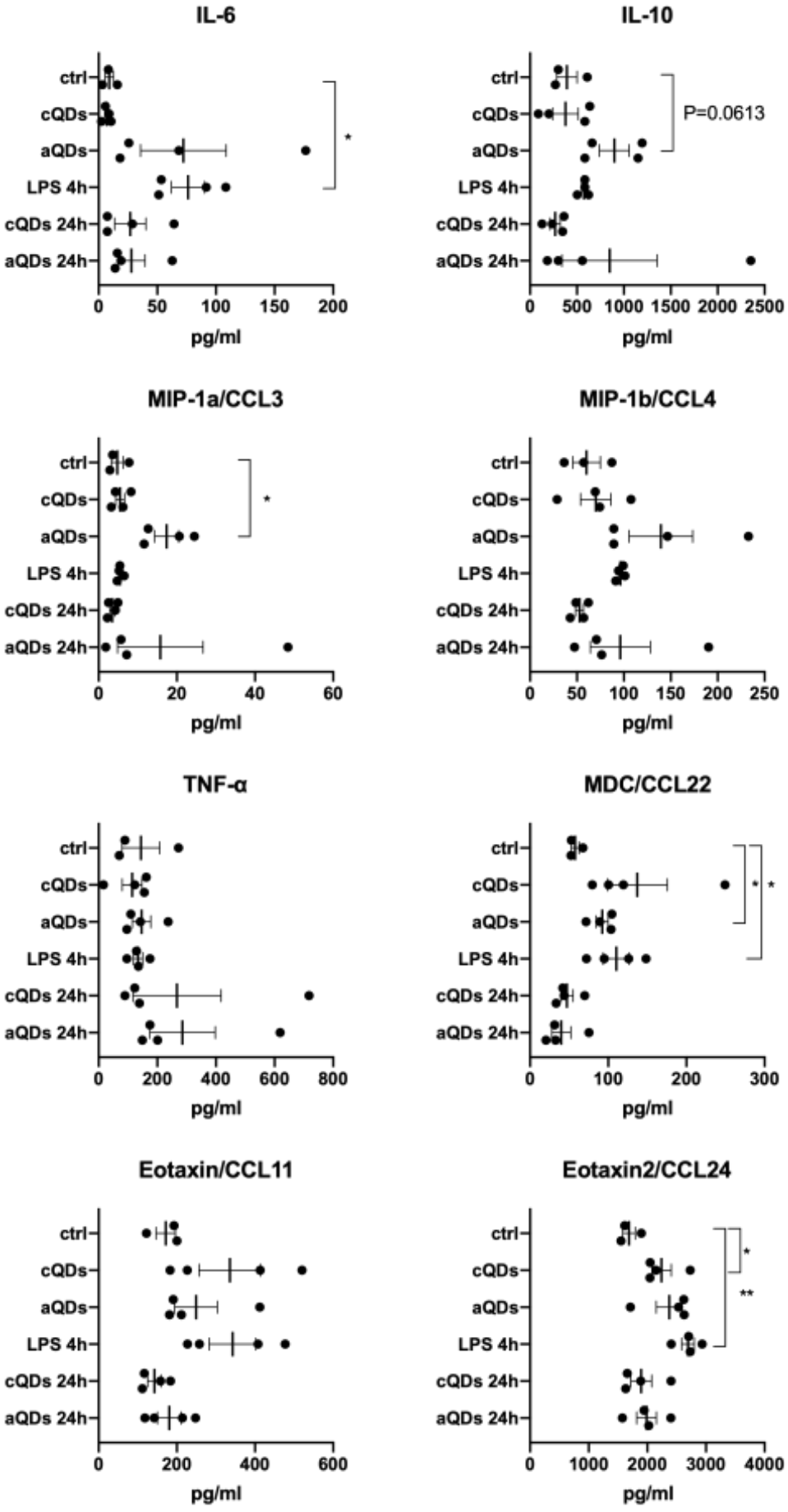
IL-6
ctrl
cQDs
aQDs
LPS 4h
cQDs 24h
aQDs 24h
0
50
100
150
200
pg/ml
*
IL-10
P=0.0613
0
500
1000
1500
2000
2500
MIP-1a/CCL3
0
20
40
60
MIP-1b/CCL4
0
50
100
150
200
250
TNF-α
0
200
400
600
800
MDC/CCL22
0
100
200
300
**
Eotaxin/CCL11
Eotaxin2/CCL24
0
1000
2000
3000
4000

Figure 29. Alterations of chemokine concentrations in blood serum after aQDs, cQDs (both for 1 h and 24 h), LPS (4 h) and vehicle control (1 h) applications, including IL-6, IL-10, MIP-1a/CCL3, MIP-1b/CCL4, MDC/CCL22, TNF-α, Eotaxin/CCL11, and Eotaxin2/CCL24, respectively. (mean ± SEM, n = 3~4 mice/group, Student's t test).

3.7 The effect of extracellular ATP (eATP) on neutrophil recruitment

3.7.1 eATP levels in systemic circulation and BALF following QDs application

Based on our findings, aQDs were found to increase chemokine levels in the systemic circulation and induce the neutrophil recruitment in the pulmonary microcirculation. We hypothesized that aQDs in the blood might cause cell stress or damage, leading to the release of damage-associated molecular patterns (DAMPs) that activate immune responses. eATP acts as a pro-inflammatory stimulus triggered by tissue injury and robust activation of immune cells (Di Virgilio et al. 2017). In a mouse model of acute lung injury, eATP mediated the later stages of neutrophil recruitment to the lung, such as emigration (Shah et al. 2014).

To explore the potential role of eATP in the observed immune responses, we conducted a detection of eATP in plasma and BALF after QDs treatments (Fig.30). There was a noticeable trend of increased eATP concentrations after 1 h application of aQDs, and this increase became significant after 24 h of aQDs administration in the systemic circulation compared to controls, which might be released from stressed cells and potentially activate inflammation. The P2X7R antagonist did not block eATP release. On the other hand, in the BALF, aQDs application to the systemic circulation results in a slight decrease in eATP levels after 1 h, and the P2X7R antagonist further reduces these levels. Interestingly, after 24 h, eATP levels in BALF return to control levels which might indicate a resolution of inflammation over time.

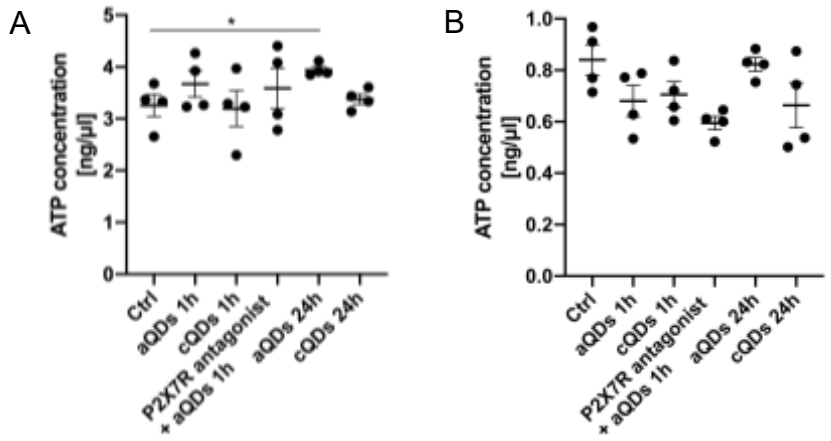

Figure 30. eATP concentrations after QDs application.

In freshly prepared plasma (A) and BALF (B) samples, collected from mice after the application of aQDs and cQDs, eATP concentrations were determined. (mean ± SEM, n = 4 mice, Student's t test).

3.7.2 P2X7R activation is involved in the cascade of neutrophil recruitment induced by aQDs

P2X7R is expressed on inflammatory cells such as monocytes, macrophages, DC cells, and lymphocytes, and it plays an important role by interacting with eATP (Tran et al. 2010). The receptor acts as an ATP-gated cation channel, allowing an influx of calcium ions (Ca^{2+}) and sodium (Na^{+}) and efflux of potassium (K^{+}). Upon activation, P2X7R and subsequent ion flux trigger various cellular responses, including inflammation and neutrophil recruitment (da Silva et al. 2013; Janks, Sprague, and Egan 2019; Rotondo et al. 2022). However, the function of P2X7R in recruiting neutrophils in the pulmonary microcirculation is not known.

To investigate the role of P2X7R in aQDs-induced neutrophil recruitment and blood perfusion changes, we administered a P2X7R antagonist (A438079, 30 µg/mouse, BioTechne GmbH, Germany) intravenously 30 min prior to L-IVM and aQDs injection. In Fig. 31 A and B, the results showed that the P2X7R antagonist attenuated aQDs-induced neutrophil recruitment, and the trend in neutrophil numbers was similar to that of controls, with neutrophil numbers of 1.98 ± $0.61/10^4 um^2$ at 60 min. Furthermore, compared to 149.2 ± 8.2 um/s in the aQDs

group, the blood flow velocity in the aQDs group pretreated with the P2X7R antagonist increased significantly to 199.0 ± 11.0 um/s, reaching control group levels (201.6 ± 10.0 um/s).

These results indicate that the P2X7R antagonist can reduce inflammation and restore the diminished blood perfusion induced by aQDs. This suggests that targeting the P2X7R pathway may be a potential therapeutic approach to mitigate the adverse effects of aQDs on the pulmonary microcirculation and inflammation.

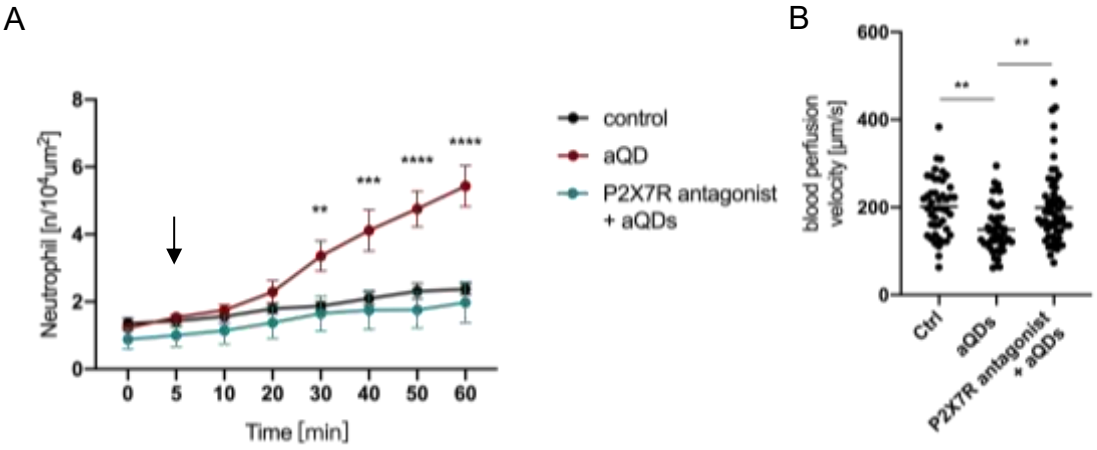

Figure 31. Neutrophil recruitment induced by aQDs was related to P2X7R activation in the pulmonary microcirculation.

(A) Quantification of recruited neutrophils over time after aQDs application in mice with and without pre-treatment by i.v. injection of P2X7R antagonist (A438079, 30 µg/mouse) 30 min prior to L-IVM (aQDs injection at 5 min indicated by arrow). (mean ± SEM, n = 4 mice/group, * compared with aQDs group, Two-way ANOVA test). (B) Quantification of blood perfusion velocity after 1 h of L-IVM. (n = 3 mice/group, in P2X7R antagonist + aQDs group, n = 4 mice/group, One-way ANOVA test,).

3.7.3 Effects of P2X7R antagonist on aQDs induced neutrophil motility changes in the pulmonary microcirculation

To further investigate the role of P2X7R in neutrophil recruitment induced by aQDs, we examined the motility of neutrophils after pretreatment with the P2X7R antagonist in detail. Neutrophils were imaged at 5 s intervals, and individual neutrophils were automatically tracked using Fiji, as described in section 3.3.2.

The results depicted in Fig.32 show that a 30 min pretreatment with the P2X7R antagonist significantly reversed the reduced crawling velocity of neutrophils induced by aQDs. The crawling velocity increased from 8.23 ± 1.05 µm/min to 14.04 ± 0.91 µm/min. After 60 min, the crawling velocity of neutrophils in the P2X7R antagonist + aQDs group (12.96 ± 0.44 µm/min) was significantly higher than that of the aQDs group alone (8.45 ± 0.37 µm/min), but still lower than that of the control group (16.60 ± 1.52 µm/min).

These findings demonstrate that the P2X7R antagonist has a significant impact on the crawling velocity of neutrophils in response to aQDs. Ion flux, especially Ca^{2+} inflow and K^{+} outflow, has been shown to be related to neutrophil activation and recruitment (Immler, Simon, and Sperandio 2018; Immler et al. 2022). We speculate that this antagonist likely acts through this pathway to effectively reverse the initial decrease in crawling velocity induced by aQDs and partially restore the velocity. However, since the restoration of crawling velocity does not fully reach the level observed in the control group, it suggests that other factors may also contribute to the observed effect.

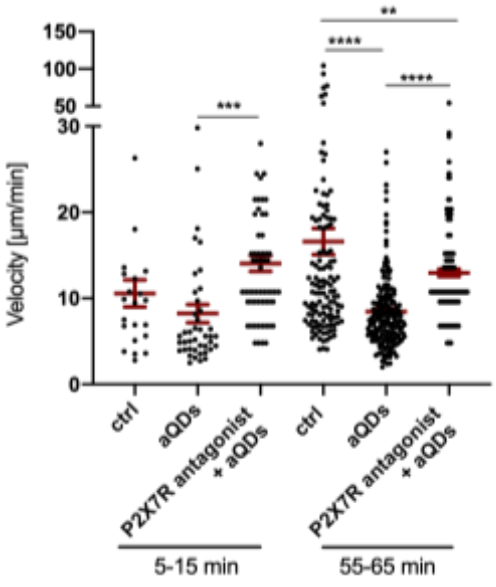

Figure 32. Pretreatment with P2X7R antagonist restores crawling velocity of neutrophils.

The crawling neutrophils in time-lapse movies taken at 5-15 min and 55-65 min after aQDs application were automatically tracked using Fiji, and the velocities were analyzed. The velocities of different treatments and time points are shown in the graph. (mean ± SEM, n = 22-247 neutrophils in 10-min interval form 2 mice/group, One-way ANOVA test).

3.8 Platelet responses to QDs application in the pulmonary microcirculation

In addition to analyzing neutrophil immunoreactivity in the pulmonary microcirculation, we also investigated the effects of QDs application on platelets. DyLight649-labeled anti-GPIb-V-IX complex mAbs were injected intravenously before L-IVM to label platelets, and QDs were subsequently administered intravenously after baseline recording. The percentage of the platelet-covered area in each field of view was quantified, and the results were presented as the mean fold change in percentage normalized to 0 min for each condition. The platelet results under different conditions, including healthy, LPS-treated, and Bleomycin-treated mice after exposure to QDs, were presented in section 3.1.2.

In healthy mice (Fig.33 A), cQDs induced an increase in the platelet-covered area at t=10 min, peaking at 2.37 ± 0.27 compared to 1.26 ± 0.17 in controls at this time, and then decreased to baseline levels until 60 min. However, in LPS-treated mice (Fig.33 B), cQDs only significantly increased the platelet-covered area at 30 min, with a percentage of 2.07 ± 1.15 compared to 0.76 ± 0.03 in LPS-treated control mice. On the other hand, in Bleomycin-treated mice (Fig.33 C), cQDs induced a longer duration of platelet-covered area increase, ranging from 10 min to 30 min. In all conditions, exposure to aQDs did not significantly alter platelet dynamics, and the overall trend was similar to the respective control groups.

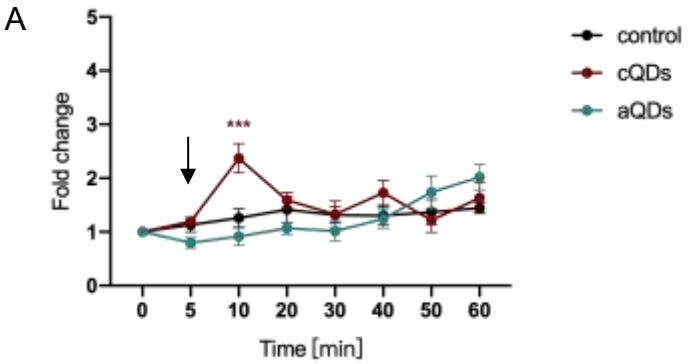

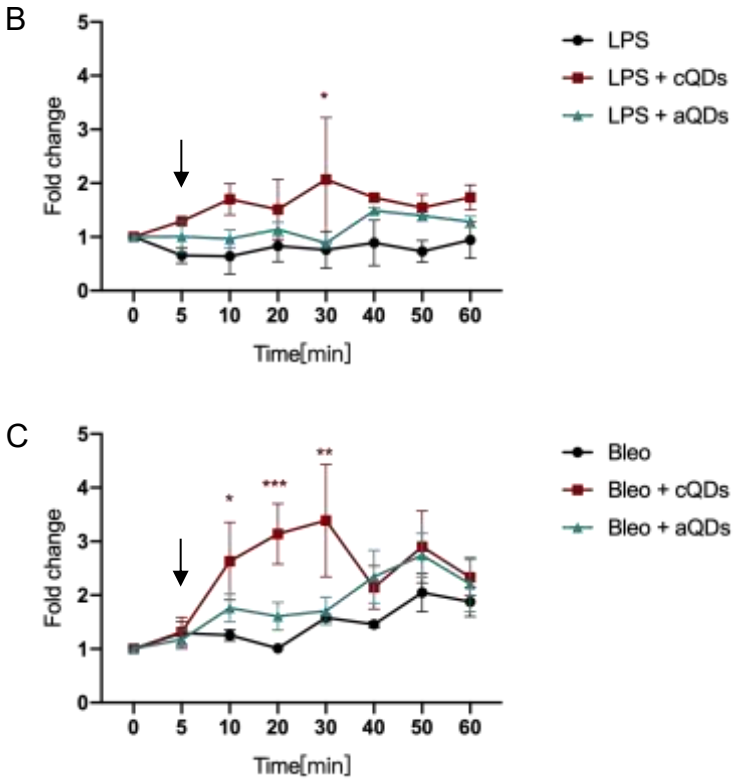

Figure 33. Quantification of the platelet-covered area after QDs application in different tissue conditions.

The fold change in the percentage of platelet-covered area in the fields of views in the pulmonary microcirculation of healthy (A), LPS-treated (B), and Bleomycin-treated (C) mice during 60 min of L-IVM was quantified. QDs were applied at 5 min (indicated by the arrow). (mean ± SEM, n = 2~4 mice, * compared with the control group of each respective condition, Two-way ANOVA test).

3.9 Changes in BAL parameters and blood cell composition following QDs application

3.9.1 Analysis of BAL cell numbers and composition

As described in section 3.1.3, BAL cells were collected and analyzed. The results presented in Fig.34 show that the application of aQDs and cQDs for 1 h did not have any significant effects on BAL parameters, including total cell numbers and cell counts of macrophages, neutrophils, lymphocytes, and monocytes in healthy and Bleomycin-treated (14 d) mice. However, in LPS-treated mice after 24 h, the

application of both QDs types (for 1 h) resulted in decreased numbers of total BAL cells, neutrophils, and monocytes.

These findings suggest that the application of QDs to the systemic circulation impacts the BAL cell composition under pathophysiologic tissue conditions induced by prior LPS treatment. However, this effect could not be observed through the L-IVM approach used in this thesis.

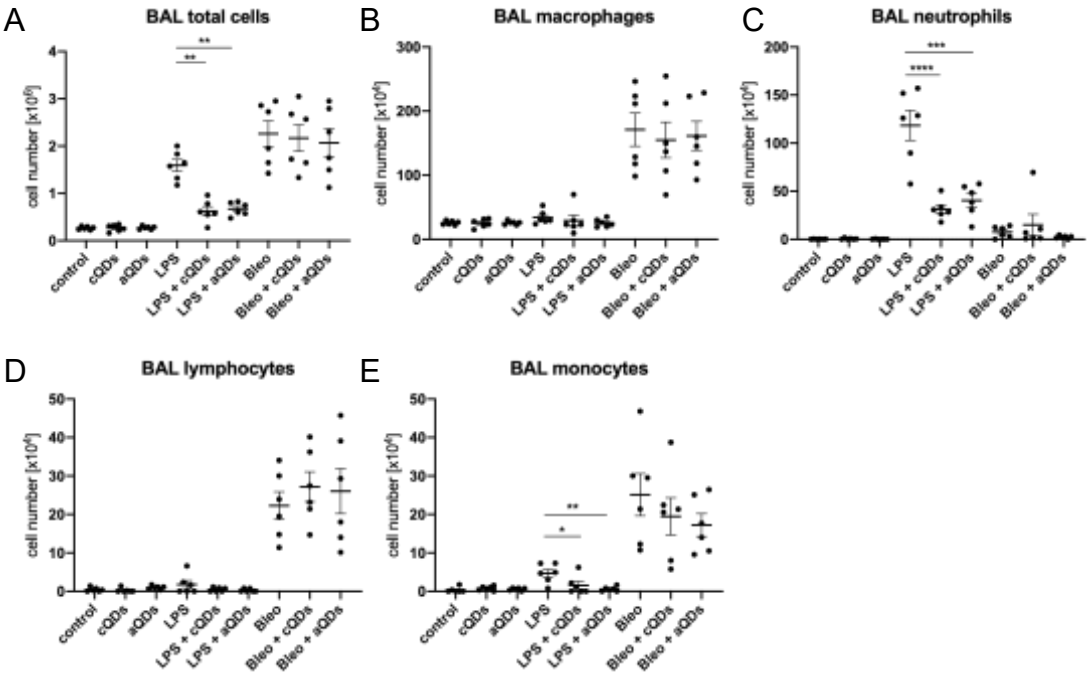

Figure 34. BAL cell analysis after QDs application in healthy, LPS-treated, and Bleomycin-treated mice.

Quantification of total BAL cells (A), macrophages (B), neutrophils (C), lymphocytes (D), and monocytes (E) after L-IVM was shown (QDs were applied 1 h prior to lavage). May Grunwald-Giemsa stained cytospins of BAL cells were analyzed. (mean ± SEM, n = 6 mice/group, One-way ANOVA test).

3.9.2 Alterations in BALF dsDNA and protein levels

Following the methodology described in section 3.1.3, the first 2 ml of BALF supernatant was collected from the mice after 1 h of L-IVM for analysis of dsDNA and protein levels. As shown in Fig.35, there were no significant differences in protein levels after QDs application under the three investigated conditions. However, after 24 h of LPS administration, the dsDNA levels in BALF supernatant

significantly decreased with aQDs application to 22.87 ± 4.73 ng/ml compared to controls (82.67 ± 18.20 ng/ml), with a trend of reduced levels also in the cQDs group (28.35 ± 8.88 ng/ml).

These findings suggest that surface-modified QDs may have a potential impact on the release of dsDNA in the alveolar space, particularly under LPS-treated conditions. Further investigations are warranted to elucidate the underlying mechanisms and explore the implications of these observations.

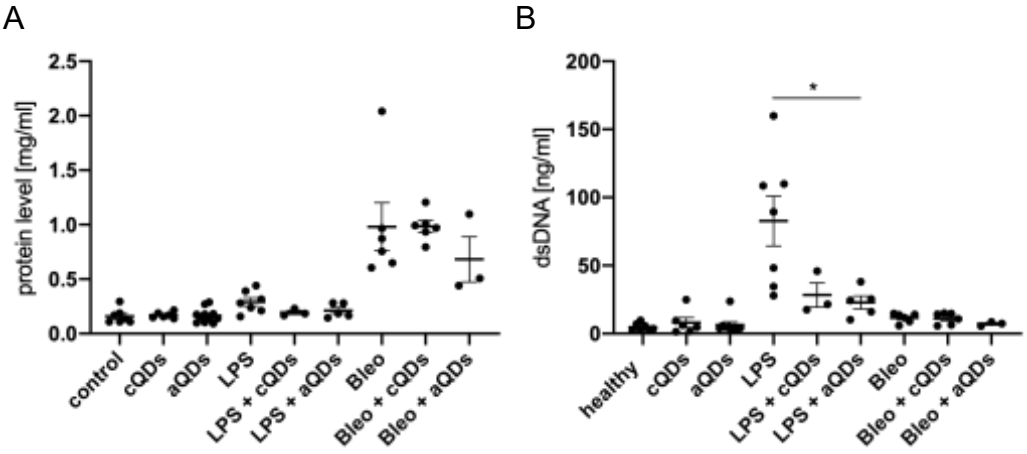

Figure 35. dsDNA and protein level of BALF supernatant.

The first 2 ml of BALF supernatant was collected and assessed using the BCA protein assay kit and PicoGreen dsDNA assay kit. The concentrations of protein (A) and dsDNA (B) in the three conditions (+/- QDs) are shown. (mean ± SEM, n = 6~7 mice/group, One-way ANOVA test).

3.9.3 Changes in immune cell population in the systemic circulation

To investigate the systemic changes in blood immune cells, blood samples were collected from the angular vein following the application of QDs (i.v.) for 1 h/24 h and LPS (instillation) for 4 h. There were not many alterations observed in white blood cell (WBC) numbers after both QDs application (Fig.36). However, aQDs increased neutrophil cell counts and their percentages of WBC compared to controls (0.85 ± 0.09 K/µl vs 0.45 ± 0.04 K/µl; 17.85 ± 1.38 % vs 11.45 ± 0.98 %) and decreased the percentages of monocytes present in the WBC to 1.95 ± 0.13 % compared to control values of 5.05 ± 1.26 %. Interestingly, the application of cQDs for 24 h induced a decrease in WBC and lymphocyte counts.

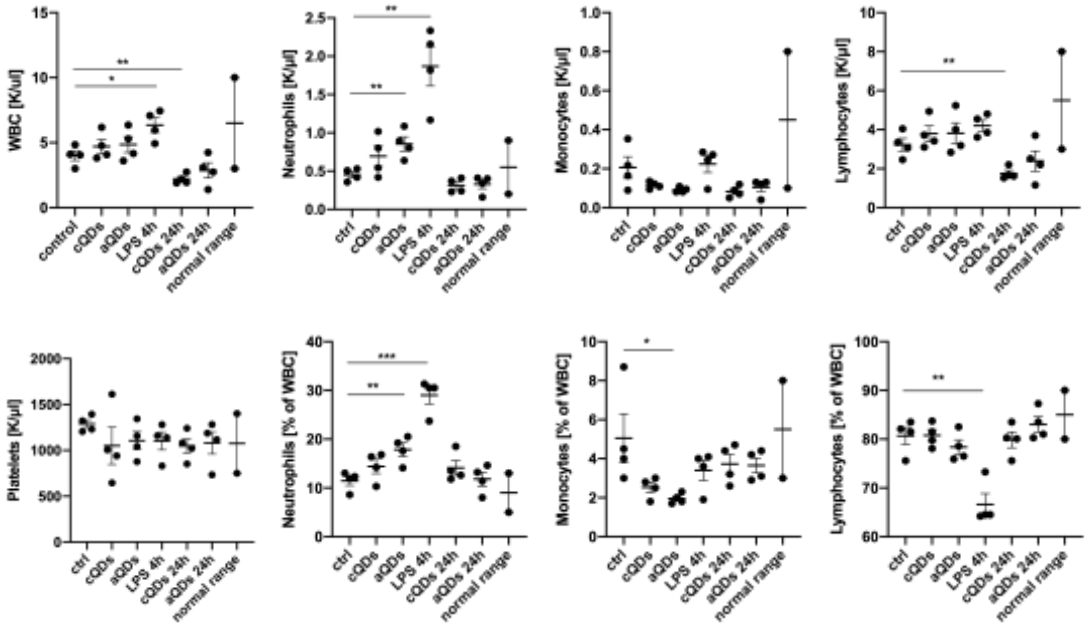

Figure 36. Hematological analysis after QDs application.

Following cQDs and aQDs application (i.v.) for 1 h/24 h and LPS (instillation) for 4 h, blood samples were collected from the angular vein for hematological analysis. The numbers of immune cells and their corresponding percentages of WBC are displayed. (mean ± SEM, n = 4 mice/group, Student's t test).

4. Discussion

4.1 Real-time monitoring of immune responses induced by NPs using L-IVM

Engineered NPs have emerged as a promising tool for precision drug delivery, diagnostics, and biomedical imaging modalities when applied into the blood circulation (Han et al. 2019; Mitchell et al. 2021). However, the interaction of NPs with the immune system can have complex effects and may lead to immunotoxicity. Different surface-modified NPs have been utilized to study their interaction dynamics under pathological conditions (Uhl et al. 2018). When NPs encounter immune cells, such as macrophages and monocytes, they can trigger immune responses, including the release of various cytokines and chemokines. These immune responses can mediate local and systemic inflammatory reactions (Elsabahy and Wooley 2013). These effects may lead to tissue damage, exacerbate pre-existing inflammatory conditions, or induce new inflammatory responses.

Furthermore, it is important to consider the route of NP exposure. Apart from i.v. application, another significant route through which NPs can enter the bloodstream is by inhalation. Inhaled engineered NPs that deposit in the alveolar region have the capability to break down mucus and cross the epithelial-endothelial barrier, allowing them to access the bloodstream (Kreyling 2010; Thompson et al. 2014; Chen et al. 2015). In addition to affecting the lungs, inhaled NPs can also modulate immune responses in other organs through cytokines released from the lungs or by directly translocating from the lungs to distant organs (Nurkiewicz et al. 2006; Thompson et al. 2014).

Previous studies have shown that exposure to various types of NPs, such as carbon NPs, carbon nanotubes, TiO_2 NPs, gold NPs, and silver NPs, can induce lung inflammation and increase levels of inflammatory factors through different routes of administration, including inhalation, intratracheal administration, as well as i.v. injection (Jacobsen et al. 2009; Ng et al. 2016; Sagawa et al. 2021). Additionally, NPs have been shown to exacerbate pre-existing respiratory inflammation induced by various factors like exposure to LPS or allergens such as dust mites (Zhou, Jin, and Ma 2023). Ramos-Gomes et al. employed an ex vivo lung

model filled with agarose and utilized L-IVM to visualize NP interactions with macrophage/monocyte in mice lungs (Ramos-Gomes et al. 2020).

While many studies have focused on the later immune responses of the lungs to NPs, the early innate immune response to NP exposure in the pulmonary microcirculation, under both healthy and pathophysiologic conditions, remains largely elusive. To visualize and quantify the dynamics of NPs and the associated innate immune responses in the pulmonary microvasculature in real-time, we employed L-IVM in the alveolar region of murine lungs. Given that neutrophils serve as the frontline immune responders against invading pathogens and are usually the initial cells to mobilize towards the site of inflammation (Grommes and Soehnlein 2011), we mainly focus on neutrophils in the pulmonary microcirculation. To achieve this, we utilized an optimized intercostal window technique with continuous negative reversible vacuum pressure, originally developed from Mark R. Looney (Looney et al. 2011; Headley et al. 2016). This approach allowed us to study dynamic NP interactions and cellular responses in real-time in live mice. To the best of our knowledge, our study is the first to utilize L-IVM to directly examine the local immune response, particular neutrophil recruitment, elicited by different surface-modified NPs in the pulmonary microvasculature of live mice.

4.2 Rapid recruitment of neutrophils in pulmonary microcirculation induced by aQDs

In our study, two subsets of NPs with distinct characteristics, one exhibiting low potential (aQDs) and the other exhibiting high potential (cQDs) to interact with biomolecules and cells (Rehberg et al. 2010), have been employed as fluorescent mimics of NPs in our study. These NPs were selected based on their brightness, photostability, broad excitation spectrum, high emission intensity, and narrow emission spectra (Wegner and Hildebrandt 2015). PEG is a biocompatible polymer that can modify the physical and chemical characteristics of molecules, such as their electrostatic binding and hydrophobicity, to increase their retention time in the circulating system, reduce the interaction with plasma proteins and immune cells, and prevent renal excretion. PEGylation is a widely used technique in drug delivery and biomedical research, which enhances the pharmacokinetics and

pharmacodynamics of drugs, reduces immunogenicity and toxicity, and improves their therapeutic efficacy (Harris and Chess 2003; Veronese and Mero 2008).

The QDs used in our study are obtained from a commercial company and are functionalize with either carboxyl residues directly or amino derivatized PEG. In our previous research, different surface modifications of QDs exhibit distinct effects on their interaction within the microvasculature, as well as their biodistribution and proinflammatory effects in postcapillary venules of skeletal muscle tissue (Rehberg et al. 2010). Under physiological conditions, cQDs, but not aQDs, induced leukocyte (neutrophil) recruitment, mediated by the uptake of cQDs by perivascular macrophages, leading to mast cell activation and subsequent endothelium-mediated leukocyte recruitment (Rehberg et al. 2010). However, under ischemia-reperfusion injury, aQDs, but not cQDs, induced leukocyte transmigration, likely attributed to the recruitment of endogenous microparticles that stimulated endothelial cells (Rehberg et al. 2012).

In our current research, we observed that after i.v. application of QDs, aQDs evoked immediate neutrophil recruitment in the pulmonary microcirculation at 20 min post-exposure, while cQDs could induce a slight degree of inflammation after 60 min. The increased neutrophil numbers were also observed in the systemic circulation. These observations align with previous studies showing the different surface-modified NPs can induce varying degrees of lung injury and inflammation depending on the dose and time post-exposure (Roberts et al. 2013; Ho et al. 2013). Specifically, they found that after intratracheal instillation, aQDs at a dose of 12.5 μg induced a greater increase in lactate dehydrogenase (LDH) and albumin levels in BAL at day 1 compared to cQDs at the same dose. These results suggest that under certain conditions, exposure to aQDs can induce more general cytotoxicity and damage to the air blood barrier compared to cQDs (Roberts et al. 2013). Ho et al. examined the long-term impact of PEG modification on QDs in mice after intratracheal instillation of 12 μg and 60 μg doses. They discovered that both types of QDs (60 μg) increased inflammatory cells, protein levels, and LDH activity in BAL on day 2, 17, and 90. On day 17, both aQDs and cQDs (60 μg) induced similar pathological manifestations, including neutrophil and interstitial lymphocyte infiltration, and a granulomatous reaction. However, PEG modification was found to mitigate the granulomatous reaction at day 90. Additionally, both types of QDs (12 μg and 60 μg) increased the expression of proinflammatory

cytokines and chemokines on day 17. These findings demonstrate that PEG modification does not fully prevent inflammation induced by QDs over an extended period of time after their application to the lung (Ho et al. 2013).

Under normal homeostatic conditions, organs like the liver and adipose tissue contain few neutrophils (Rosales 2018). Typically, various sentinel cells including macrophages, dendritic cells, mast cells, and endothelial cells are activated in response to localized tissue infections or injury. These cells release proinflammatory signals and chemokines which attract recruited neutrophils to the site of infection or injury (Phillipson and Kubes 2011). Moreover, patrolling monocytes along blood vessels may infiltrate affected tissues early in the infection process and contribute to neutrophil recruitment (Auffray et al. 2007). However, it is important to note that in the pulmonary microcirculation, neutrophils play a crucial role in defending against invading pathogens, unlike in other organs where macrophages dominate the role in immune defense (Kolaczkowska and Kubes 2013; Granton et al. 2018; Liew and Kubes 2019). The observation of “baseline” neutrophils at t=0 in L-IVM provides valuable insights of the “marginated pool” into the lung’s host defense mechanism. These neutrophils are already present in the pulmonary microcirculation, patrolling and surveying the microenvironment for potential threats. The increased neutrophil numbers, that were observed after aQDs application in both L-IVM and hematological analysis, provide further evidence that aQDs trigger a specific response from the lung, leading to the recruitment of additional neutrophils from both the marginated pool and the circulating blood. This response indicates the active involvement of neutrophils in the pulmonary microcirculation following aQDs exposure, likely in response to potential stress or injury caused by the NPs.

Studies have shown that various NPs including Carbon, TiO_2, and Au NPs after inhalation can aggravate allergic airway inflammation and airway fibrosis in mice (Ryman-Rasmussen et al. 2009; Inoue et al. 2010; Rossi et al. 2010). Furthermore, pre-existing lung inflammation, such as that induced by LPS pretreatment via intratracheal administration, has been shown to enhance the inflammatory cytokine responses to NPs, leading to worsened inflammation (Parhiz et al. 2022). Interestingly, the surface modifications of NPs can have a significant impact on their immunomodulatory properties under inflammatory conditions. For instance,

zwitterionic particles may have a pro-inflammatory effect, while tetraethylene glycol-modified particles may exhibit an anti-inflammatory effect (Moyano et al. 2016). This suggests that the choice of NPs surface modification can have important implications for their biological effects in inflammatory conditions.

In our LPS-induced disease model, we observed that aQDs increased neutrophil numbers at an early time point beyond the levels of pre-existing inflammation, although the increase was not significant and did not alter after 60 min. The increased neutrophil levels observed in the LPS-treated group compared to healthy mice undergoing L-IVM might be attributed to the pre-sensitization of the immune response after LPS challenge, due to the intercostal surgery and L-IVM process.

In the Bleomycin-induced fibrosis disease model, a slight increase in neutrophil levels was observed after aQDs application, but it was not sustained over time. Engineered NPs have been utilized to target macrophages and epithelial-mesenchymal transition to mitigate lung fibrosis (Singh et al. 2022; Jin et al. 2023).

Furthermore, in both disease models, cQDs, but not aQDs, significantly elevated the platelet-covered area in the pulmonary microcirculation at an early timepoint, although these changes were transient. We also observed a trend of decreasing platelet count in the whole blood after cQDs application compared to the control group. Previous studies have shown that QDs can aggregate human platelets by upregulating surface expression of P-selectin and GPIIb/IIIa receptors (Samuel et al. 2015). Moreover, cQDs have been shown to cause more pulmonary vascular thrombosis and result in lower platelet counts in blood compared to aQDs due to their ability to activate the coagulation cascade (Geys et al. 2008). Our findings, obtained from both L-IVM and hematological analysis, are consistent with these previous results. Overall, after QDs application to disease models, we do not observe major changes in the first hour.

4.3 Preferential accumulation of recruited neutrophils in capillaries

Neutrophils are primarily recruited to postcapillary venules of the systemic microcirculation in response to inflammation in most organs. In the lung, these recruited

neutrophils tend to accumulate in small capillaries that interconnect the outsides of alveoli (Doerschuk 2000; Grommes and Soehnlein 2011; Rossaint and Zarbock 2013). The parenchyma of the lungs, which mainly comprises capillaries, is defined as vessels ranging smaller than 20-25 μm (Townsley 2012). The alveolar septal wall interstitium consists of collagen, elastin, fibroblasts, and the basement membrane, with a thickness smaller than 1 μm (Mercer, Russell, and Crapo 1994; Townsley 2012). In L-IVM, the diameter of lung microvessels was measured, and it was found that small pulmonary arterioles had a diameter of 24.9 ± 0.7 μm, while small venules had a diameter of 25.9 ± 0.7 μm (Tabuchi et al. 2008). Lung capillaries typically have a diameter ranging from 2-15 μm (Doerschuk et al. 1993). Yipp et al. conducted L-IVM experiments to investigate the distribution of recruited neutrophils and observed that adhesion, crawling, and tethering neutrophils were primarily located in vessels smaller than 10 μm. Fewer neutrophils were observed in vessels ranging from 11-20 μm and no neutrophils were observed transiting in vessels larger than 20 μm (Yipp et al. 2017).

The specific patterns of marginated neutrophils and recruited neutrophils in different types of vessels have not been well understood until now. In our study, we utilized L-IVM and labeled platelets with DyLight649-labeled anti-GPIb-V-IX complex to measure the alveolar septal thickness, which approximately represent pulmonary microvessels. We successfully distinguished and quantified neutrophil numbers in microvessels of different sizes and in the alveolar space. Our results showed that marginated neutrophils (at t=0) were predominantly present in vessels smaller than 20 μm, with a slightly higher accumulation in vessels smaller than 10 μm. After 1 h of exposure to aQDs, the recruited neutrophils remained localized in vessels smaller than 20 μm, but there was a greater increase in neutrophils in vessels ranging from 10-20 μm. Interestingly, marginated neutrophils were rarely observed in the alveolar space and vessels larger than 20 μm. However, following the inflammatory stimulus, recruited neutrophils increased in these regions. This finding provides novel insights into the distribution of marginated and recruited neutrophils in the pulmonary microcirculation in response to aQDs challenge.

4.4 Reduction in neutrophil crawling velocity induced by NP-induced inflammation

The classical neutrophil recruitment cascade involves several steps, including initial leukocyte slow rolling, adhesion strengthening, intraluminal crawling, and paracellular and transcellular migration, in most organs (Ley et al. 2007). However, in the lungs, due to the narrow diameter of capillaries, neutrophils undergo significant deformation to facilitate passage, and the rolling step is not included in the recruitment cascade. Instead, the process involves tethering, adhesion, crawling, and transmigration (Rossaint and Zarbock 2013; Maas, Soehnlein, and Viola 2018). Several studies have utilized L-IVM to investigate neutrophil motility in the pulmonary microcirculation and the reported velocity values have shown variation. For example, Looney et al. reported important insights into the velocity of neutrophils in different types of vessels. They found that the velocity of neutrophils in capillaries with a diameter ranging from 10-15 μm was approximately 0.91 μm/s. In medium-sized vessels with an average diameter of 30 μm, the transiting velocity of neutrophils reached up to 96 μm/s (Looney et al. 2011). Kreisel et al. observed a significant increase in neutrophil velocity to 9.68 μm/min after 5 min of LPS intratracheal challenge (Kreisel et al. 2010). Yipp et al. also used L-IVM to observe neutrophil motility in the pulmonary microcirculation of mice after i.v. injection of LPS. They categorized neutrophil motility into different stages based on the time spent and interactions with the vascular wall. In the steady state, approximately 35 % of neutrophils were in an adherent state, and crawling neutrophils typically moved less than 20 μm in a period of 10 min. After 20 min of LPS exposure, the displacement of crawling neutrophils significantly increased from 20 μm/10 min at baseline levels to 50 μm/10 min (Yipp et al. 2017). However, Ueki's research showed a decrease in neutrophil motility after the peak day (day 1) of neutrophil recruitment in mice infected with influenza virus intranasally. The neutrophils mainly exhibited slow motion, indicating that the movement of neutrophils could be impaired by influenza virus infection (Ueki et al. 2018). Additionally, Park et al. found that neutrophil motility initially increased within the first 3 h following LPS treatment and then decreased from 6 h (Park et al. 2019).

The classification method proposed by Yipp et al. (Yipp et al. 2017) allowed us to categorize neutrophils in the pulmonary microcirculation based on their duration

and motility during recruitment in the context of NPs exposure. By tracking single cells and examining their crawling velocity, we gained valuable insights into the motility and dynamics of neutrophils and their interactions with the endothelium. Our observations revealed that the crawling velocity of neutrophils immediately showed a trend of decreasing alteration after the application of both types of QDs. This effect was particularly evident and sustained after 60 min in the aQDs group. We hypothesize that when aQDs are applied to the pulmonary microcirculation, they trigger an immune response in both the endothelium and marginated neutrophils, leading to increased neutrophil recruitment from the circulating blood. Our findings shows that this immune response likely involves upregulation of relevant selectins and integrins on both endothelial cells and neutrophils, which, in turn, slows down the crawling velocity of neutrophils. By examining their crawling velocities, we can better comprehend how neutrophils navigate through the microvasculature in response to various stimuli or conditions. Referring to the function of selectins and integrins on neutrophil recruitment and crawling velocity, we will state these below.

4.5 Initiation of acute inflammatory response triggered by aQDs and associated inflammatory products

4.5.1 Cytokines and chemokines mediate the recruitment of neutrophils

Acute pulmonary inflammation can be induced by various cytokines and chemokines， which play crucial roles in initiating and regulating the inflammatory response in the lungs. Among these cytokines, IL-1, IL-6, TNF-α are particularly important in facilitating neutrophil recruitment. IL-1 and TNF-α have been shown to enhance the expression of adhesion molecules such as E-selectin and ICAM-1 on endothelial cells, promoting neutrophil recruitment to the site of inflammation by facilitating adhesion to the pulmonary vascular endothelium (Ward 2003). On the other hand, IL-6 plays a role in upregulating C5a receptor on vascular endothelium to accumulate more C5a. C5a is a potent complement activation product that can produce various proinflammatory mediators, attracting polymorphonuclear neutrophils to the sites of inflammation or injury (Ward 2003; Dudeck et al.

2021). Polymorphic membrane proteins of C. pneumoniae were also proved to induce IL-6 and monocyte chemoattractant protein (MCP) -1 in human endothelial cells by activating the NFkB pathway (Niessner et al. 2003). When inflammation occurs, the regulatory mechanism responds, especially IL-10, which exerts anti-inflammatory effects (Ward 2003). IL-10 exerts its influence through autocrine or paracrine signaling, regulating the inflammatory response locally, while also demonstrating endocrine effects by modulating inflammation at the systemic level (Stenvinkel et al. 2005). Our results showed a trend of increased IL-6 concentration and a significant elevation of IL-10 concentration in the circulating system following aQDs application for 1 h. While there was a significant increase in IL-6 levels in LPS-treated group. These findings suggest that aQDs may have an impact on the regulation of pro-inflammatory cytokines, such as IL-6, as well as anti-inflammatory cytokines, like IL-10, in the systemic circulation. It is interesting to note that the response to aQDs in terms of cytokine secretion may be dose-dependent, as indicated by the study by Borgognoni et al., where high doses of TiO_2 triggered human microphages to release both IL-6 and IL-10, while low doses only resulted in IL-6 secretion (Borgognoni et al. 2015). Similarly, in our study, the low dose of LPS used may have only led to the observation of increased IL-6 levels in the systemic circulation in the LPS-treated group. The finding that aQDs can trigger the production of both pro-inflammatory and anti-inflammatory cytokines in the systemic circulation highlights the complex nature of the immune response to NPs. It is known that NPs can interact with immune cells and elicit a variety of responses depending on their properties, dose, and route of exposure. The production of both IL-6 and IL-10 suggests a possible regulatory mechanism where the immune system tries to balance pro-inflammatory and anti-inflammatory responses to maintain immune homeostasis.

In addition, we also observed an increase in CCL3 and CCL22 levels after aQDs application. Chemokines are a family of small proteins that can be classified into different subfamilies, including C, CC, CXC, and CX3C chemokines. These chemokines play important roles in immune responses by activating various immune cells, such as neutrophils, monocytes, macrophages, and lymphocytes. MIP-1a/CCL3 and MIP-1b/CCL4 are chemotactic and proinflammatory regulators expressed by lymphocytes, monocytes and macrophages (Maurer and von Stebut 2004). CCL3 is known to mediate neutrophil recruitment in response to

inflammatory stimuli, depending on TNF-α pathway, which is also a proinflammation cytokine produced by various cells, including macrophages, lymphocytes, and endothelial cells (Ramos et al. 2005; Reichel et al. 2009). The increase in CCL3 levels after aQDs application could indicate the activation of these immune cells and their involvement in the recruitment of other immune cells, such as neutrophils, to the site of aQDs exposure. MDC/CCL22 is a proinflammatory chemoattractant for CCR4-expressing Th2 lymphocytes, monocytes-derived dendritic cells, and natural killer cells, and it is known to regulate pulmonary levels of MIP-2 and MIP-1 (Richter et al. 2014). Like CCL3, CCL22 is produced by immune cells in response to inflammatory signals. The increase in CCL22 levels after aQDs application could suggest the recruitment of specific immune cell subsets that are attracted by this chemokine. Together, the increase in CCL3 and CCL22 levels after aQDs application supports the idea that aQDs interact with immune cells in the bloodstream, leading to the release of proinflammatory factors and subsequent recruitment of immune cells, including neutrophils, to the site of aQDs exposure.

4.5.2 Selectins and integrins mediate aQDs induced neutrophil recruitment in microvessels

Unlike neutrophils in vessels of other organs, which are typically 6-10 μm in diameter, neutrophils in the pulmonary microvessels, with diameters ranging from 2-15 μm, need to undergo deformation to pass through (Grommes and Soehnlein 2011). Therefore, neutrophil recruitment in the pulmonary microcirculation primarily encompasses tethering, adhesion, crawling and transmigration. The onset of neutrophil recruitment is mediated by multiple selectins and integrins. The selectin family includes E-selectin, which is expressed on endothelial cells, P-selectin, expressed on activated endothelium and platelets, and L-selectin, expressed on leukocytes. The necessity of these selectins in the lung is dependent on the distinct inflammatory stimulus (Grommes and Soehnlein 2011). In the study by Mizgerd et al. (Mizgerd et al. 1996), it was observed that inhibiting of E-, P-, and L-selectins did not have an impact on the flux of neutrophils transmigrating into the alveolar space following stimulation with S. pneumoniae and LPS. However, other studies have presented partly contrasting viewpoints. For instance, in the

zymosan-induced peritonitis model and the LPS-induced lung inflammation model, blocking P-selectin did not affect neutrophil migration. On the other hand, in the LPS-induced lung inflammation model, blockage of E-selectin showed an effect, while it was ineffective in the zymosan-induced peritonitis model. Additionally, L-selectin was found to reduce neutrophil migration in both inflammation models (Kornerup et al., 2010). The expression of E-selectin and LFA-1 mediates the deceleration of leukocyte velocity for firm adhesion and rolling during inflammation (Zarbock et al. 2011). These divergent findings highlight the complexity of selectin-mediated neutrophil migration and indicate potential variations depending on the specific inflammatory stimuli and experimental models employed. In our study, we observed that inhibiting E-selectin by application of neutralizing mAbs effectively reduced the recruitment of neutrophils and survived the reduced velocity of crawling neutrophils induced by aQDs in the pulmonary microcirculation. However, the blockage of P-selectin did not exhibit a similar impact, and the blockade of L-selectin did not work. Taken together, these results suggest that E-selectin plays a specific role in the recruitment of neutrophils in response to aQDs, while L-selectin and P-selectin may not be involved in this particular process.

Neutrophils crawling under shear conditions need to maintain continuous adhesion to the endothelial surface while navigating through the microvessels. During this process, they release some of the existing adhesive bonds as they move forward and form new bonds in other regions of the cell, allowing them to securely adhere to the endothelium while undergoing crawling motion (Kolaczkowska and Kubes 2013). In this process, the integrins LFA-1 and MAC-1 play crucial roles in neutrophil adhesion and crawling (Ley et al. 2007; Li et al. 2018). Henderson et al. firstly emphasized the role of LFA-1 in the stabilization of the transient or tethering phase of neutrophil rolling, thereby contributing to neutrophil rolling on the mesenteric vascular bed by IVM. On the other hand, the presence of MAC-1 is not essential for either rolling or firm adhesion, but rather exhibits distinctive properties in facilitating emigration from the vessel (Henderson et al. 2001). Philipson et al. investigated neutrophil adhesion and crawling in postcapillary venules in response to MIP-2 and TNF-α. The study found that neutrophil adhesion was primarily dependent on the integrin LFA-1, while crawling was mainly dependent on the integrin MAC-1. Interestingly, when LFA-1-deficient neutrophils were ex-

amined, only a few neutrophils adhered to the endothelium with similar displacement and velocity compared to the control group. On the other hand, MAC-1-deficient neutrophils were able to adhere to the endothelium, but their velocity was significantly reduced by 95% and their displacement was reduced by 10-fold compared to the control group (Phillipson et al. 2006). Also, Sumagin et al. studied the distinct functions of LFA-1 and MAC-1 in the movement patterns of neutrophils and monocytes in the cremaster muscle using IVM. They found that MAC-1, not LFA-1, is essential for neutrophil crawling under both unstimulated and TNF-α activated conditions, as well as for transmigration during inflammation. However, in the absence of MAC-1, neutrophils can still crawl in the venules, and the intralumenal crawling distance is typically longer than in MAC-1 mediated crawling (Sumagin et al. 2010). These findings highlight the distinct contributions of LFA-1 and MAC-1 in the adhesion and crawling processes of neutrophils during inflammation. As shown in our study, we observed that blocking LFA-1 effectively inhibited the neutrophil recruitment elicited by aQDs, whereas blocking MAC-1 did not have the same effect. However, the blockage of LFA-1 and MAC-1 can partially abolish the reduced crawling velocity induced by aQDs. The disruption of adhesive interactions between neutrophils and endothelial cells by inhibiting LFA-1 and MAC-1 led to a reduction in neutrophil adhesion and crawling behavior. As a result, neutrophils may regain some of their steady-state velocities. However, it's important to note that the restoration of crawling velocity may not fully reach the control levels. This could be due to several reasons, such as residual effects of aQDs on neutrophils, incomplete inhibition of LFA-1 and MAC-1, or involvement of other factors that contribute to the altered neutrophil behavior.

4.6 Impaired pulmonary perfusion due to NP-induced inflammation in the pulmonary microcirculation

Blood flow velocity is inversely proportional to the total cross-sectional area of the blood vessels. Large cross-sectional areas result in decreased flow velocity. Capillaries, with their extensive total cross-sectional area, have the slowest blood flow, allowing for efficient exchange of gases and nutrients (Matienzo and Bordoni 2023). In the lungs, there is a dense network of capillaries, hosting a significantly

higher number of neutrophils (50-fold) compared to other blood vessel systems. This collection of neutrophils is known as the marginated pool. In pulmonary capillaries, the transit time of neutrophils is prolonged compared to other organs, primarily due to their deformation to pass through the narrow capillary openings (Wiggs et al., 1994; Kuebler and Goetz, 2002; Burns, Smith, and Walker, 2003). Leukocyte sequestration in the lungs is associated with decreased pulmonary microvascular flow velocity (Waisman et al. 2006). In a study conducted by Ueki et al., they utilized 1-μm fluorescence beads injected intravenously to evaluate the blood velocity in mice by employing L-IVM. The control baseline blood velocity was reported to be 150 μm/s. They observed that pulmonary perfusion in mice infected with influenza viruses was reduced at day 2 of infection and remained consistently low thereafter. They concluded in the paper that inflammation caused by the influenza virus can impact the blood velocity in the pulmonary microcirculation (Ueki et al. 2018). Park et al. introduced the concept of the functional capillary ratio (FCR) to evaluate the proportion of functional microvasculature and dead space in the pulmonary microcirculation. They found neutrophils were the main hindrance in the pulmonary microcirculation during sepsis, while reversed FCR in the pulmonary microcirculation was resulted from depleting neutrophils (Park et al. 2019). Taken together, these studies suggest that neutrophils contribute significantly to the impaired blood flow and gas exchange in sepsis.

In our study, we investigated the effects of QDs on neutrophil recruitment and pulmonary microcirculation perfusion. As discussed above, we observed an inflammatory response and a reduction of microcirculation perfusion in the aQDs group under healthy conditions. By blocking TNF-α, LFA-1, and using a P2X7R antagonist, we were able to reverse the reduced blood flow velocity induced by aQDs. As this recovery of blood flow velocity coincided with the prevention of neutrophil adhesion and a similar reduction in blood flow velocity observed in the LPS-induced injury condition with neutrophil accumulation in the microvessels, these findings suggest that neutrophil recruitment plays a crucial role in modulating pulmonary microcirculation perfusion. Further research in this area may contribute to the development of therapeutic strategies targeting neutrophil recruitment to improve microcirculatory function in various pathological conditions.

4.7 eATP-mediated neutrophil recruitment in response to NPs

The cellular response to NPs, such as amino-modified NPs, can exhibit a dose-dependent pattern. Higher doses of NPs may cause cell death through mechanisms like oxidative stress, inflammation, and membrane damage, while even low doses can disrupt cell cycle and impair cellular functions. The release of toxic ions, ROS, and lysosomal alterations induced from NPs can cause extensive cellular damage and ultimately cell death (Kim et al. 2013; Anguissola et al. 2014; Deville et al. 2020). The immune system can be activated by DAMPs released from injured or damaged tissue. These DAMPs serve as signals, stimulating various sentinel cells like mast cells, macrophages, and dendritic cells. This activation sets off a cascade of events within the immune system. One of the initial responses to this activation is the recruitment of leukocytes, particularly neutrophils, to the site of inflammation (Tang et al. 2012; Maas, Soehnlein, and Viola 2018). eATP has been regarded as a DAMP in response to stress, serveing as a signal to recruit inflammatory cells to the site of injury. The accumulation of eATP in the inflammatory site involves the contribution of multiple cell types. Membrane deformation of neutrophils induced the release of ATP. When neutrophils were stimulated by the chemoattractant FMLP, ATP was released to the peak after 5 min and returned to basal levels after 15 min (Chen, Corriden, et al. 2006). eATP, as an extracellular signaling molecule, further contributes to the recruitment and activation of immune cells in the inflammatory response. During inflammation induced by LPS, there is a peak in eATP levels in the BAL, which coincides with the maximum migration of neutrophils into the alveolar space. Interestingly, blocking eATP production has been shown to limit vascular leakage associated with inflammation. This suggests that eATP plays a role in promoting neutrophil migration during the inflammatory response (Shah et al. 2014).

P2X7R, an ATP-gated cation channel, is expressed on various inflammatory cells (Tran et al. 2010). Gene expression data from our laboratory revealed the presence of P2X7R expression on capillary endothelial cells, monocytes, macrophages, and lymphocytes during pulmonary pathological conditions (Personal communication of unpublished results from Lianyong Han and Tobias Stöger). At low concentrations, eATP activates P2X7R, leading to the opening of channels for sodium (Na^+), potassium (K^+), and calcium ions (Ca^{2+}). This results in the re-

lease of K^+ outside the cell and flux of Na^+ and Ca^{2+} into the intracellular environment. On the other hand, high concentrations of eATP make a non-selective pore, ultimately leading to cell death. The activation of P2X7R and subsequent ion flux trigger various cellular responses, including inflammation and immune responses (Janks, Sprague, and Egan 2019; Rotondo et al. 2022). This receptor has been reported to control a variety of pro-inflammatory cellular signals based on its ability to initiate post-translational cytokine processing. Furthermore, P2X7R is essential for neutrophil recruitment (Riteau et al. 2010; da Silva et al. 2013; Di Virgilio et al. 2017).

In our study, we observed that the application of a P2X7R antagonist inhibited neutrophil recruitment, consistent with previous reports. We speculate that the disruption of the ATP-gated cation mechanism by the P2X7R antagonist indeed leads to a reduction in ion flux, which may have implications for neutrophil recruitment. Neutrophils rely on ion flux and ATP signaling to navigate and respond to inflammatory stimuli. By inhibiting P2X7R, the antagonist interferes with the normal cellular responses to eATP, potentially modulating neutrophil behavior, including crawling and transmigration. As a result, neutrophils may no longer need to engage in excessive crawling behavior, leading to the observed reversal in the crawling velocity induced by aQDs. The reduced ion flux may alter the signals that dictate neutrophil migration and positioning, ultimately affecting their recruitment to the site of inflammation. This finding suggests that the P2X7R antagonist has the potential to influence neutrophil motility and their involvement in the inflammatory response triggered by aQDs.

5. Conclusion

1. In vitro experiments reveal that cQDs are taken up more efficiently by HUVEC compared to aQDs. In vivo experiments demonstrate that intravenously applied cQDs interact with endothelial cells and might be taken up by them. In contrast, aQDs tend to form clusters in pulmonary vessels over time and induce stronger inflammation compared to cQDs, indicating that the PEG modification of QDs does not fully protect against their potential effects in the pulmonary microcirculation.

2. Under physiological conditions, i.v. injection of aQDs induces neutrophil recruitment, but it does not significantly alter immune responses under pathological conditions, such as LPS-induced acute inflammation and Bleomycin-induced fibrosis.

3. The initiation of neutrophil recruitment induced by aQDs requires cellular degranulation and release of TNF-α. Moreover, the neutrophil response to aQDs appears to involve the release of DAMPs, particularly eATP. This process also involves the upregulation of relevant selectins (such as E-selectin) and the involvement of integrins (such as LFA-1 and MAC-1) on endothelial cells and neutrophils. These, in turn, result in a slowdown of the crawling velocity of neutrophils on the vascular surface. The blockage of selectins and integrins or the use of an eATP antagonist prevents recruitment of neutrophils and partially restores their reduced crawling velocity.

4. The accumulation and retention of neutrophils in the pulmonary microcirculation result in a decrease in local blood flow velocity. Accordingly, when factors involved in neutrophil recruitment, such as cellular degranulation, DAMPs, and TNF-α release, as well as the upregulation of selectins and integrins, are diminished, blood perfusion could be restored to baseline levels.

6. References

1. André, E., T. Stoeger, S. Takenaka, M. Bahnweg, B. Ritter, E. Karg, B. Lentner, C. Reinhard, H. Schulz, and M. Wjst. 2006. "Inhalation of Ultrafine Carbon Particles Triggers Biphasic Pro-Inflammatory Response in the Mouse Lung." The European Respiratory Journal 28 (2): 275–85. https://doi.org/10.1183/09031936.06.00071205.
2. Ali, Hassan, Ashrafullah Khan, Jawad Ali, Hadayat Ullah, Adnan Khan, Hussain Ali, Nadeem Irshad, and Salman Khan. 2020. "Attenuation of LPS-Induced Acute Lung Injury by Continentalic Acid in Rodents through Inhibition of Inflammatory Mediators Correlates with Increased Nrf2 Protein Expression." *BMC Pharmacology and Toxicology* 21 (1): 81. https://doi.org/10.1186/s40360-020-00458-7.
3. Alessandrini, Francesca, Holger Schulz, Shinji Takenaka, Bernd Lentner, Erwin Karg, Heidrun Behrendt, and Thilo Jakob. 2006. "Effects of Ultrafine Carbon Particle Inhalation on Allergic Inflammation of the Lung." The Journal of Allergy and Clinical Immunology 117 (4): 824–30. https://doi.org/10.1016/j.jaci.2005.11.046.
4. Anguissola, Sergio, David Garry, Anna Salvati, Peter J. O'Brien, and Kenneth A. Dawson. 2014. "High Content Analysis Provides Mechanistic Insights on the Pathways of Toxicity Induced by Amine-Modified Polystyrene Nanoparticles." *PloS One* 9 (9): e108025. https://doi.org/10.1371/journal.pone.0108025.
5. Arganda-Carreras, Ignacio, Carlos O. S. Sorzano, Roberto Marabini, José María Carazo, Carlos Ortiz-de-Solorzano, and Jan Kybic. 2006. "Consistent and Elastic Registration of Histological Sections Using Vector-Spline Regularization." In Computer Vision Approaches to Medical Image Analysis, edited by Reinhard R. Beichel and Milan Sonka, 85–95. Lecture Notes in Computer Science. Berlin, Heidelberg: Springer. https://doi.org/10.1007/11889762_8.
6. Auffray, Cedric, Darin Fogg, Meriem Garfa, Gaelle Elain, Olivier Join-Lambert, Samer Kayal, Sabine Sarnacki, Ana Cumano, Gregoire Lauvau, and Frederic Geissmann. 2007. "Monitoring of Blood Vessels and Tissues by a Population of Monocytes with Patrolling Behavior." *Science (New York, N.Y.)* 317 (5838): 666–70. https://doi.org/10.1126/science.1142883.
7. Baranov, Maksim V., Manoj Kumar, Stefano Sacanna, Shashi Thutupalli, and Geert van den Bogaart. 2021. "Modulation of Immune Responses by Particle Size and Shape." *Frontiers in Immunology* 11. https://www.frontiersin.org/articles/10.3389/fimmu.2020.607945.
8. Bankova, L. G., D. F. Dwyer, A. Y. Liu, K. F. Austen, and M. F. Gurish. 2015. "Maturation of Mast Cell Progenitors to Mucosal Mast Cells during Allergic Pulmonary Inflammation in Mice." *Mucosal Immunology* 8 (3): 596–606. https://doi.org/10.1038/mi.2014.91.

9. Begandt, Daniela, Sarah Thome, Markus Sperandio, and Barbara Walzog. 2017. “How Neutrophils Resist Shear Stress at Blood Vessel Walls: Molecular Mechanisms, Subcellular Structures, and Cell–Cell Interactions.” *Journal of Leukocyte Biology* 102 (3): 699–709. https://doi.org/10.1189/jlb.3MR0117-026RR.
10. Borgognoni, Camila F., Michael Mormann, Ying Qu, Marcus Schäfer, Klaus Langer, Cengiz Öztürk, Sylvia Wagner, et al. 2015. “Reaction of Human Macrophages on Protein Corona Covered TiO2 Nanoparticles.” *Nanomedicine: Nanotechnology, Biology and Medicine* 11 (2): 275–82. https://doi.org/10.1016/j.nano.2014.10.001.
11. Buzea, Cristina, Ivan I. Pacheco, and Kevin Robbie. 2007. “Nanomaterials and Nanoparticles: Sources and Toxicity.” *Biointerphases* 2 (4): MR17–71. https://doi.org/10.1116/1.2815690.
12. Burns, Alan R., C. Wayne Smith, and David C. Walker. 2003. “Unique Structural Features That Influence Neutrophil Emigration Into the Lung.” *Physiological Reviews* 83 (2): 309–36. https://doi.org/10.1152/physrev.00023.2002.
13. Chen, Huei-Wen, Sheng-Fang Su, Chiang-Ting Chien, Wei-Hsiang Lin, Sung-Liang Yu, Cheng-Chung Chou, Jeremy J. W. Chen, and Pan-Chyr Yang. 2006. “Titanium Dioxide Nanoparticles Induce Emphysema-like Lung Injury in Mice.” *FASEB Journal: Official Publication of the Federation of American Societies for Experimental Biology* 20 (13): 2393–95. https://doi.org/10.1096/fj.06-6485fje.
14. Chen, Ross Corriden, Yoshiaki Inoue, Linda Yip, Naoyuki Hashiguchi, Annelies Zinkernagel, Victor Nizet, Paul A. Insel, and Wolfgang G. Junger. 2006. “ATP Release Guides Neutrophil Chemotaxis via P2Y2 and A3 Receptors.” *Science (New York, N.Y.)* 314 (5806): 1792–95. https://doi.org/10.1126/science.1132559.
15. Chrysanthopoulou, Akrivi, Ioannis Mitroulis, Eirini Apostolidou, Stella Arelaki, Dimitrios Mikroulis, Theocharis Konstantinidis, Efthimios Sivridis, et al. 2014. “Neutrophil Extracellular Traps Promote Differentiation and Function of Fibroblasts.” *The Journal of Pathology* 233 (3): 294–307. https://doi.org/10.1002/path.4359.
16. Crooks, Michael G., Ahmed Fahim, Khalid M. Naseem, Alyn H. Morice, and Simon P. Hart. 2014. “Increased Platelet Reactivity in Idiopathic Pulmonary Fibrosis Is Mediated by a Plasma Factor.” *PLoS ONE* 9 (10): e111347. https://doi.org/10.1371/journal.pone.0111347.
17. da Silva, Nathalia D. M. Sperotto, Thiago J. Borges, Cristina Bonorino, Cristina M. Takyia, Robson Coutinho-Silva, Maria M. Campos, Rafael F. Zanin, and Fernanda B. Morrone. 2013. “P2X7 Receptor Is Required for Neutrophil Accumulation in a Mouse Model of Irritant Contact Dermatitis.” *Experimental Dermatology* 22 (3): 184–88. https://doi.org/10.1111/exd.12094.
18. Detampel, Pascal, Anutosh Ganguly, Sara Tehranian, Francis Green, Santiswarup Singha, Pere Santamaria, Ayodeji A. Jeje, Clifford S. Cho, Björn Petri, and Matthias W. Amrein. 2019. “In Vivo Clearance of Nanoparticles by Transcytosis across Alveolar Epithelial Cells.” *PLoS ONE* 14 (9): e0223339. https://doi.org/10.1371/journal.pone.0223339.

19. Deng, Zicheng, Gregory T. Kalin, Donglu Shi, and Vladimir V. Kalinichenko. 2021. “Nanoparticle Delivery Systems with Cell-Specific Targeting for Pulmonary Diseases.” *American Journal of Respiratory Cell and Molecular Biology* 64 (3): 292–307. https://doi.org/10.1165/rcmb.2020-0306TR.
20. De Filippo, Katia, Anne Dudeck, Mike Hasenberg, Emma Nye, Nico van Rooijen, Karin Hartmann, Matthias Gunzer, Axel Roers, and Nancy Hogg. 2013. “Mast Cell and Macrophage Chemokines CXCL1/CXCL2 Control the Early Stage of Neutrophil Recruitment during Tissue Inflammation.” *Blood* 121 (24): 4930–37. https://doi.org/10.1182/blood-2013-02-486217.
21. Deville, Sarah, Birgit Honrath, Quynh T. D. Tran, Gyorgy Fejer, Ivo Lambrichts, Inge Nelissen, Amalia M. Dolga, and Anna Salvati. 2020. “Time-Resolved Characterization of the Mechanisms of Toxicity Induced by Silica and Amino-Modified Polystyrene on Alveolar-like Macrophages.” *Archives of Toxicology* 94 (1): 173–86. https://doi.org/10.1007/s00204-019-02604-5.
22. Di Virgilio, Francesco, Diego Dal Ben, Alba Clara Sarti, Anna Lisa Giuliani, and Simonetta Falzoni. 2017. “The P2X7 Receptor in Infection and Inflammation.” *Immunity* 47 (1): 15–31. https://doi.org/10.1016/j.immuni.2017.06.020.
23. Doerschuk, C. M., N. Beyers, H. O. Coxson, B. Wiggs, and J. C. Hogg. 1993. “Comparison of Neutrophil and Capillary Diameters and Their Relation to Neutrophil Sequestration in the Lung.” *Journal of Applied Physiology* 74 (6): 3040–45. https://doi.org/10.1152/jappl.1993.74.6.3040.
24. Doerschuk, Claire M. 2000. “Leukocyte Trafficking in Alveoli and Airway Passages.” *Respiratory Research* 1 (3): 136–40. https://doi.org/10.1186/rr24.
25. Domscheit, Hannes, Maria A. Hegeman, Niedja Carvalho, and Peter M. Spieth. 2020. “Molecular Dynamics of Lipopolysaccharide-Induced Lung Injury in Rodents.” *Frontiers in Physiology* 11. https://www.frontiersin.org/articles/10.3389/fphys.2020.00036.
26. Donaldson, Ken, and Craig A. Poland. 2012. “Inhaled Nanoparticles and Lung Cancer - What We Can Learn from Conventional Particle Toxicology.” *Swiss Medical Weekly* 142: w13547. https://doi.org/10.4414/smw.2012.13547.
27. Dudeck, Jan, Johanna Kotrba, Roland Immler, Aaron Hoffmann, Martin Voss, Vasileia Ismini Alexaki, Lorena Morton, et al. 2021. “Directional Mast Cell Degranulation of Tumor Necrosis Factor into Blood Vessels Primes Neutrophil Extravasation.” *Immunity* 54 (3): 468-483.e5. https://doi.org/10.1016/j.immuni.2020.12.017.
28. Elsabahy, Mahmoud, and Karen L. Wooley. 2013. “Cytokines as Biomarkers of Nanoparticle Immunotoxicity.” *Chemical Society Reviews* 42 (12): 5552–76. https://doi.org/10.1039/c3cs60064e.
29. Ershov, D., Phan, MS., Pylvänäinen, J.W., Rigaud S.U., et al. TrackMate 7: integrating state-of-the-art segmentation algorithms into tracking pipelines. Nat Methods (2022). https://doi.org/10.1038/s41592-022-01507-1

30. *European Commission*. 2022. https://eur-lex.europa.eu/legal-content/EN/TXT/?uri=CELEX%3A32022H0614%2801%29.
31. Fromen, Catherine A., William J. Kelley, Margaret B. Fish, Reheman Adili, Jeffery Noble, Mark J. Hoenerhoff, Michael Holinstat, and Omolola Eniola-Adefeso. 2017. "Neutrophil–Particle Interactions in Blood Circulation Drive Particle Clearance and Alter Neutrophil Responses in Acute Inflammation." *ACS Nano* 11 (11): 10797–807. https://doi.org/10.1021/acsnano.7b03190.
32. Fu, Jie, Jennifer Fiegel, Eric Krauland, and Justin Hanes. 2002. "New Polymeric Carriers for Controlled Drug Delivery Following Inhalation or Injection." Biomaterials, Injectable Polymeric Biomaterials, 23 (22): 4425–33. https://doi.org/10.1016/S0142-9612(02)00182-5.
33. Ganter, Michael T., Jérémie Roux, Byron Miyazawa, Marybeth Howard, James A. Frank, George Su, Dean Sheppard, et al. 2008. "Interleukin-1beta Causes Acute Lung Injury via Alphavbeta5 and Alphavbeta6 Integrin-Dependent Mechanisms." *Circulation Research* 102 (7): 804–12. https://doi.org/10.1161/CIRCRESAHA.107.161067.
34. Ganguly, Koustav, Dariusch Ettehadieh, Swapna Upadhyay, Shinji Takenaka, Thure Adler, Erwin Karg, Fritz Krombach, et al. 2017. "Early Pulmonary Response Is Critical for Extra-Pulmonary Carbon Nanoparticle Mediated Effects: Comparison of Inhalation versus Intra-Arterial Infusion Exposures in Mice." *Particle and Fibre Toxicology* 14 (1): 19. https://doi.org/10.1186/s12989-017-0200-x.
35. Gazendam, Roel P., John L. van Hamme, Anton T. J. Tool, Mark Hoogenboezem, J. Merlijn van den Berg, Jan M. Prins, Ljubomir Vitkov, et al. 2016. "Human Neutrophils Use Different Mechanisms to Kill Aspergillus Fumigatus Conidia and Hyphae: Evidence from Phagocyte Defects." *Journal of Immunology (Baltimore, Md.: 1950)* 196 (3): 1272–83. https://doi.org/10.4049/jimmunol.1501811.
36. Geiser, Marianne, Tobias Stoeger, Marco Casaulta, Shanze Chen, Manuela Semmler-Behnke, Ines Bolle, Shinji Takenaka, Wolfgang G. Kreyling, and Holger Schulz. 2014. "Biokinetics of Nanoparticles and Susceptibility to Particulate Exposure in a Murine Model of Cystic Fibrosis." Particle and Fibre Toxicology 11 (April): 19. https://doi.org/10.1186/1743-8977-11-19.
37. Geys, Jorina, Abderrahim Nemmar, Erik Verbeken, Erik Smolders, Monica Ratoi, Marc F. Hoylaerts, Benoit Nemery, and Peter H.M. Hoet. 2008. "Acute Toxicity and Prothrombotic Effects of Quantum Dots: Impact of Surface Charge." *Environmental Health Perspectives* 116 (12): 1607–13. https://doi.org/10.1289/ehp.11566.
38. Granton, Elise, Jung Hwan Kim, John Podstawka, and Bryan G. Yipp. 2018. "The Lung Microvasculature Is a Functional Immune Niche." *Trends in Immunology* 39 (11): 890–99. https://doi.org/10.1016/j.it.2018.09.002.

Greenland, John R., Xiang Xu, David M. Sayah, Feng Chun Liu, Kirk D. Jones, Mark R. Looney, and George H. Caughey. 2014. "Mast Cells in a Murine Lung Ischemia-Reperfusion

Model of Primary Graft Dysfunction." *Respiratory Research* 15 (1): 95. https://doi.org/10.1186/s12931-014-0095-0

39. Grommes, Jochen, and Oliver Soehnlein. 2011. "Contribution of Neutrophils to Acute Lung Injury." *Molecular Medicine* 17 (3–4): 293–307. https://doi.org/10.2119/molmed.2010.00138.
40. Guo, Ren-Feng, and Peter A. Ward. 2002. "Mediators and Regulation of Neutrophil Accumulation in Inflammatory Responses in Lung: Insights from the IgG Immune Complex Model." *Free Radical Biology & Medicine* 33 (3): 303–10. https://doi.org/10.1016/s0891-5849(02)00823-7.
41. Guo, Tao, Qiuyu Tang, Yating Guo, Honglong Qiu, Jing Dai, Chao Xing, Shihao Zhuang, and Guoming Huang. 2021. "Boron Quantum Dots for Photoacoustic Imaging-Guided Photothermal Therapy." *ACS Applied Materials & Interfaces* 13 (1): 306–11. https://doi.org/10.1021/acsami.0c21198.
42. Han, Xiangjun, Ke Xu, Olena Taratula, and Khashayar Farsad. 2019. "Applications of Nanoparticles in Biomedical Imaging." *Nanoscale* 11 (3): 799–819. https://doi.org/10.1039/c8nr07769j.
43. Harris, J. Milton, and Robert B. Chess. 2003. "Effect of Pegylation on Pharmaceuticals." *Nature Reviews Drug Discovery* 2 (3): 214–21. https://doi.org/10.1038/nrd1033.
44. Hay, J., S. Shahzeidi, and G. Laurent. 1991. "Mechanisms of Bleomycin-Induced Lung Damage." *Archives of Toxicology* 65 (2): 81–94. https://doi.org/10.1007/BF02034932.
45. Haber, Shimon, Alys Clark, and Merryn Tawhai. 2013. "Blood Flow in Capillaries of the Human Lung." *Journal of Biomechanical Engineering* 135 (10): 101006. https://doi.org/10.1115/1.4025092.
46. Headley, Mark B., Adriaan Bins, Alyssa Nip, Edward W. Roberts, Mark R. Looney, Audrey Gerard, and Matthew F. Krummel. 2016. "Visualization of Immediate Immune Responses to Pioneer Metastatic Cells in the Lung." *Nature* 531 (7595): 513–17. https://doi.org/10.1038/nature16985.
47. Heires, Marcel. 2008. "The International Organization for Standardization (ISO)." *New Political Economy* 13 (3): 357–67. https://doi.org/10.1080/13563460802302693.
48. Hellewell, P. G., P. M. Henson, G. P. Downey, and G. S. Worthen. 1991. "Control of Local Blood Flow in Pulmonary Inflammation: Role for Neutrophils, PAF, and Thromboxane." *Journal of Applied Physiology (Bethesda, Md.: 1985)* 70 (3): 1184–93. https://doi.org/10.1152/jappl.1991.70.3.1184.
49. Henderson, R. B., L. H. Lim, P. A. Tessier, F. N. Gavins, M. Mathies, M. Perretti, and N. Hogg. 2001. "The Use of Lymphocyte Function-Associated Antigen (LFA)-1-Deficient Mice to Determine the Role of LFA-1, Mac-1, and Alpha4 Integrin in the Inflammatory Response of Neutrophils." *The Journal of Experimental Medicine* 194 (2): 219–26. https://doi.org/10.1084/jem.194.2.219.
50. Ho, Chia-Chi, Han Chang, Hui-Ti Tsai, Ming-Hsien Tsai, Chung-Shi Yang, Yong-Chien Ling, and Pinpin Lin. 2013. "Quantum Dot 705, a Cadmium-Based Nanoparticle, Induces Persistent

Inflammation and Granuloma Formation in the Mouse Lung." *Nanotoxicology* 7 (1): 105–15. https://doi.org/10.3109/17435390.2011.635814.

51. Holian, A., R. Hamilton, and R. K. Scheule. 1991. "Mechanistic Aspects of Cromolyn Sodium Action on the Alveolar Macrophage: Inhibition of Stimulation by Soluble Agonists." *Agents and Actions* 33 (3–4): 318–25. https://doi.org/10.1007/BF01986580.
52. Immler, Roland, Scott I. Simon, and Markus Sperandio. 2018. "Calcium Signaling and Related Ion Channels in Neutrophil Recruitment and Function." *European Journal of Clinical Investigation* 48 (Suppl 2): e12964. https://doi.org/10.1111/eci.12964.
53. Immler, Roland, Wiebke Nadolni, Annika Bertsch, Vasilios Morikis, Ina Rohwedder, Sergi Masgrau-Alsina, Tobias Schroll, et al. 2022. "The Voltage-Gated Potassium Channel KV1.3 Regulates Neutrophil Recruitment during Inflammation." *Cardiovascular Research* 118 (5): 1289–1302. https://doi.org/10.1093/cvr/cvab133.
54. Inoue, K., H. Takano, R. Yanagisawa, M. Sakurai, S. Abe, S. Yoshino, K. Yamaki, and T. Yoshikawa. 2007. "Effects of Nanoparticles on Lung Physiology in the Presence or Absence of Antigen." *International Journal of Immunopathology and Pharmacology* 20 (4): 737–44. https://doi.org/10.1177/039463200702000409.
55. Inoue, Ken-ichiro, Eiko Koike, Rie Yanagisawa, Seishiro Hirano, Masataka Nishikawa, and Hirohisa Takano. 2009. "Effects of Multi-Walled Carbon Nanotubes on a Murine Allergic Airway Inflammation Model." *Toxicology and Applied Pharmacology* 237 (3): 306–16. https://doi.org/10.1016/j.taap.2009.04.003.
56. Inoue, Ken-ichiro, Hirohisa Takano, Rie Yanagisawa, Miho Sakurai, Takamichi Ichinose, Kaori Sadakane, and Toshikazu Yoshikawa. 2005. "Effects of Nano Particles on Antigen-Related Airway Inflammation in Mice." *Respiratory Research* 6 (1): 106. https://doi.org/10.1186/1465-9921-6-106.
57. Inoue, Ken-ichiro, Hirohisa Takano, Rie Yanagisawa, Seishiro Hirano, Miho Sakurai, Akinori Shimada, and Toshikazu Yoshikawa. 2006. "Effects of Airway Exposure to Nanoparticles on Lung Inflammation Induced by Bacterial Endotoxin in Mice." *Environmental Health Perspectives* 114 (9): 1325–30. https://doi.org/10.1289/ehp.8903.
58. Inoue, Ken-Ichiro, Rie Yanagisawa, Eiko Koike, Masataka Nishikawa, and Hirohisa Takano. 2010. "Repeated Pulmonary Exposure to Single-Walled Carbon Nanotubes Exacerbates Allergic Inflammation of the Airway: Possible Role of Oxidative Stress." *Free Radical Biology & Medicine* 48 (7): 924–34. https://doi.org/10.1016/j.freeradbiomed.2010.01.013.
59. Janks, Laura, Randy S. Sprague, and Terrance M. Egan. 2019. "ATP-Gated P2X7 Receptors Require Chloride Channels to Promote Inflammation in Human Macrophages." *Journal of Immunology (Baltimore, Md. 1950)* 202 (3): 883–98. https://doi.org/10.4049/jimmunol.1801101.
60. Jacobsen, Nicklas Raun, Peter Møller, Keld Alstrup Jensen, Ulla Vogel, Ole Ladefoged, Steffen Loft, and Håkan Wallin. 2009. "Lung Inflammation and Genotoxicity Following Pulmonary Exposure to Nanoparticles in ApoE-/- Mice." *Particle and Fibre Toxicology* 6 (January): 2. https://doi.org/10.1186/1743-8977-6-2.

61. Jin, Hee, Michaela Jeong, Gyeongseok Lee, Minjeong Kim, Youngjo Yoo, Hyun Jin Kim, Jaeho Cho, Yun-Sil Lee, and Hyukjin Lee. 2023. “Engineered Lipid Nanoparticles for the Treatment of Pulmonary Fibrosis by Regulating Epithelial-Mesenchymal Transition in the Lungs.” *Advanced Functional Materials* 33 (7): 2209432. https://doi.org/10.1002/adfm.202209432.
62. Karsten, Christian M., Manoj K. Pandey, Julia Figge, Regina Kilchenstein, Philip R. Taylor, Marcela Rosas, Jacqueline U. McDonald, et al. 2012. “Galactosylated IgG1 Links FcγRIIB and Dectin-1 to Block Complement-Mediated Inflammation.” *Nature Medicine* 18 (9): 1401–6. https://doi.org/10.1038/nm.2862.
63. Khandoga, A., T. Stoeger, A. G. Khandoga, P. Bihari, E. Karg, D. Ettehadieh, S. Lakatos, J. Fent, H. Schulz, and F. Krombach. 2010. “Platelet Adhesion and Fibrinogen Deposition in Murine Microvessels upon Inhalation of Nanosized Carbon Particles.” Journal of Thrombosis and Haemostasis: JTH 8 (7): 1632–40. https://doi.org/10.1111/j.1538-7836.2010.03904.x.
64. Kim, Betty Y. S., James T. Rutka, and Warren C. W. Chan. 2010. “Nanomedicine.” *The New England Journal of Medicine* 363 (25): 2434–43. https://doi.org/10.1056/NEJMra0912273.
65. Kim, Christoffer Åberg, Guillermo de Cárcer, Marcos Malumbres, Anna Salvati, and Kenneth A. Dawson. 2013. “Low Dose of Amino-Modified Nanoparticles Induces Cell Cycle Arrest.” *ACS Nano* 7 (9): 7483–94. https://doi.org/10.1021/nn403126e.
66. Kim, and Andrew D. Luster. 2015. “The Role of Tissue Resident Cells in Neutrophil Recruitment.” *Trends in Immunology* 36 (9): 547–55. https://doi.org/10.1016/j.it.2015.07.007.
67. Kolaczkowska, Elzbieta, and Paul Kubes. 2013. “Neutrophil Recruitment and Function in Health and Inflammation.” *Nature Reviews Immunology* 13 (3): 159–75. https://doi.org/10.1038/nri3399.
68. Kornerup, Kristin N., Gary P. Salmon, Simon C. Pitchford, Wai L. Liu, and Clive P. Page. 2010. “Circulating Platelet-Neutrophil Complexes Are Important for Subsequent Neutrophil Activation and Migration.” *Journal of Applied Physiology (Bethesda, Md.: 1985)* 109 (3): 758–67. https://doi.org/10.1152/japplphysiol.01086.2009.
69. Kolde R (2019). _pheatmap: Pretty Heatmaps_. R package version 1.0.12, https://CRAN.R-project.org/package=pheatmap
70. Kuebler, Wolfgang M., and Alwin E. Goetz. 2002. “The Marginated Pool.” *European Surgical Research. Europaische Chirurgische Forschung. Recherches Chirurgicales Europeennes* 34 (1–2): 92–100. https://doi.org/10.1159/000048894.
71. Kreyling, Wolfgang G. 2010. “Nanoparticles in the Lung.”
72. Kreisel, Daniel, Ruben G. Nava, Wenjun Li, Bernd H. Zinselmeyer, Baomei Wang, Jiaming Lai, Robert Pless, Andrew E. Gelman, Alexander S. Krupnick, and Mark J. Miller. 2010. “In Vivo Two-Photon Imaging Reveals Monocyte-Dependent Neutrophil Extravasation during Pulmonary Inflammation.” *Proceedings of the National Academy of Sciences* 107 (42): 18073–78. https://doi.org/10.1073/pnas.1008737107.

73. Last, Jerold A., Rachel Ward, Lisa Temple, Kent E. Pinkerton, and Nicholas J. Kenyon. 2004. “Ovalbumin-Induced Airway Inflammation and Fibrosis in Mice Also Exposed to Ultrafine Particles.” *Inhalation Toxicology* 16 (2): 93–102. https://doi.org/10.1080/08958370490265077.
74. Ley, Klaus, Carlo Laudanna, Myron I. Cybulsky, and Sussan Nourshargh. 2007. “Getting to the Site of Inflammation: The Leukocyte Adhesion Cascade Updated.” *Nature Reviews Immunology* 7 (9): 678–89. https://doi.org/10.1038/nri2156.
75. Li, Wei, Gabriele S. Kaminski Schierle, Bingfu Lei, Yingliang Liu, and Clemens F. Kaminski. 2022. “Fluorescent Nanoparticles for Super-Resolution Imaging.” *Chemical Reviews* 122 (15): 12495–543. https://doi.org/10.1021/acs.chemrev.2c00050.
76. Li, Hao Yang, Manliu Wang, Shouqin Lü, Yan Zhang, and Mian Long. 2018. “Ligand-Specific Binding Forces of LFA-1 and Mac-1 in Neutrophil Adhesion and Crawling.” *Molecular Biology of the Cell* 29 (4): 408–18. https://doi.org/10.1091/mbc.E16-12-0827.
77. Liang, Wanling, Harry W. Pan, Driton Vllasaliu, and Jenny K. W. Lam. 2020. *“Pulmonary Delivery of Biological Drugs.”* Pharmaceutics 12 (11): 1025. https://doi.org/10.3390/pharmaceutics12111025.
78. Liew, Pei Xiong, and Paul Kubes. 2019. “The Neutrophil’s Role During Health and Disease.” *Physiological Reviews* 99 (2): 1223–48. https://doi.org/10.1152/physrev.00012.2018.
79. Lin, Qiaoya, Parinaz Fathi, and Xiaoyuan Chen. 2020. “Nanoparticle Delivery in Vivo: A Fresh Look from Intravital Imaging.” *EBioMedicine* 59 (August): 102958. https://doi.org/10.1016/j.ebiom.2020.102958.
80. Looney, Mark R, Emily E Thornton, Debasish Sen, Wayne J Lamm, Robb W Glenny, and Matthew F Krummel. 2011. “Stabilized Imaging of Immune Surveillance in the Mouse Lung.” *Nature Methods* 8 (1): 91–96. https://doi.org/10.1038/nmeth.1543.
81. Maas, Sanne L., Oliver Soehnlein, and Joana R. Viola. 2018. “Organ-Specific Mechanisms of Transendothelial Neutrophil Migration in the Lung, Liver, Kidney, and Aorta.” *Frontiers in Immunology* 9: 2739. https://doi.org/10.3389/fimmu.2018.02739.
82. Mansour, Heidi M., Yun-Seok Rhee, and Xiao Wu. 2009. “Nanomedicine in Pulmonary Delivery.” *International Journal of Nanomedicine* 4: 299–319. https://doi.org/10.2147/ijn.s4937.
83. Martinez, Fernando J., Harold R. Collard, Annie Pardo, Ganesh Raghu, Luca Richeldi, Moises Selman, Jeffrey J. Swigris, Hiroyuki Taniguchi, and Athol U. Wells. 2017. “Idiopathic Pulmonary Fibrosis.” *Nature Reviews Disease Primers* 3 (1): 1–19. https://doi.org/10.1038/nrdp.2017.74.
84. Matienzo, and Bordoni. 2023. “Anatomy, Blood Flow.” In *StatPearls*. Treasure Island (FL): StatPearls Publishing. http://www.ncbi.nlm.nih.gov/books/NBK554457/.
85. Maurer, M., and E. von Stebut. 2004. “Macrophage Inflammatory Protein-1.” *The International Journal of Biochemistry & Cell Biology* 36 (10): 1882–86. https://doi.org/10.1016/j.biocel.2003.10.019.

86. Mercer, R. R., M. L. Russell, and J. D. Crapo. 1994. “Alveolar Septal Structure in Different Species.” *Journal of Applied Physiology* 77 (3): 1060–66. https://doi.org/10.1152/jappl.1994.77.3.1060.
87. Miles, Tylah, Gerard F Hoyne, Darryl A Knight, Mark W Fear, Steven E Mutsaers, and Cecilia M Prêle. 2020. “The Contribution of Animal Models to Understanding the Role of the Immune System in Human Idiopathic Pulmonary Fibrosis.” *Clinical & Translational Immunology* 9 (7): e1153. https://doi.org/10.1002/cti2.1153.
88. Mitchell, Michael J., Margaret M. Billingsley, Rebecca M. Haley, Marissa E. Wechsler, Nicholas A. Peppas, and Robert Langer. 2021. “Engineering Precision Nanoparticles for Drug Delivery.” *Nature Reviews Drug Discovery* 20 (2): 101–24. https://doi.org/10.1038/s41573-020-0090-8.
89. Mizgerd, J. P., B. B. Meek, G. J. Kutkoski, D. C. Bullard, A. L. Beaudet, and C. M. Doerschuk. 1996. “Selectins and Neutrophil Traffic: Margination and Streptococcus Pneumoniae-Induced Emigration in Murine Lungs.” *The Journal of Experimental Medicine* 184 (2): 639–45. https://doi.org/10.1084/jem.184.2.639.
90. Mizgerd, Hiroshi Kubo, Gregory J. Kutkoski, Sabrina D. Bhagwan, Karin Scharffetter-Kochanek, Arthur L. Beaudet, and Claire M. Doerschuk. 1997. “Neutrophil Emigration in the Skin, Lungs, and Peritoneum: Different Requirements for CD11/CD18 Revealed by CD18-Deficient Mice.” *The Journal of Experimental Medicine* 186 (8): 1357–64. https://www.ncbi.nlm.nih.gov/pmc/articles/PMC2199087/.
91. Morimoto, Yasuo, Masanori Horie, Norihiro Kobayashi, Naohide Shinohara, and Manabu Shimada. 2013. “Inhalation Toxicity Assessment of Carbon-Based Nanoparticles.” *Accounts of Chemical Research* 46 (3): 770–81. https://doi.org/10.1021/ar200311b.
92. Moyano, Daniel F., Yuanchang Liu, Furkan Ayaz, Singyuk Hou, Premsak Puangploy, Bradley Duncan, Barbara A. Osborne, and Vincent M. Rotello. 2016. “Immunomodulatory Effects of Coated Gold Nanoparticles in LPS-Stimulated in Vitro and in Vivo Murine Model Systems.” *Chem* 1 (2): 320–27. https://doi.org/10.1016/j.chempr.2016.07.007.
93. Murgia, Xabi, Cristiane de Souza Carvalho, and Claus-Michael Lehr. 2014. “Overcoming the Pulmonary Barrier: New Insights to Improve the Efficiency of Inhaled Therapeutics.” *European Journal of Nanomedicine* 6 (3): 157–69. https://doi.org/10.1515/ejnm-2014-0019.
94. Murugadoss, Sivakumar, Dominique Lison, Lode Godderis, Sybille Van Den Brule, Jan Mast, Frederic Brassinne, Noham Sebaihi, and Peter H. Hoet. 2017. “Toxicology of Silica Nanoparticles: An Update.” *Archives of Toxicology* 91 (9): 2967–3010. https://doi.org/10.1007/s00204-017-1993-y.
95. Nicolaou, Laura, Magdalena Fandiño-Del-Rio, Kirsten Koehler, and William Checkley. 2021. “Size Distribution and Lung-Deposited Doses of Particulate Matter from Household Exposure to Biomass Smoke.” *Indoor Air* 31 (1): 51–62. https://doi.org/10.1111/ina.12710.

96. Neupane, Arpan Sharma, and Paul Kubes. 2022. “Imaging Reveals Novel Innate Immune Responses in Lung, Liver, and Beyond*.” *Immunological Reviews* 306 (1): 244–57. https://doi.org/10.1111/imr.13040.
97. Nguyen, Dung Hoang, Newton Cho, Kajana Satkunendrarajah, James W. Austin, Jian Wang, and Michael G. Fehlings. 2012. “Immunoglobulin G (IgG) Attenuates Neuroinflammation and Improves Neurobehavioral Recovery after Cervical Spinal Cord Injury.” *Journal of Neuroinflammation* 9 (1): 224. https://doi.org/10.1186/1742-2094-9-224.
98. Ng, Cheng-Teng, Jia’En Jasmine Li, Suresh Kumar Balasubramanian, Fang You, Lin-Yue Lanry Yung, and Boon-Huat Bay. 2016. “Inflammatory Changes in Lung Tissues Associated with Altered Inflammation-Related MicroRNA Expression after Intravenous Administration of Gold Nanoparticles in Vivo.” *ACS Biomaterials Science & Engineering* 2 (11): 1959–67. https://doi.org/10.1021/acsbiomaterials.6b00358.
99. Nurkiewicz, Timothy R., Dale W. Porter, Mark Barger, Lyndell Millecchia, K. Murali K. Rao, Paul J. Marvar, Ann F. Hubbs, Vincent Castranova, and Matthew A. Boegehold. 2006. “Systemic Microvascular Dysfunction and Inflammation after Pulmonary Particulate Matter Exposure.” *Environmental Health Perspectives* 114 (3): 412–19. https://doi.org/10.1289/ehp.8413.
100. Oberdörster, G. 2001. “Pulmonary Effects of Inhaled Ultrafine Particles.” *International Archives of Occupational and Environmental Health* 74 (1): 1–8. https://doi.org/10.1007/s004200000185.
101. Pardo, Annie, Roberto Barrios, Miguel Gaxiola, Lourdes Segura-Valdez, Guillermo Carrillo, Andrea Estrada, Mayra Mejía, and Moisés Selman. 2000. “Increase of Lung Neutrophils in Hypersensitivity Pneumonitis Is Associated with Lung Fibrosis.” *American Journal of Respiratory and Critical Care Medicine* 161 (5): 1698–1704. https://doi.org/10.1164/ajrccm.161.5.9907065.
102. Parhiz, Hamideh, Jacob S. Brenner, Priyal N. Patel, Tyler E. Papp, Hamna Shahnawaz, Qin Li, Ruiqi Shi, et al. 2022. “Added to Pre-Existing Inflammation, MRNA-Lipid Nanoparticles Induce Inflammation Exacerbation (IE).” *Journal of Controlled Release: Official Journal of the Controlled Release Society* 344 (April): 50–61. https://doi.org/10.1016/j.jconrel.2021.12.027.
103. Park, Inwon, Kibaek Choe, Howon Seo, Yoonha Hwang, Eunjoo Song, Jinhyo Ahn, You Hwan Jo, and Pilhan Kim. 2018. “Intravital Imaging of a Pulmonary Endothelial Surface Layer in a Murine Sepsis Model.” *Biomedical Optics Express* 9 (5): 2383. https://doi.org/10.1364/BOE.9.002383.
104. Park, Inwon, Mingyo Kim, Kibaek Choe, Eunjoo Song, Howon Seo, Yoonha Hwang, Jinhyo Ahn, et al. 2019. “Neutrophils Disturb Pulmonary Microcirculation in Sepsis-Induced Acute Lung Injury.” *European Respiratory Journal* 53 (3): 1800786. https://doi.org/10.1183/13993003.00786-2018.
105. Peterson, Jennifer M., Kevin D. Feeback, Joel H. Baas, and Francis X. Pizza. 2006. “Tumor Necrosis Factor-α Promotes the Accumulation of Neutrophils and Macrophages in Skeletal

Muscle." *Journal of Applied Physiology* 101 (5): 1394–99. https://doi.org/10.1152/japplphysiol.01453.2005.

106. Phillipson, Mia, Bryan Heit, Pina Colarusso, Lixin Liu, Christie M. Ballantyne, and Paul Kubes. 2006. "Intraluminal Crawling of Neutrophils to Emigration Sites: A Molecularly Distinct Process from Adhesion in the Recruitment Cascade." *The Journal of Experimental Medicine* 203 (12): 2569–75. https://doi.org/10.1084/jem.20060925.
107. Phillipson, Mia, and Paul Kubes. 2011. "The Neutrophil in Vascular Inflammation." *Nature Medicine* 17 (11): 1381–90. https://doi.org/10.1038/nm.2514.
108. Praetner, Marc, Markus Rehberg, Peter Bihari, Max Lerchenberger, Bernd Uhl, Martin Holzer, Martin E. Eichhorn, Robert Fürst, Tamara Perisic, and Christoph A. Reichel. 2010. "The Contribution of the Capillary Endothelium to Blood Clearance and Tissue Deposition of Anionic Quantum Dots in Vivo." *Biomaterials* 31 (26): 6692–6700. https://doi.org/10.1016/j.biomaterials.2010.05.051.
109. Qiao, Qi, Xiong Liu, Ting Yang, Kexin Cui, Li Kong, Conglian Yang, and Zhiping Zhang. 2021. "Nanomedicine for Acute Respiratory Distress Syndrome: The Latest Application, Targeting Strategy, and Rational Design." *Acta Pharmaceutica Sinica B* 11 (10): 3060–91. https://doi.org/10.1016/j.apsb.2021.04.023.
110. R Core Team (2023). R: A language and environment for statistical computing. R Foundation for Statistical Computing, Vienna, Austria. https://www.R-project.org/.
111. Ramos, Cleber D. L., Claudio Canetti, Janeusa T. Souto, João S. Silva, Cory M. Hogaboam, Sergio H. Ferreira, and Fernando Q. Cunha. 2005. "MIP-1alpha [CCL3] Acting on the CCR1 Receptor Mediates Neutrophil Migration in Immune Inflammation via Sequential Release of TNF-Alpha and LTB4." *Journal of Leukocyte Biology* 78 (1): 167–77. https://doi.org/10.1189/jlb.0404237.
112. Ramos-Gomes, Fernanda, Nathalia Ferreira, Alexander Kraupner, Frauke Alves, and M. Andrea Markus. 2020. "Ex Vivo Live Cell Imaging of Nanoparticle-Cell Interactions in the Mouse Lung." *Frontiers in Bioengineering and Biotechnology* 8 (October): 588922. https://doi.org/10.3389/fbioe.2020.588922.
113. Rehberg, M., M. Praetner, C. F. Leite, C. A. Reichel, P. Bihari, K. Mildner, S. Duhr, D. Zeuschner, and F. Krombach. 2010. "Quantum Dots Modulate Leukocyte Adhesion and Transmigration Depending on Their Surface Modification." *Nano Letters* 10 (9): 3656–64. https://doi.org/10.1021/nl102100m.
114. Rehberg, Markus, Camila F. Leite, Karina Mildner, Jan Horstkotte, Dagmar Zeuschner, and Fritz Krombach. 2012. "Surface Chemistry of Quantum Dots Determines Their Behavior in Postischemic Tissue." *ACS Nano* 6 (2): 1370–79. https://doi.org/10.1021/nn204187c.
115. Rehberg, Markus, Katharina Nekolla, Sabine Sellner, Marc Praetner, Karina Mildner, Dagmar Zeuschner, and Fritz Krombach. 2016. "Intercellular Transport of Nanomaterials Is Mediated by Membrane Nanotubes In Vivo." *Small* 12 (14): 1882–90. https://doi.org/10.1002/smll.201503606.

116. Reichel, Christoph Andreas, Markus Rehberg, Max Lerchenberger, Nina Berberich, Peter Bihari, Alexander Georg Khandoga, Stefan Zahler, and Fritz Krombach. 2009. “Ccl2 and Ccl3 Mediate Neutrophil Recruitment via Induction of Protein Synthesis and Generation of Lipid Mediators.” *Arteriosclerosis, Thrombosis, and Vascular Biology* 29 (11): 1787–93. https://doi.org/10.1161/ATVBAHA.109.193268.

117. Resnik, David B., and Sally S. Tinkle. 2007. “Ethical Issues in Clinical Trials Involving Nanomedicine.” *Contemporary Clinical Trials* 28 (4): 433–41. https://doi.org/10.1016/j.cct.2006.11.001.

118. Richter, Jillian R., Jeffrey M. Sutton, Ritha M. Belizaire, Lou Ann Friend, Rebecca M. Schuster, Taylor A. Johannigman, Steven G. Miller, Alex B. Lentsch, and Timothy A. Pritts. 2014. “Macrophage-Derived Chemokine (MDC/CCL22) Is a Novel Mediator of Lung Inflammation Following Hemorrhage and Resuscitation.” *Shock (Augusta, Ga.)* 42 (6): 525–31. https://doi.org/10.1097/SHK.0000000000000253.

119. Rittirsch, Daniel, Michael A. Flierl, Danielle E. Day, Brian A. Nadeau, Stephanie R. McGuire, Laszlo M. Hoesel, Kyros Ipaktchi, et al. 2008. “Acute Lung Injury Induced by Lipopolysaccharide Is Independent of Complement Activation.” *Journal of Immunology (Baltimore, Md. : 1950)* 180 (11): 7664–72. https://www.ncbi.nlm.nih.gov/pmc/articles/PMC2753408/.

120. Riteau, Nicolas, Pamela Gasse, Louis Fauconnier, Aurélie Gombault, Marion Couegnat, Lizette Fick, Jean Kanellopoulos, et al. 2010. “Extracellular ATP Is a Danger Signal Activating P2X7 Receptor in Lung Inflammation and Fibrosis.” *American Journal of Respiratory and Critical Care Medicine* 182 (6): 774–83. https://doi.org/10.1164/rccm.201003-0359OC.

121. Roberts, Jenny R., James M. Antonini, Dale W. Porter, Rebecca S. Chapman, James F. Scabilloni, Shih-Houng Young, Diane Schwegler-Berry, Vincent Castranova, and Robert R. Mercer. 2013. “Lung Toxicity and Biodistribution of Cd/Se-ZnS Quantum Dots with Different Surface Functional Groups after Pulmonary Exposure in Rats.” *Particle and Fibre Toxicology* 10 (1): 5. https://doi.org/10.1186/1743-8977-10-5.

122. Rossaint, Jan, and Alexander Zarbock. 2013. “Tissue-Specific Neutrophil Recruitment into the Lung, Liver, and Kidney.” *Journal of Innate Immunity* 5 (4): 348–57. https://doi.org/10.1159/000345943.

123. Rosales, Carlos. 2018. “Neutrophil: A Cell with Many Roles in Inflammation or Several Cell Types?” *Frontiers in Physiology* 9 (February): 113. https://doi.org/10.3389/fphys.2018.00113.

124. Rossi, Lea Pylkkänen, Antti J. Koivisto, Minnamari Vippola, Keld A. Jensen, Mirella Miettinen, Kristiina Sirola, et al. 2010. “Airway Exposure to Silica-Coated TiO2 Nanoparticles Induces Pulmonary Neutrophilia in Mice.” *Toxicological Sciences: An Official Journal of the Society of Toxicology* 113 (2): 422–33. https://doi.org/10.1093/toxsci/kfp254.

125. Rotondo, John Charles, Chiara Mazziotta, Carmen Lanzillotti, Chiara Stefani, Giada Badiale, Giulia Campione, Fernanda Martini, and Mauro Tognon. 2022. “The Role of Purinergic P2X7 Receptor in Inflammation and Cancer: Novel Molecular Insights and Clinical Applications.” *Cancers* 14 (5): 1116. https://doi.org/10.3390/cancers14051116.

126. Ryman-Rasmussen, Mark F. Cesta, Arnold R. Brody, Jeanette K. Shipley-Phillips, Jeffrey I. Everitt, Earl W. Tewksbury, Owen R. Moss, et al. 2009. “Inhaled Carbon Nanotubes Reach the Subpleural Tissue in Mice.” *Nature Nanotechnology* 4 (11): 747–51. https://doi.org/10.1038/nnano.2009.305.

127. Sagawa, Tomoya, Akiko Honda, Raga Ishikawa, Natsuko Miyasaka, Megumi Nagao, Sakiko Akaji, Takashi Kida, et al. 2021. “Role of Necroptosis of Alveolar Macrophages in Acute Lung Inflammation of Mice Exposed to Titanium Dioxide Nanoparticles.” *Nanotoxicology* 15 (10): 1312–30. https://doi.org/10.1080/17435390.2021.2022231.

128. Samuel, Stephen P, Maria J Santos-Martinez, Carlos Medina, Namrata Jain, Marek W Radomski, Adriele Prina-Mello, and Yuri Volkov. 2015. “CdTe Quantum Dots Induce Activation of Human Platelets: Implications for Nanoparticle Hemocompatibility.” *International Journal of Nanomedicine* 10 (April): 2723–34. https://doi.org/10.2147/IJN.S78281.

129. Sattler, Christine, Franco Moritz, Shanze Chen, Beatrix Steer, David Kutschke, Martin Irmler, Johannes Beckers, et al. 2017. “Nanoparticle Exposure Reactivates Latent Herpesvirus and Restores a Signature of Acute Infection.” Particle and Fibre Toxicology 14 (1): 2. https://doi.org/10.1186/s12989-016-0181-1.

130. Secklehner, Judith, Cristina Lo Celso, and Leo M Carlin. 2017. “Intravital Microscopy in Historic and Contemporary Immunology.” *Immunology & Cell Biology* 95 (6): 506–13. https://doi.org/10.1038/icb.2017.25.

131. Segal, Anthony W. 2005. “How Neutrophils Kill Microbes.” *Annual Review of Immunology* 23: 197–223. https://doi.org/10.1146/annurev.immunol.23.021704.115653.

132. Schindelin, J., Arganda-Carreras, I., Frise, E., Kaynig, V., Longair, M., Pietzsch, T., … Cardona, A. (2012). Fiji: an open-source platform for biological-image analysis. Nature Methods, 9(7), 676–682. doi:10.1038/nmeth.2019

133. Singh, Abhalaxmi, Sreeparna Chakraborty, Sing Wan Wong, Nicole A. Hefner, Andrew Stuart, Abdul S. Qadir, Amitabha Mukhopadhyay, et al. 2022. “Nanoparticle Targeting of de Novo Profibrotic Macrophages Mitigates Lung Fibrosis.” *Proceedings of the National Academy of Sciences of the United States of America* 119 (15): e2121098119. https://doi.org/10.1073/pnas.2121098119.

134. Shah, Dilip, Freddy Romero, William Stafstrom, Michelle Duong, and Ross Summer. 2014. “Extracellular ATP Mediates the Late Phase of Neutrophil Recruitment to the Lung in Murine Models of Acute Lung Injury.” *American Journal of Physiology. Lung Cellular and Molecular Physiology* 306 (2): L152-161. https://doi.org/10.1152/ajplung.00229.2013.

135. Smola, Malgorzata, Thierry Vandamme, and Adam Sokolowski. 2008. “Nanocarriers as Pulmonary Drug Delivery Systems to Treat and to Diagnose Respiratory and Non-Respiratory Diseases.” *International Journal of Nanomedicine* 3 (1): 1–19. https://www.ncbi.nlm.nih.gov/pmc/articles/PMC2526354/.

136. Stenvinkel, Peter, Markus Ketteler, Richard J. Johnson, Bengt Lindholm, Roberto Pecoits-Filho, Miguel Riella, Olof Heimbürger, Tommy Cederholm, and Matthias Girndt. 2005. “IL-10,

IL-6, and TNF-α: Central Factors in the Altered Cytokine Network of Uremia—The Good, the Bad, and the Ugly." *Kidney International* 67 (4): 1216–33. https://doi.org/10.1111/j.1523-1755.2005.00200.x.

137. Sumagin, Ronen, Hen Prizant, Elena Lomakina, Richard E. Waugh, and Ingrid H. Sarelius. 2010. "LFA-1 and Mac-1 Define Characteristically Different Intralumenal Crawling and Emigration Patterns for Monocytes and Neutrophils In Situ." *The Journal of Immunology* 185 (11): 7057–66. https://doi.org/10.4049/jimmunol.1001638.
138. Tashiro, Jun, Gustavo A. Rubio, Andrew H. Limper, Kurt Williams, Sharon J. Elliot, Ioanna Ninou, Vassilis Aidinis, Argyrios Tzouvelekis, and Marilyn K. Glassberg. 2017. "Exploring Animal Models That Resemble Idiopathic Pulmonary Fibrosis." *Frontiers in Medicine* 4 (July): 118. https://doi.org/10.3389/fmed.2017.00118.
139. Tabuchi, Arata, Michael Mertens, Hermann Kuppe, Axel R. Pries, and Wolfgang M. Kuebler. 2008. "Intravital Microscopy of the Murine Pulmonary Microcirculation." *Journal of Applied Physiology* 104 (2): 338–46. https://doi.org/10.1152/japplphysiol.00348.2007.
140. Tang, Daolin, Rui Kang, Carolyn B. Coyne, Herbert J. Zeh, and Michael T. Lotze. 2012. "PAMPs and DAMPs: Signal 0s That Spur Autophagy and Immunity." *Immunological Reviews* 249 (1): 158–75. https://doi.org/10.1111/j.1600-065X.2012.01146.x.
141. Terry, R. J. 1939. "A THORACIC WINDOW FOR OBSERVATION OF THE LUNG IN A LIVING ANIMAL." Science (New York, N.Y.) 90 (2324): 43–44. https://doi.org/10.1126/science.90.2324.43.
142. Thompson, Elizabeth A., Brian C. Sayers, Ellen E. Glista-Baker, Kelly A. Shipkowski, Alexia J. Taylor, and James C. Bonner. 2014. "Innate Immune Responses to Nanoparticle Exposure in the Lung." *Journal of Environmental Immunology and Toxicology* 1 (3): 150–56. https://doi.org/10.7178/jeit.23.
143. Tran, Jimmy N.S.N., Aleta Pupovac, Rosanne M. Taylor, James S. Wiley, Scott N. Byrne, and Ronald Sluyter. 2010. "Murine Epidermal Langerhans Cells and Keratinocytes Express Functional P2X7 Receptors." *Experimental Dermatology* 19 (8): e151–57. https://doi.org/10.1111/j.1600-0625.2009.01029.x.
144. Thompson, Elizabeth A., Brian C. Sayers, Ellen E. Glista-Baker, Kelly A. Shipkowski, Alexia J. Taylor, and James C. Bonner. 2014. "Innate Immune Responses to Nanoparticle Exposure in the Lung." *Journal of Environmental Immunology and Toxicology* 1 (3): 150–56. https://doi.org/10.7178/jeit.23.
145. Townsley, Mary I. 2012. "Structure and Composition of Pulmonary Arteries, Capillaries and Veins." *Comprehensive Physiology* 2 (January): 675–709. https://doi.org/10.1002/cphy.c100081.
146. Ueki, Hiroshi, I-Hsuan Wang, Satoshi Fukuyama, Hiroaki Katsura, Tiago Jose da Silva Lopes, Gabriele Neumann, and Yoshihiro Kawaoka. 2018. "In Vivo Imaging of the Pathophysiological Changes and Neutrophil Dynamics in Influenza Virus-Infected Mouse Lungs." *Proceedings of*

the National Academy of Sciences 115 (28): E6622–29. https://doi.org/10.1073/pnas.1806265115.

147. Uhl, Bernd, Stephanie Hirn, Karina Mildner, Raffaele Coletti, Steffen Massberg, Christoph A. Reichel, Markus Rehberg, Dagmar Zeuschner, and Fritz Krombach. 2018. "The Surface Chemistry Determines the Spatio-Temporal Interaction Dynamics of Quantum Dots in Atherosclerotic Lesions." *Nanomedicine (London, England)* 13 (6): 623–38. https://doi.org/10.2217/nnm-2017-0350.
148. Veronese, Francesco M., and Anna Mero. 2008. "The Impact of PEGylation on Biological Therapies." *BioDrugs: Clinical Immunotherapeutics, Biopharmaceuticals and Gene Therapy* 22 (5): 315–29. https://doi.org/10.2165/00063030-200822050-00004.
149. Waisman, Dan, Amir Abramovich, Vera Brod, Ofir Lavon, Steven Nurkin, Faina Popovski, Avi Rotschild, and Haim Bitterman. 2006. "Subpleural Microvascular Flow Velocities and Shear Rates in Normal and Septic Mechanically Ventilated Rats." *Shock (Augusta, Ga.)* 26 (1): 87–94. https://doi.org/10.1097/01.shk.0000215317.22113.b2.
150. Ward, P. A. 2003. "Acute Lung Injury: How the Lung Inflammatory Response Works." *European Respiratory Journal* 22 (44 suppl): 22s–23s. https://doi.org/10.1183/09031936.03.00000703a.
151. Warheit, D. B., B. R. Laurence, K. L. Reed, D. H. Roach, G. a. M. Reynolds, and T. R. Webb. 2004. "Comparative Pulmonary Toxicity Assessment of Single-Wall Carbon Nanotubes in Rats." *Toxicological Sciences: An Official Journal of the Society of Toxicology* 77 (1): 117–25. https://doi.org/10.1093/toxsci/kfg228.
152. Warheit, David B., Thomas R. Webb, Kenneth L. Reed, Scott Frerichs, and Christie M. Sayes. 2007. "Pulmonary Toxicity Study in Rats with Three Forms of Ultrafine-TiO2 Particles: Differential Responses Related to Surface Properties." *Toxicology* 230 (1): 90–104. https://doi.org/10.1016/j.tox.2006.11.002.
153. Wegner, K. David, and Niko Hildebrandt. 2015. "Quantum Dots: Bright and Versatile in Vitro and in Vivo Fluorescence Imaging Biosensors." *Chemical Society Reviews* 44 (14): 4792–4834. https://doi.org/10.1039/C4CS00532E.
154. Wiggs, D. English, W. M. Quinlan, N. A. Doyle, J. C. Hogg, and C. M. Doerschuk. 1994. "Contributions of Capillary Pathway Size and Neutrophil Deformability to Neutrophil Transit through Rabbit Lungs." *Journal of Applied Physiology (Bethesda, Md.: 1985)* 77 (1): 463–70. https://doi.org/10.1152/jappl.1994.77.1.463.
155. Wissinger, E. L., J. Saldana, A. Didierlaurent, and T. Hussell. 2008. "Manipulation of Acute Inflammatory Lung Disease." *Mucosal Immunology* 1 (4): 265–78. https://doi.org/10.1038/mi.2008.16.
156. Xu, Cynthia, Frank W. Sellke, and M. Ruhul Abid. 2022. "Assessments of Microvascular Function in Organ Systems." *American Journal of Physiology-Heart and Circulatory Physiology* 322 (6): H891–905. https://doi.org/10.1152/ajpheart.00589.2021.

157. Xu, Jingsong, Xiao-Pei Gao, Ramaswamy Ramchandran, You-Yang Zhao, Stephen M Vogel, and Asrar B Malik. 2008. “Nonmuscle Myosin Light-Chain Kinase Mediates Neutrophil Transmigration in Sepsis-Induced Lung Inflammation by Activating B2 Integrins.” *Nature Immunology* 9 (8): 880–86. https://doi.org/10.1038/ni.1628.

158. Yacobi, Nazanin R., Farnoosh Fazllolahi, Yong Ho Kim, Arnold Sipos, Zea Borok, Kwang-Jin Kim, and Edward D. Crandall. 2011. “Nanomaterial Interactions with and Trafficking across the Lung Alveolar Epithelial Barrier: Implications for Health Effects of Air-Pollution Particles.” *Air Quality, Atmosphere, & Health* 4 (1): 65–78. https://doi.org/10.1007/s11869-010-0098-z.

159. Yang, Guangbao, Soo Zeng Fiona Phua, Anivind Kaur Bindra, and Yanli Zhao. 2019. “Degradability and Clearance of Inorganic Nanoparticles for Biomedical Applications.” *Advanced Materials* 31 (10): 1805730. https://doi.org/10.1002/adma.201805730.

160. Yeh, Yu-Wen, Arka Sen Chaudhuri, Ling Zhou, Yu Fang, Preben Boysen, and Zou Xiang. 2021. “Mast Cells Are Identified in the Lung Parenchyma of Wild Mice, Which Can Be Recapitulated in Naturalized Laboratory Mice.” *Frontiers in Immunology* 12 (September): 736692. https://doi.org/10.3389/fimmu.2021.736692.

161. Yipp, Bryan G., Jung Hwan Kim, Ronald Lima, Lori D. Zbytnuik, Björn Petri, Nick Swanlund, May Ho, et al. 2017. “The Lung Is a Host Defense Niche for Immediate Neutrophil-Mediated Vascular Protection.” *Science Immunology* 2 (10): eaam8929. https://doi.org/10.1126/sciimmunol.aam8929.

162. Zarbock, Alexander, Klaus Ley, Rodger P. McEver, and Andrés Hidalgo. 2011. “Leukocyte Ligands for Endothelial Selectins: Specialized Glycoconjugates That Mediate Rolling and Signaling under Flow.” *Blood* 118 (26): 6743–51. https://doi.org/10.1182/blood-2011-07-343566.

163. Zarnegar, Behdad, Annika Westin, Syrmoula Evangelidou, and Jenny Hallgren. 2018. “Innate Immunity Induces the Accumulation of Lung Mast Cells During Influenza Infection.” *Frontiers in Immunology* 9. https://www.frontiersin.org/articles/10.3389/fimmu.2018.02288.

164. Zeuschner. 2015. “Quantum Dots in Transmission Electron Microscopy.” Imaging and Microscopy. 2015. https://analyticalscience.wiley.com/do/10.1002/imaging.5241.

165. Zhang, Yan, Bernard F. Ramos, and Barbara A. Jakschik. 1992. “Neutrophil Recruitment by Tumor Necrosis Factor from Mast Cells in Immune Complex Peritonitis.” *Science* 258 (5090): 1957–59. https://doi.org/10.1126/science.1470922.

166. Zhou, Yan, Bo Zhang, Chen Li, XiaoTing Huang, HaiPeng Cheng, XingWen Bao, FeiYan Zhao, et al. 2019. “Megakaryocytes Participate in the Occurrence of Bleomycin-Induced Pulmonary Fibrosis.” *Cell Death & Disease* 10 (9): 1–14. https://doi.org/10.1038/s41419-019-1903-8.

167. Zhou, Weitao Jin, and Jingjun Ma. 2023. “Lung Inflammation Perturbation by Engineered Nanoparticles.” *Frontiers in Bioengineering and Biotechnology* 11 (May): 1199230. https://doi.org/10.3389/fbioe.2023.1199230.

168. Zhu, Geyunjian Harry, Alex B. C. Gray, and Hirak K. Patra. 2022. “Nanomedicine: Controlling Nanoparticle Clearance for Translational Success.” *Trends in Pharmacological Sciences* 43 (9): 709–11. https://doi.org/10.1016/j.tips.2022.05.001.

7. Apendix

7.1 Abbrevatioins

%	percent
°C	grad Celsius
µ	micro
µg	microgram
µl	microliter
µm	micrometer
3D	three-dimensional
aQDs	amine (PEG) Quantum Dots
ALI	acute lung injury
ATP	adenosine triphosphate
ARDS	acute respiratory distress syndrome
BAL	bronchoalveolar lavage
BALF	bronchoalveolar lavage fluid
BSA	bovine serum albumin
BW	body weight
ca.	circa
CdSe	cadmium selenide
CO_2	carbon dioxide
COPD	chronic obstructive pulmonary disease
cQDs	carboxyl Quantum Dots
Ctrl	control
DAMPs	damage-associated molecular patterns
DBE	dibenzyl ether
DCM	dichloromethane
DNA	deoxyribonucleic acid
DPBS	dulbecco’s phosphate buffered saline
eATP	extracellular ATP
EDTA	ethylenediaminetetraacetic acid
et al.	et alii
Fig.	figure
FOV	field of view
g	gram
h	hour
H&E	haematoxylin and eosin

H_2O	water
HCL	hydrochloric acid
HUVEC	human umbilical vein endothelial cell
ICAM-1	intercellular adhesion molecule 1
i.e.	id est
Ig	immunoglobulin
IL	interleukin
i.p.	intraperitoneal
IPF	idiopathic pulmonary fibrosis
i.v.	intravenous
IVC	individually ventilated cages
IVM	intravital microscopy
IVIS	in vivo imaging system
kg	kilogram
L	liter
LDHa	lactate dehydrogenase
LFA-1	lymphocyte function-associated antigen 1
L-IVM	lung intravital microscope
LPS	lipopolysaccharide
LSFM	light sheet fluorescence microscope
m	milli
Mac-1	macrophage 1
mAbs	monoclonal antibody
MCP	monocyte chemoattractant protein
MDC	macrophage-derived chemokine
mg	milligram
min	minutes
MIP	macrophage inflammatory protein
ml	milliliter
MMF	medetomidinhydrochlorid, midazolam, fentanyl
MPS	mononuclear phagocyte system
NETs	neutrophil extracellular traps
NFkB	nuclear factor 'kappa-light-chain-enhancer' of activated B- cells
ng	nanogram
nm	nanometer
NPs	nanoparticles
O_2	oxygen
O.C.T compound	optimal cutting temperature compound

P2X7R	P2X7 receptor
PEEP	positive end-expiratory pressure
PEG	polyethylene glycol
PFA	paraformaldehyde
pH	potential of hydrogen
PRR	pattern recognition receptor
PSGL1	P-selectin glycoprotein ligand 1
QDs	Quantum Dots
RNA	ribonucleic acid
ROS	reactive oxygen species
rpm	revolutions per minute
RT	room temperature
SEM	standard error of the mean
TEM	transmission electron microscopy
THF	tetrahydrofuran
TLR4	toll-like receptor 4
TNF-α	tumor necrosis factor alpha
UK	United Kingdom
USA	United States of America
WBC	white blood cells
ZnS	zinc sulfide

Acknowledgements

First and foremost, I would like to express my sincere gratitude to Prof. Dr. Markus Rehberg (LHI/CPC) for his invaluable guidance and unwavering support as my supervisor. His mentorship and teachings on the L-IVM procedure have been instrumental in my research journey, and I am deeply grateful for his trust, patience, and insightful advice that contributed to the realization of this thesis.

I am also thankful to Dr. Tobias Stöger for graciously accepting me into his research group at the Helmholtz Zentrum München. His valuable comments and advice have played a crucial role in shaping the direction and outcomes of my thesis.

Furthermore, I extend my heartfelt appreciation to my esteemed committee member, Prof. Dr. med. Markus Sperandio (Walter-Brendel-Centre, LMU), for his constant support, engaging discussions, and constructive feedback that enriched the quality of my research.

I want to acknowledge China Scholarship Council, which has provided me with the opportunity to pursue doctoral studies and expand my horizons in a different academic environment. The support from my motherland has empowered me to further academic pursuits and achieve personal growth.

My gratitude extends to all the members of LHI/CPC with whom I have had the pleasure of working, Dr. Carola Voss, Dr. Qiaoxia Zhou, Eva Günther, Elisabeth Folwarcany, Hongyu Ren, Yasmin Shaalan, Phoebe Cabanis, Camille Barro, Haiyun Zhang, particularly Dr. Lianyong Han, Dr. Verena Häfner, David Kutschke and Dr. Lin Yang for their contributions and invaluable guidance throughout this journey. I would like to thank Qiongliang Liu for his nice cooperation and helpfulness during the execution of my experiments.

I would like to extend my additional gratitude to Dr. Roland Immler (Walter-Brendel-Centre, LMU), Barbara Mosetter (IMA-TCI, GmbH), and Dr. med. vet. Birgit Rathkolb (Molecular Animal Breeding and Biotechnology, LMU/GmbH) for their invaluable assistance and close collaboration in my research project. Their expertise and insightful discussions have been instrumental in advancing my work and contributing to the success of this thesis. I am truly grateful for their support and guidance throughout this journey.

Special thanks go to the SMAP team for their support in supplying and providing

the necessary resources, including mice, for my research.

Of course, I cannot forget to express my deepest gratitude to my parents, Guoliang Li and Xuejun Chen, and my little brother, Chenyang Li. Their unwavering love and unconditional support have been the driving force behind my pursuit of studying in a foreign country. Their encouragement and belief in me have given me the courage to face challenges on the road to development. With their support, I can be myself without fear.

I am truly blessed to have such incredible and intimate friends like Jin Guo, Shiqi Luo, Xin Zhang, Shaoying Liu, and others. I am incredibly fortunate to have them to accompany me through my darkest and most painful moments. During times of deep despair, they have shown me that I am worthy of love and trust, and they have taught me how to embrace life with optimism and resilience. Despite our different geographical locations and diverse experiences, the joy and happiness they bring into my life are irreplaceable. Their friendship is a treasure that I cherish dearly, and I am eternally grateful for their presence in my life.

In conclusion, this thesis would not have been possible without the invaluable contributions and unwavering support from all those mentioned above. I am grateful for the opportunities, knowledge, and life lessons that have shaped my academic and personal growth.

Affidavit

Affidavit

Li, Chenxi
_____
Surname, first name

Ingolstädter Landstraße 1
_____
Street

85764, Neuherberg, Germany
_____
Zip code, town, country

I hereby declare, that the submitted thesis entitled:

Behavior and effect of nanoparticles in the pulmonary microcirculation
…….

is my own work. I have only used the sources indicated and have not made unauthorised use of services of a third party. Where the work of others has been quoted or reproduced, the source is always given.

I further declare that the dissertation presented here has not been submitted in the same or similar form to any other institution for the purpose of obtaining an academic degree.

_01.02.2024. Munich_____ ___Chenxi Li_____
place, date Signature doctoral candidate

Confirmation of congruency

LMU LUDWIG-MAXIMILIANS-UNIVERSITÄT MÜNCHEN

Promotionsbüro Medizinische Fakultät

MMRS

Confirmation of congruency between printed and electronic version of the doctoral thesis

Li, Chenxi

Surname, first name

Ingolstädter Landstraße 1

Street

85764, Neuherberg, Germany

Zip code, town, country

I hereby declare, that the submitted thesis entitled:

Behavior and effect of nanoparticles in the pulmonary microcirculation

……

is congruent with the printed version both in content and format.

__01.02.2024_Munich___
place, date

__ Chenxi Li_____
Signature doctoral candidate

List of publications

1. **Chenxi Li***, et al. Markus Rehberg[#]. Behavior and effect of nanoparticles in the pulmonary microcirculation. 2023 (in preparation)
2. Qiongliang Liu*, **Chenxi Li**, et al. Markus Rehberg[#]. Real time in vivo investigation of the innate immune response during ventilator-assisted nanoparticle inhalation, Nature Nanotech. 2023 (in preparation)
3. Shanshan Song*, Fransien van Dijk*, Qiongliang. Liu, Marina de Jager, Sophie Bos, **Chenxi Li**, Tobias Stöger, Markus Rehberg**,** David Kutschke**,** et al. Barbro N Melgert[#]. Nylon microplastic fibers inhibit outgrowth of airway epithelial cells through upregulating Hoxa5, Am. J. Respir. Crit. 2022 (under review)
4. **Chenxi Li*,** Wenke Chen, Jin Guo, Wei Guan[#]. Relationship of Inhaled Long-acting Bronchodilators with Cardiovascular Outcomes Among Patients with Stable COPD: A Meta-Analysis and Systematic Review OF 43 Randomized Trials, Int J Chron Obstruct Pulmon Dis, 2019,14:799-808.